12-2013

Bond Performance of High-Capacity Strands in High Strength Concrete

Xin Jiang
University of Tennessee - Knoxville, xjiang11@utk.edu

To the Graduate Council:

I am submitting herewith a dissertation written by Xin Jiang entitled "Bond Performance of High-Capacity Strands in High Strength Concrete." I have examined the final electronic copy of this dissertation for form and content and recommend that it be accepted in partial fulfillment of the requirements for the degree of Doctor of Philosophy, with a major in Civil Engineering.

Z. John Ma, Major Professor

We have read this dissertation and recommend its acceptance:

Edwin G. Burdette, Richard M. Bennett, Yanfei Gao

Accepted for the Council:

Carolyn R. Hodges

Vice Provost and Dean of the Graduate School

(Original signatures are on file with official student records.)

Bond Performance of High-Capacity Strands in High Strength Concrete

A Dissertation Presented for the
Doctor of Philosophy
Degree
The University of Tennessee, Knoxville

Xin Jiang

December 2013

Dedication

I dedicate this dissertation to my family and friends for their endless love, support and encouragement.

Acknowledgements

I wish to thank my committee members who are more than generous with their expertise and time. My sincere appreciation goes to my advisor, Dr. Zhongguo John Ma, for offering me the chance to study in his research group. Without his support, encouragement and patience, it is impossible for me to finish my dissertation. Thank you Dr. Edwin G. Burdette, Dr. Richard M. Bennett and Dr. Yanfei Gao for agreeing to serve my committee and offering help to the accomplishment of this dissertation.

My appreciation also goes to Ms. Nancy Roberts and Mr. Larry Roberts for their technical supports and material preparation.

I would also like to thank my colleagues and friends, Dr. Lungui Li, Dr. Peng Zhu, Dr. Qi Cao, Dr. Wenchao Song, Mr. John Cabage, Ms. Jing Song and Ms. Jing Yuan for their help and friendship.

Finally, my profound thanks are given to Tennessee Department of Transportation (TDOT), National Science Foundation (NSF), The China Scholarship Council (CSC), and Center for Transportation Research (CTR) for their financial support.

Abstract

18-mm-diameter (0.7-in.) strand has the ability to introduce almost twice the prestressing force of 13-mm-diameter (0.5-in.) strand and 135% of the prestressing force of 15-mm-diameter (0.6-in.) strand, which could result in a significant increase in the span capacity of the current AASHTO bulb tee girders without having to modify the sections or acquire new forms. To date, the information regarding the bond performance of 18-mm-diameter (0.7-in.) prestressing strand is very limited, preventing its application despite its attractive high-strength. Also, our understanding of the bond mechanism is incomplete and non-quantitative; a rational understanding of the bond mechanism would help predict the bond behavior and develop design guidelines. Therefore, this study concentrated on these two topics. The finite element method was applied to simulate the bond between the prestressing strand and concrete. A parametric analysis was conducted to analyze the factors affecting transfer length. With the comparison of the non-pretensioned and pretensioned pull-out tests, the contribution of each bond mechanism was quantitatively analyzed. The tests indicated that the bond performance was dependent on the specimen length and the pretension level, and the pretension force significantly affected the transfer length.

Table of Contents

List of Tables

List of Figures

Chapter 1 : Introduction

Pretensioned members such as I-girders and bulb tees are widely used in the construction of bridges. Currently the strand diameters used in these members are predominantly 13-mm (0.5 in.) and 15-mm (0.6 in.). In sections like AASHTO I-girders and bulb tees, the area in the bottom flange to accommodate the strands is limited. Using 18-mm-(0.7-in.-) diameter strands can significantly decrease the required number of strands in a given section for an equivalent span capacity. Alternatively, an equal number of the 18-mm diameter strands can be used to accommodate longer spans for a given section with higher concrete strength. Further, an increased roadway clearance can possibly be achieved by using shallower members. States like Tennessee use AASHTO bulb tee (BT) sections which have very limited room in the bottom flange when compared to Nebraska University (NU) sections. Using larger diameter strands helps in increasing the span capacity of the girders without increasing the number of strands in the bottom flange of the section. Thus, these states which are using the bulb tee sections can obtain longer spans without switching over to NU sections or changing their form work. The BT sections with 18-mm-(0.7-in.-) diameter UHS strands prevent them from making extensive changes to the design and fabrication procedures.

Despite the great advantage and attractiveness of using 18-mm-diameter strands, the research conducted on these ultra high strength strands is very limited. The Pacific Street Bridge over I-680 in Omaha, Nebraska, is the first bridge in the United States to use 18-mm-(0.7-in.-) diameter strands in the pretensioned concrete girders (Schuler 2009). Ma and Burdette (2011) analyzed the transfer length and girder end confinement of AASHTO BT girders with 18-mm-(0.7-in.-) diameter strands. Morcous et al. (2012)

conducted a number of tension tests to investigate the mechanical properties of 18-mm-(0.7-in.-) diameter strands. Also, they tested 58 strand specimens using the North America Strand Producers (NASP) test method and demonstrated that the bond of 18-mm-(0.7 in.-) diameter strands was proportional to the concrete strength. However, information about the bond performance of 18-mm-(0.7-in.-) diameter strands in high strength concrete is still limited.

Bond, by definition, refers to the interaction and transfer of force between steel strands and concrete. Without the bond, the pretensioned concrete members would not be possible. For pretensioned concrete members, the anchorage and development of prestressing force exclusively depends on the bond after the release of strands. The bond in pretensioned concrete members may be categorized as the transfer bond and the flexural bond, as shown in Figure 1.1. The transfer bond exists at the release of the prestressing strand through the transfer of the prestress force from the strand to the concrete in the end zone; the transfer length, Lt, is the distance from the end of the concrete to the point where the strand stress reaches a constant level, the effective prestress after losses, fse. The flexural bond starts acting when the external loads are applied and causes the increase of the strand stress and concrete cracking, the flexural bond length is the distance from the end of the transfer length to a point at which the ultimate stress can be developed. In essence, bond controls the behavior of the pretensioned concrete members; thus, the effect of bond is of great interest.

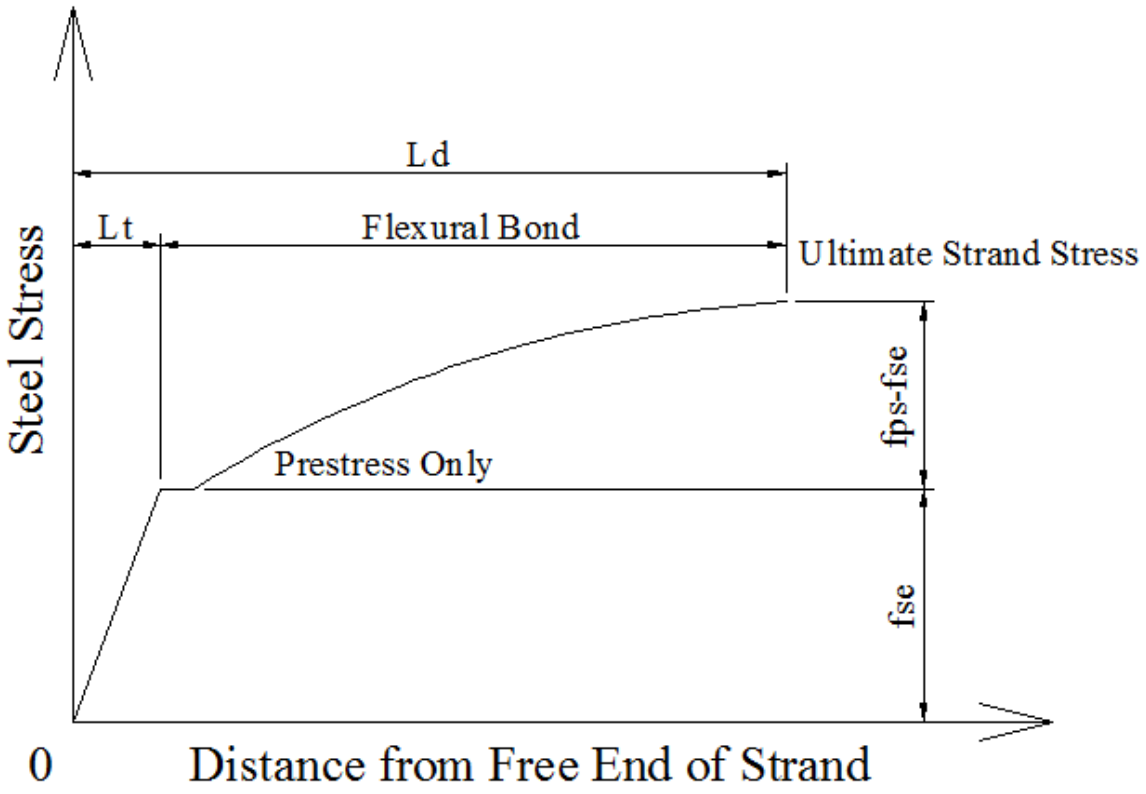

Figure 1.1 Variation of prestressing steel stress

Extensive research on the transfer bond and flexural bond has been conducted parametrically. There are a number of variables affecting the bond: strand diameter, strand location and spacing, strand release method, strand surface condition, concrete strength, concrete cracking, concrete age, curing condition and so on. Janney (1954) tested prestressed concrete prisms to determine the distribution of prestress transfer bond when the strand was released. The short beam specimens were three-point-loaded to failure to investigate the flexural bond. The effect of the diameter and surface condition of the steel wire and the concrete strength were studied. Hanson and Kaar (1959) conducted an investigation of flexural bond in 47 beams pretensioned with seven wire strands. The effect of the embedment length and diameter of strand on the bond

performance was studied. Stocker and Sozen (1970) conducted 486 tests of simple pull-out specimens with short embedment lengths. Basic information on the relationship between bond and slip was provided. A number of variables were investigated: size of strand, concrete, lateral confining pressure, and time effect. A hypothesis on the nature of bond for plain wire and strand was developed, and a simple conceptual model was proposed to explain the bond characteristics. Abrishami and Mitchell (1993) studied the bond characteristics of pretensioned strand along the transfer length and the development length. The average bond stress was directly obtained from measured force in the strand rather than the strains measured on the strands or concrete surface. Tabatabiai and Dickson (1993) investigated the history of the development length equation, detailing how the equation was formulated.

However, the understanding of the nature of bond is still incomplete because the sources of bond are microscopic in nature. Bond originates from chemical adhesion, friction and mechanical interlock between the strand and concrete. A rational understanding of the bond mechanism would help reduce the amount of required testing and develop guidelines for the design of pretensioned concrete members. A general concept of bond is discussed by the previous research (Leonhardt, 1964; Stocker and Sozen, 1970; Russell and Burns, 1993). Very little effort has been made to quantify the elements of bond mechanism. Due to the rigid brittle behavior of the adhesion bond, it disappears as soon as the relative slip occurs between the strand and the surrounding concrete. The slip within the concrete members cannot be directly detected or measured, causing difficulty in quantifying its contribution. This component is ignored in most cases. Friction, a recognized main component of bond, is of large variability and unpredictability.

According to classic Column friction theory, there are two main factors creating the friction: normal pressure and friction coefficient. Normal pressure is hard to obtain at the interface, and its distribution along the strand and around the strand is complicated. Furthermore, the friction coefficient is dependent on the surface condition of the strands, causing the large variability. Mechanical interlock is attributed to the normal force, friction coefficient between the strand and the concrete, and the pitch angle of the outer wires of the strands. Therefore, it is very difficult to quantify its contribution to the bond although it is traditionally regarded as the largest contributor to the flexural bond.

To date, information regarding the 18-mm-(0.7-in.-) diameter prestressing strand is very limited, preventing its wide application despite its attractive high-strength. Our understanding of the bond mechanism is incomplete and non-quantitative; a rational understanding of the bond mechanism would help to predict the bond behavior and develop design guidelines. The two topics described above are vital to the application of the 18-mm-(0.7-in.-) diameter strand in practice and are of interest to this study. Therefore, this study concentrates on these two topics and is outlined as follows. First, the finite element method is applied to simulate the bond between the prestressing strand and concrete. A parametric analysis is conducted to analyze the factors affecting transfer length. Next, six traditional pull-out tests of non-pretensioned specimens are conducted. The effect of the specimen length on the bond behavior, especially on the failure mode, is discussed. Then, nine pull-out tests of pretensioned specimens are carried out. How the pretension level affects the bond performance is revealed. Finally, with the comparison of the non-pretensioned and pretensioned pull-out tests, the bond mechanism is quantitatively analyzed. With the finite element analysis and the experimental results, the

bond performance of the 18-mm-(0.7-in.-) diameter strand in high strength concrete is studied.

Chapter 2 : Finite Element Analysis of the Bond Performance

For the purpose of a better understanding of the bonding mechanism, the influence of different variables on the stress distribution in strands and surrounding concrete, and the effect of debonding on the performance of pretensioned concrete girders with 18-mm-(0.7-in.-) diameter strand, a finite element (FE) analysis was conducted with ABAQUS. Both the fully bonded model and the partially bonded model were analyzed. In the former fully bonded model, no slip between strand and concrete occurred, while the bond simulation in the latter, with consideration of relative slip, was based on the Coulomb friction model. The distribution of concrete strain, the transfer length and the slip of strand at the end of the girder were studied. By comparing the result of FE modeling and the measured transfer length in the previous experiment, the effect of friction coefficient of the strand was evaluated, and the FE models were validated. The debonding FE model was established on the validated partially bonded model. A parametric analysis was conducted, focusing on the impact of friction coefficient and the debonding length in the end of girders.

2.1 Introduction

Traditionally, the Tennessee Department of Transportation (TDOT) has been using AASHTO-PCI BT sections for its concrete bridges. These sections have limited bottom flange widths where the prestressing strands are located. To increase span capacities of these sections, other states have adopted a new section with a wider bottom flange width. Producers in the State of Tennessee have raised concerns about the cost of the revised new steel forms to accommodate a new section. As an alternative, research work is underway testing larger diameter strand used in conjunction with high-strength concrete

and standard BT sections as an innovative and cost effective approach to increase girder span capacity. An 18-mm-(0.7-in.-) diameter strand has the ability to introduce almost twice the prestressing force of a 13-mm-(0.5-in.-) diameter strand and 135% of the prestressing force of a 15-mm-(0.6-in.-) diameter strand, which could result in a significant increase in the span capacity of the current BTs without having to modify the sections or acquire new forms.

Strand debonding can be viewed as essentially de-activating part of the reinforcement of the member in order to eliminate perceived excessive compressive or tensile stresses. Debonding can be accomplished by enclosing a predetermined length of strand in a plastic duct to prevent it from bonding to the concrete. When the strand is detensioned at release, the strand's prestressing force is not transferred at the end of the girder, but begins to develop at the end of the duct. The position of the end of the duct could be well into the span of the girder. This debonding moves stress created by the strand away from the end of the girder towards the center where the self-weight of the girder can alleviate it. The interaction between concrete and strands is complicated. The bond can be attributed to adhesion, mechanical interlock and friction, depending on the extent of bond development and the nature of the strand surface. For the purpose of a better understanding of the bonding/debonding mechanism, the influence of different variables on the stress distribution in strands and surrounding concrete, and the effect of debonding on the performance of prestressed concrete girders, finite element analysis is commonly conducted with some general FE software. Kannel et al. (1997) studied the end cracking of a pre-tensioned I-shape girder numerically and experimentally. Three-dimensional (3D) FE models were established, in which strands were simulated with truss elements and

materials were assumed linear elastic. Also, they evaluated the effect of strand debonding. They concluded that strand cutting order affected the stress distribution in the girder end, and appropriate debonding was beneficial for crack control. Baxi (2005) presented an in-depth analytical study of the bond behavior of strands in the end zone of pre-tensioned concrete girders. An axi-symmetric FE analysis of concrete cylinders using ABAQUS was conducted to investigate the state of stress in the concrete surrounding the strands just after transfer of prestress. Based on the FE program DIANA, Bolmsvik and Lundgren (2006) studied the bond mechanism between strands and concrete and how different detailing of the strand interface affected the behavior. A bond model was calibrated by use of pull-through tests.

One objective of this research was to analyze the effect of debonding of 18-mm-(0.7-in.-) diameter strand through 3D FE modeling. A parametric analysis was conducted and two factors were investigated. One was the friction coefficient of the strand; the other was the debonding length. The distribution of concrete strain, the transfer length, and the slip of strand at the end were studied to better understand the bonding/debonding mechanism.

2.2 Modeling of Bond Behavior

As previously discussed the bond can be attributed to adhesion, mechanical interlock, and friction, depending on the extent of bond development and the nature of the strand surface. The concrete around the strand is in a tri-axial state. To better understand the bonding/debonding mechanism and the influence of different variables on the strain distribution and the slip of strands, three-dimensional (3D) finite element (FE) models were established with ABAQUS. Both the prestressing strand and the concrete were simulated by eight-node linear solid elements with reduced integration (C3D8R). The

process of force transfer from a tensioned strand to the surrounding concrete was simulated by defining an “initial stress” in ABAQUS.

Both the fully bonded and the partially bonded models were simulated. In the fully bonded model, the prestressing strand and the concrete were fast tied and no slip between strands and concrete occurred. The interaction was simulated by “tie” in ABAQUS. With the “tie” constraint, there was no relative movement between the two separate surfaces. The fully-bonded model was an ideal model in which a perfect bond was assumed.

On the other hand, in the partially bonded model, the relative slip at the interface between the strand and concrete was considered. The interface was modeled with “surface-to-surface contact” capable of simulating both the normal behavior and the tangential behavior. The normal behavior was set as “hard contact”, which meant the pressure existed between surfaces and the strand and concrete surfaces cannot penetrate into each other. In the longitudinal direction, the Coulomb friction model was introduced. The Coulomb friction model defined a critical shear stress which was the product of the pressure and the coefficient of friction. Apparently, the friction coefficient controlled the bond-slip behavior and the strain/stress distribution in concrete and strands.

As for a perfect debonding, the bond strength between debonded strands and surrounding concrete shall be zero, and the prestress force will not transfer to concrete in the debonded region. In this article, the modeling of debonding was based on the partially bonded model in which the interface was modeled with “surface-to-surface contact”. In the case of debonding using preformed tube, the tangential behavior at the interface between the debonded strand and its surrounding concrete was set as “frictionless”, indicating no friction between surfaces in the debonded region. In the case of debonding

using split sheathing, weak bond strength at the interface was considered by introducing a low friction coefficient.

2.3 Parametric Analysis of Partially Bonded Models

Parametric analysis was conducted based on the FE models with ABAQUS. In this section, the influence of friction coefficient on the bond behavior was studied. To capture the bond mechanism based on the Coulomb friction model, a prestressed concrete cylinder girder with 18-mm-(0.7-in.-) diameter strand was modeled with ABAQUS. The cylinder was 144 in. (3658 mm) long, and its diameter was 6 in (152 mm). The strand was located at the center of the cylinder. The modulus of elasticity of concrete was 6641 ksi (45788 Mpa) and the Poisson's ratio was 0.2 through a series of small scale experiments. The modulus of elasticity of 18-mm-(0.7-in.-) diameter strand was 28800 ksi (198569 Mpa) and the Poisson's ratio was 0.3. The cross section area of the strand was 0.294 $in.^2$ (189.677 mm^2), and the ultimate strength was 270 ksi (1862 Mpa). The "initial stress" was 202.5 ksi (1396.2 Mpa) which was 75% of the ultimate strength. The mesh of the FE model was shown in Figure 2.1. The X axis and the Y axis were the radial direction, and the Z axis was the longitudinal direction of the cylinder. Because the cylinder girder was symmetric, a model of a half-length (72 in. or 1829 mm) and ¼ cross section was simulated to decrease the number of FE elements. The boundary conditions were that the three planes (plane X = 0, plane Y = 0 and plane Z = 0) were symmetric.

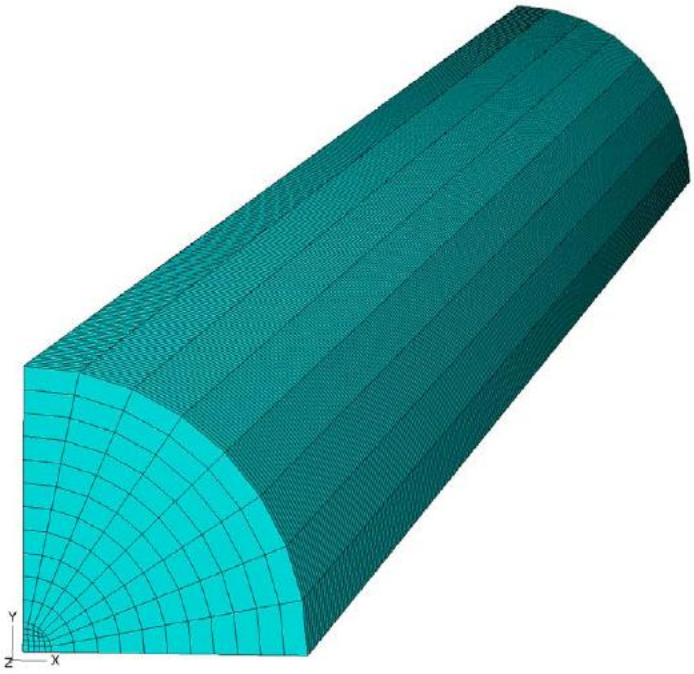

Figure 2.1 FE Model of cylinder girder

Burgueno and Sun (2011) calibrated the friction coefficient of 15-mm-(0.6-in.-) diameter strand through a series of small scale experiment. The friction coefficient varied from 0.23 to 0.7. Because the friction coefficient of 18-mm-(0.7-in.-) diameter strand was not available, a series of prestressed concrete cylinder girders with different friction coefficients were studied. There were six cylinder models. One was the fully bond (FB) model in which strand and concrete were tied fast without any relative slip, the other five models were partially bonded models. The friction coefficients of the partially bonded (PB) models PB030, PB040, PB050, PB060 and PB070 were 0.30, 0.40, 0.50, 0.60 and 0.70, respectively. The distribution of the longitudinal strain (EE33) in concrete of the partially bonded model PB040 was shown in Figure 2.2. It revealed that EE33 increased gradually from the cylinder end to the middle span. The maximum principal strain in the beam end was shown in Figure 2.3. The Hoyer's effect was captured in the wedge-shaped

strain contour. The red strain contour in Figure 2.3 revealed a maximum strain area located at the end of the cylinder. The maximum principal strain along the radial direction at three sections were investigated, as shown in Figure 2.4. At each section, the maximum strain occurred at the interface of strand and concrete, and the strain decreased along the radial direction. Within all three sections, the maximum strain was 990 microstrain. When the distance away from the center of prestressed strand was greater than 1 in. (25.4 mm), the strain decreased to less than 200 microstrain. It revealed that the strand dramatically transferred the prestressing force to the surrounding concrete within 1 in. (25.4 mm), indicating 2 in. (50.8 mm) spacing of adjacent strands could be appropriate.

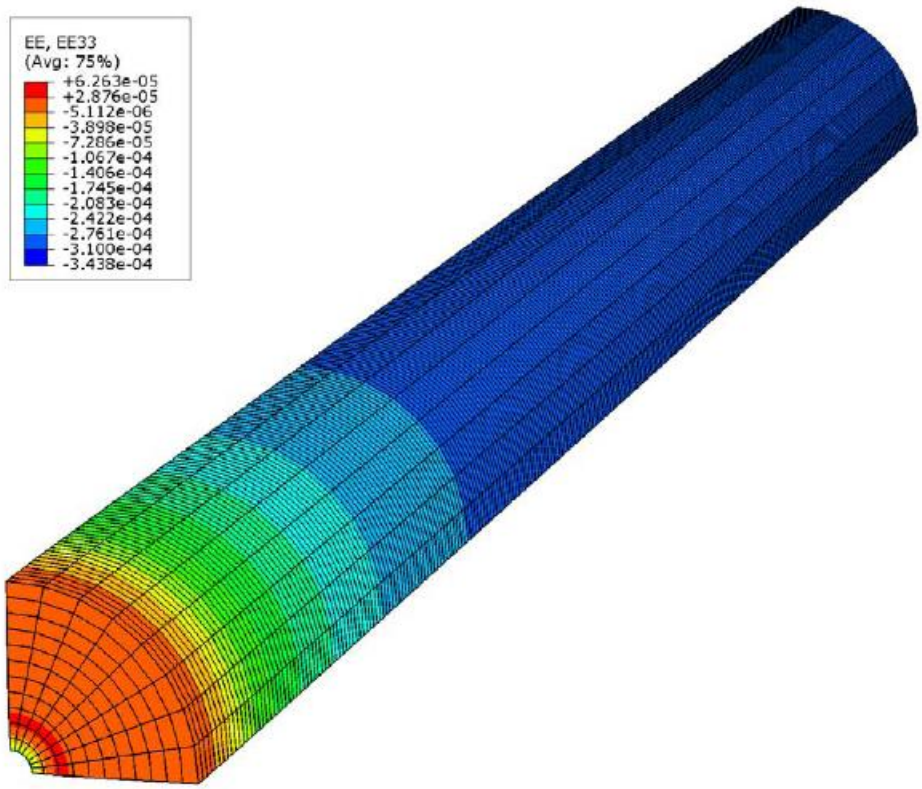

Figure 2.2 Distribution of EE33 in concrete

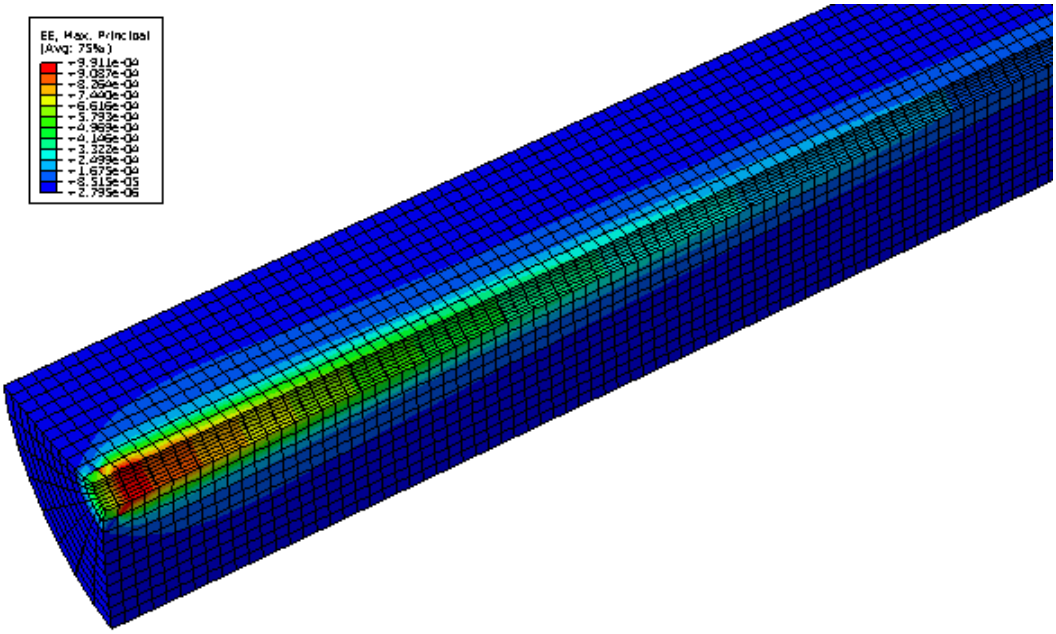

Figure 2.3 Distribution of maximum principal strain in concrete

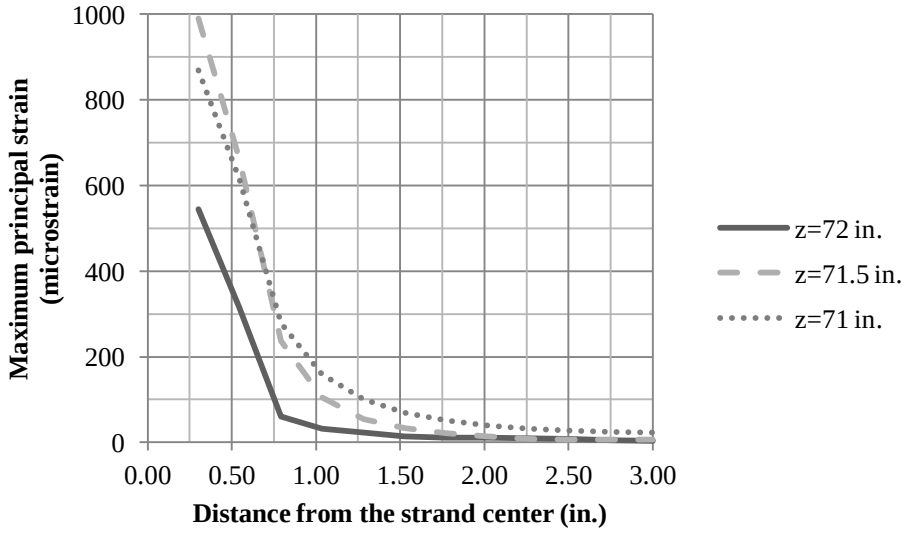

Figure 2.4 Maximum principal strain along radial direction; 1mm = 0.039 in.

Strain EE33 in the outer concrete surface along the cylinder was shown in Figure 2.5. In the fully bonded model, EE33 approximated to the maximum within 4 in. (101.6 mm). In the partially bonded model PB040, EE33 reached the plateau of maximum strain within a longer distance although the maximum EE33 in both models was the same. The distribution of EE33 revealed how the force transferred from the tensioned strand to the surrounding concrete. In the transfer length experiment, the 95% average maximum strain (AMS) method was adopted by Russell and Burns (1996). The AMS is the average of all the strains on the plateau of the longitudinal concrete strain curve. In this article, 95% AMS method was also adopted to analyze the transfer length. The result was shown in Figure 2.6. The transfer length of the model PB030, PB040, PB050, PB060 and PB070 were 27.50, 20.75, 16.75, 14.25 and 12.00 in. (698.50, 527.05, 425.45 and 304.80 mm) respectively. Apparently, the transfer length decrease with the increase of the friction coefficient. According to AASHTO LRFD Specification, the transfer length depends on the diameter of the strand. As for the 18-mm-(0.7-in.-) diameter strand, the transfer length would be 42 in. (1066.8 mm) if AASHTO LRFD equation was used. However, our previous experiment revealed the transfer length for 18-mm-(0.7-in.-) diameter strand was about 21 in. or 533.4 mm (Ma and Burdette 2011). By comparison, the FE result of PB040 was very close to the experimental result, indicating that 0.40 was an appropriate friction coefficient for this strand. In the fully bonded model, the transfer length was extremely low although the transfer length was theoretically expected to be zero due to the perfect bond. In addition, the tensioned strand tended to slip back into concrete after the prestress force was transferred. Thus, the slip of the strand at the end for all models was studied and the result was shown in Figure 2.7. The slip of the model PB030, PB040,

PB050, PB060 and PB070 was 0.06, 0.05, 0.04, 0.03 and 0.03 in. (1.52, 1.27, 1.02, 0.76 and 0.76 mm). It revealed that the slip at the end decreased with the increase of friction coefficient.

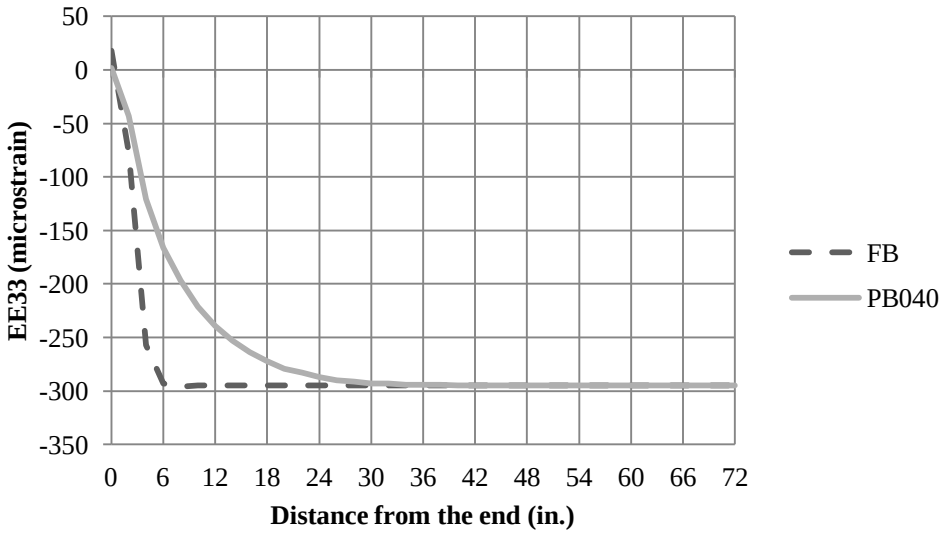

Figure 2.5 EE33 in bond models; 1mm = 0.039 in.

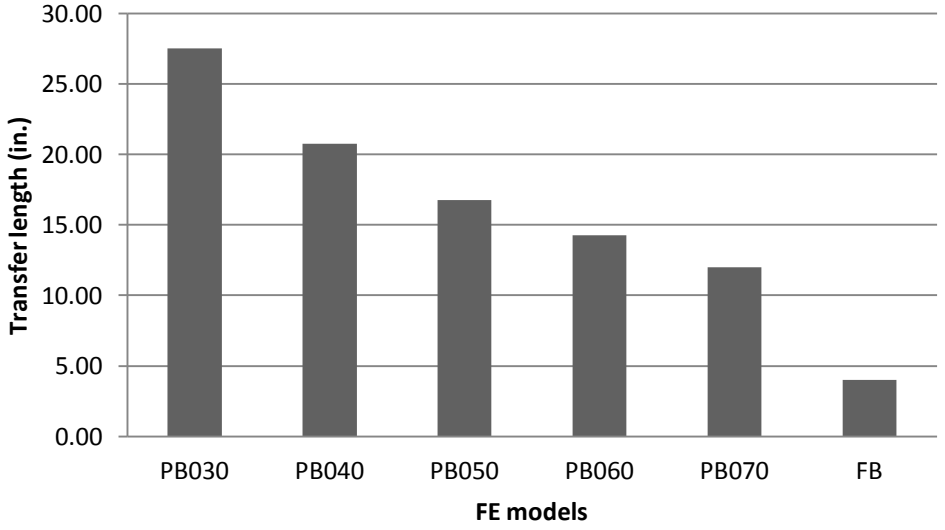

Figure 2.6 Transfer length of FE bond models; 1mm = 0.039 in.

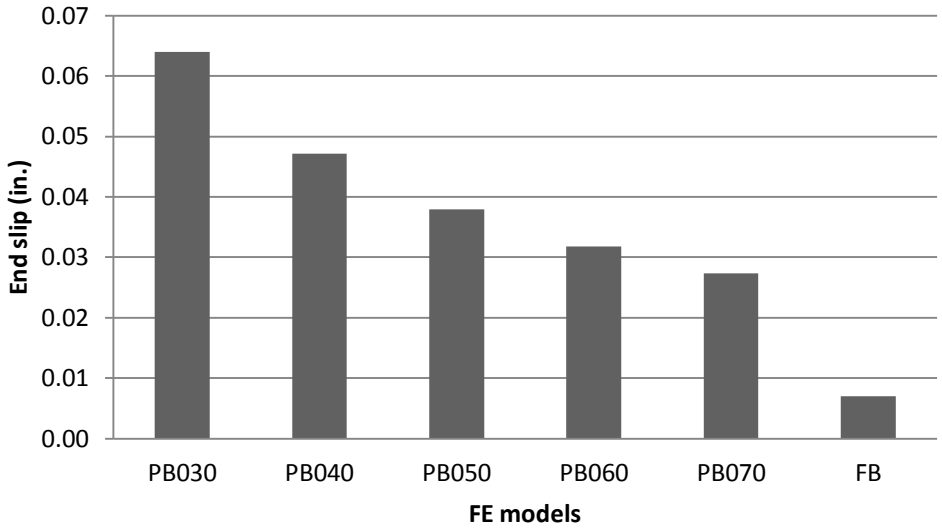

Figure 2.7 End slip of FE bond models; 1mm = 0.039 in.

2.4 Parametric Analysis of Debonding

The simulation of debonding was based on the mentioned partially bonded model. As discussed before, the transfer length in the FE model PB040 was very close to our previous experimental result. Therefore, for the prestressed strand in the bonding region, 0.40 was an appropriate friction coefficient of 18-mm-(0.7-in.-) diameter strand. For the strand in the debonding region, the friction coefficient of the debonded strand was different due to the different debonding methods. Also, the influence of debonding length was studied. The details of all nine debonding models were given in Table 2.1. The debonding model was named according to the debonding length and the friction coefficient in the debonding region. For example, the model 1-05 meant that the debonding length was 1 ft. (304.8 mm) and the friction coefficient was 0.05. All debonding models were categorized into three series according to the different friction coefficient in the debonding region. Series-00 included the debonding model 1-00, 2-00

and 3-00. Series-05 included the debonding model 1-05, 2-05 and 3-05. Series-10 included the debonding model 1-10, 2-10 and 3-10.

Table 2.1 Details of nine debonding FE models

Debonding Model Name	Debonding Length (in.)	Friction coefficient in the Debonding region
1-00	12	No friction
1-05	12	0.05
1-10	12	0.10
2-00	24	No friction
2-05	24	0.05
2-10	24	0.10
3-00	36	No friction
3-05	36	0.05
3-10	36	0.10

1 mm = 0.039 in.

For all nine debonding models, strain EE33 in the outer concrete surface along the cylinder was shown in Figure 2.8, Figure 2.9 and Figure 2.10. The distribution of strain EE33 of all nine debonding models was also compared with that of PB040 in which there was no debonding. As shown in Figure 2.8, the slope of EE33 curve of Series-00 in the end debonding region was zero. As shown in Figure 2.9 and Figure 2.10, the slope of EE33 curve of Series-10 in the debonding region was greater than that of Series-05. It revealed that the slope of EE33 in the debonding region increased with the increase of the friction coefficient.

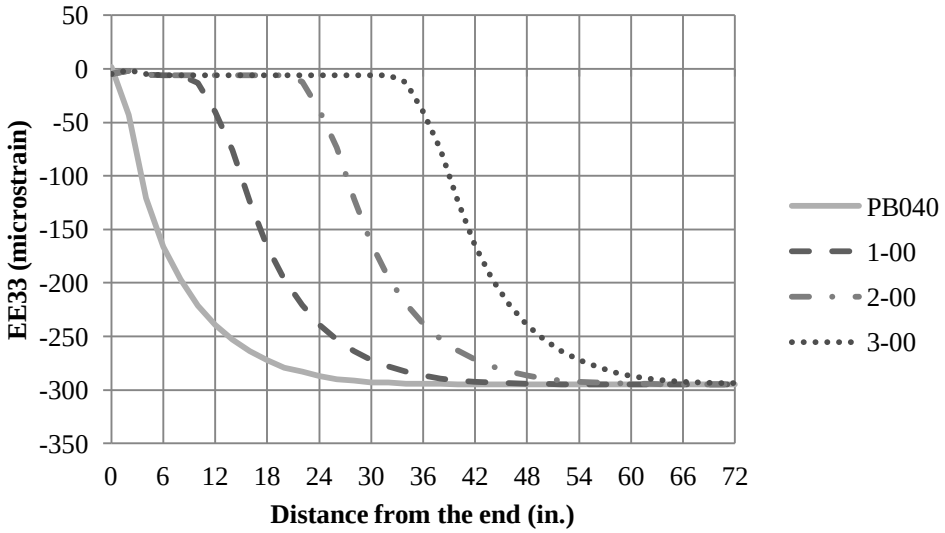

Figure 2.8 EE33 in debonding models series-00; 1mm = 0.039 in.

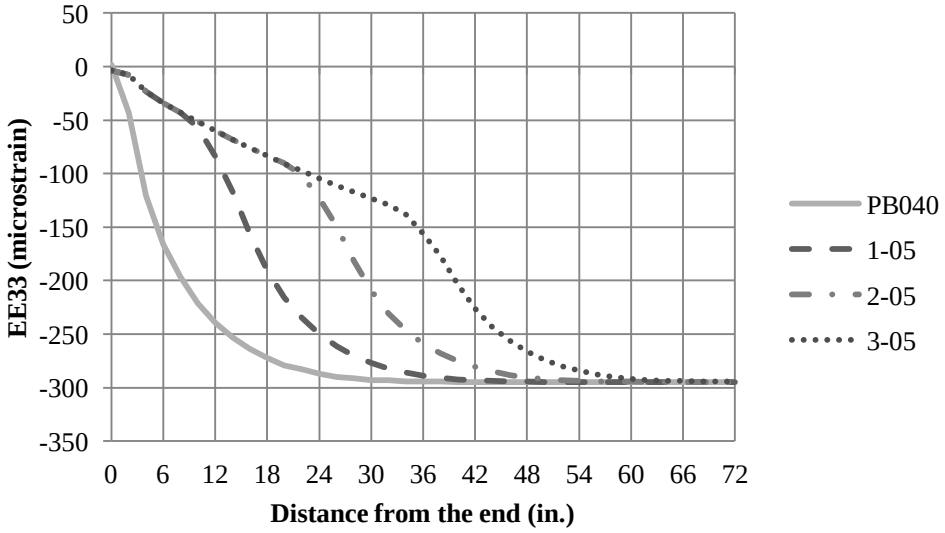

Figure 2.9 EE33 in debonding models series-05; 1mm = 0.039 in.

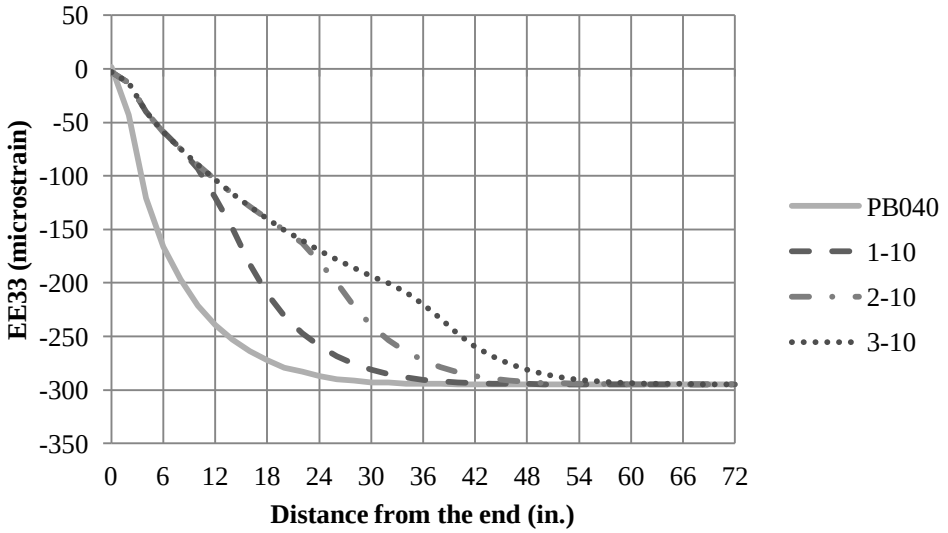

Figure 2.10 EE33 in debonding models series-10; 1mm = 0.039 in.

The transfer length for all debonding models was also calculated with the 95% AMS method. The result is shown in Figure 2.11. The transfer length increased with the decrease of debonding length and the decrease of friction coefficient, indicating that the friction at the interface in the debonding region contributed to the force transfer. When the friction coefficient was zero, the transfer length of all debonding models was the same as that of PB040, indicating that a perfect debonding did not change the transfer length of the strands. For the cases of 36 in. (914.4 mm) debonding, when the friction coefficient was 0.10, the transfer length approximated to 11.75 in. (298.45 mm). By comparison, this transfer length was about a half of the transfer length of the FE model PB040. Also, the friction coefficient and the debonding length affected the end slip, as shown in Figure 2.12. The end slip increased with the increase of debonding length and the decrease of friction coefficient.

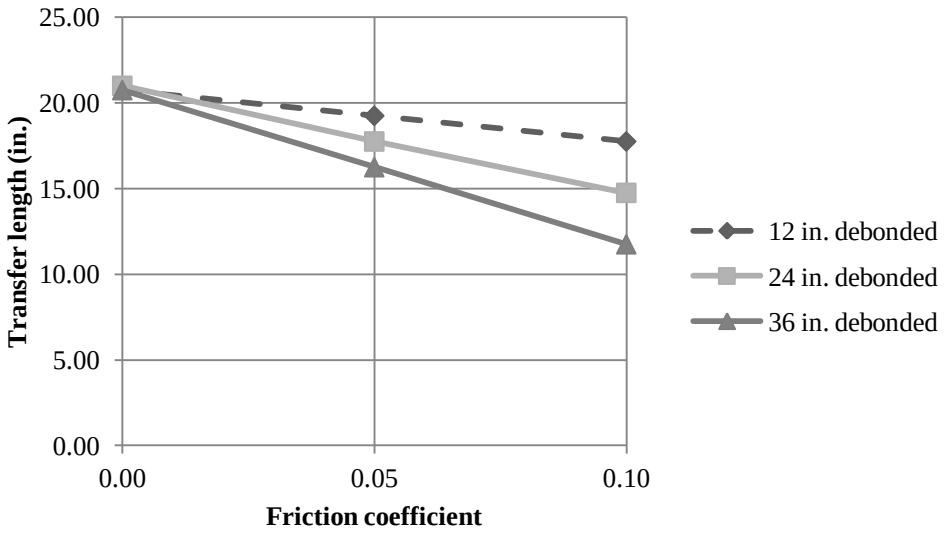

Figure 2.11 Transfer length of FE debonding models; 1mm = 0.039 in.

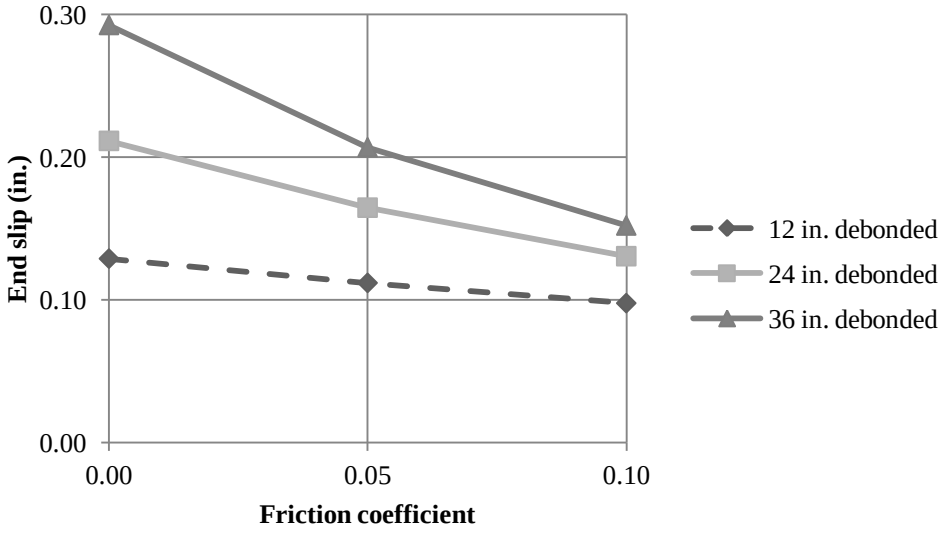

Figure 2.12 End slip of FE debonding models; 1mm = 0.039 in.

2.5 Conclusions and Discussion

FE modeling was used to analyze the performance of pretensioned concrete girders with 18-mm-(0.7-in.-) diameter strand. Both fully bonded and partially bonded models were investigated. The measured transfer length in the previous test validated the partially bonded model with an appropriate friction coefficient. The change of concrete strain along the radial direction revealed that the strand dramatically transferred the prestressing force to the surrounding concrete within 1 in. (25.4 mm), indicating 2 in. (50.8 mm) spacing of adjacent strands could be appropriate. In the parametric analysis of the partially bonded models, the transfer length increased with the decrease of the friction coefficient, and the slip at the end increased with the decrease of friction coefficient. The parametric analysis of the debonding models revealed that the transfer length increased with the decrease of debonding length and the decrease of friction coefficient when the friction coefficient was not zero. As for a perfect debonding in which there is no friction between strand and concrete, the debonding length has no effect on the transfer length. The end slip increased with the increase of debonding length and the decrease of friction coefficient.

Currently, the FE analysis is focused on the performance of pretensioned concrete girders at transfer. In the future, FE modeling will be conducted to analyze the flexural and shear behavior of AASHTO-PCI BT Girders with 18-mm-(0.7-in.-) diameter strands. Full-scale girder test will be conducted and the experimental results will be used to evaluate the FE modeling. In addition, a numerical bonding/debonding model based on the relationship of slip and bond stress will be proposed to further understand the bonding/debonding mechanism.

Chapter 3 : Material Properties and Pull-out Tests of Non-pretensioned Specimens

An experimental program was conducted to investigate the bond performance of non-pretensioned 18-mm-(0.7-in.-) diameter strand in high strength concrete. The mechanical properties of the strand and the concrete were obtained through strand tension tests and concrete compression tests. Six pull-out tests were conducted on prismatic specimens made with a non-pretensioned strand embedded in the center of the concrete without reinforcement. These specimens had different strand embedment lengths: 0.5 Lt (transfer length), 1.0 Lt and 1.5 Lt of the 18-mm-(0.7-in.-) diameter strand. The relationship between the strand slip and the pull-out force, the stress distribution along the strand, and its development with the pull-out force were investigated. The results of the pull-out tests indicate that the bond behavior is significantly affected by the strand embedment length. The failure of the specimens of 0.5 Lt, 1.0 Lt and 1.5 Lt was sudden concrete splitting, significant strand slip and rotation, and strand break at the chuck, respectively. A series of typical curves of the pull-out force versus the strand free end slip are given to describe the characteristic of the bond behavior for specimens with different strand embedment length.

3.1 Introduction

Pretensioned members such as I-girders and bulb tees are widely used in the construction of today's bridges. Currently, the strand diameters used in these members are predominantly 13-mm (0.5-in.) and 15-mm (0.6-in.). In sections like AASHTO I-girders and bulb tees, the area in the bottom flange to accommodate the strands is limited. Using 18-mm-(0.7-in.-) diameter strands can significantly decrease the required number of strands in a given section for an equivalent span capacity when used at the same spacing.

Alternatively, an equal number of the 18-mm-(0.7-in.-) diameter strands can be used to accommodate longer spans for a given section with higher concrete strength. Further, an increased roadway clearance can possibly be achieved by using shallower members. Many States use AASHTO bulb tee (BT) sections. These sections have very limited room in the bottom flange when compared to other I-girder sections. Using larger diameter strands help in increasing the span capacity of the girders without increasing the number of strands in the bottom flange of the section. Thus, States that use bulb tee sections can obtain longer spans without requiring a manufacturer formwork change. The BT sections with 18-mm-(0.7-in.-) diameter strands enable prestress girder manufacturers to create more efficient girder designs without requiring extensive changes in design and fabrication procedures.

Despite the great advantage and attractiveness of using 18-mm-(0.7-in.-) diameter strands, studies examining the design and use of these strands have been limited. Some examples though are as follows: The Pacific Street Bridge over I-680 in Omaha, Nebraska, was the first bridge in the United States to use 18-mm-(0.7-in.-) diameter strands in the pretensioned concrete girders (Schuler 2009). Song et al. (2013) analyzed the transfer length and girder end confinement of AASHTO BT girders with 18-mm-(0.7-in.-) diameter strands. Morcous et al. (2012) conducted a number of tension tests to investigate the mechanical properties of 18-mm-(0.7-in.-) diameter strands. Also, based on the North America Strand Producers (NASP) test, they demonstrated that the bond of 18-mm-(0.7-in.-) diameter strands was proportional to the concrete strength.

Bond, by definition, refers to the interaction and transfer of force between steel strands and concrete. In the 1950's, Guyon (1953) demonstrated that bond developed between

pretensioned strand and concrete, and Janney (1954) investigated the transfer bond and flexural bond based on prism tests and beam tests and analyzed the effect of steel wire diameter on bond. Extensive research (Brearley and Johnston 1990; Logan 1997; Rose and Russell 1997) has been conducted on 13-mm-(0.5-in.-) and 15-mm-(0.6-in.-) diameter strands which currently are widely used. However, information on the bond performance of 18-mm-(0.7-in.-) diameter strands in high strength concrete is unavailable, no ASTM standard test method exists, and the current AASHTO specifications (2012) are not applicable for 18-mm-(0.7-in.-) diameter strand. Since this is a new product with promising benefits, the mechanical properties of minimum embedment length and a prediction of bond behavior in the flexural beam tests are required before this product can be reliably used.

A simple pull-out testing procedure was used to study the bond characteristics of 18-mm-(0.7-in.-) diameter strand. This procedure serves as a predictor for full-scale transfer and flexure development tests. Specimens of three different lengths (0.5 transfer length (Lt), 1.0 Lt, and 1.5 Lt) were cast with 18-mm-(0.7-in.-) diameter strand and high strength concrete. Using the pull-out test procedure, the relationship between strand slip and pull-out force, along with the concrete surface strain distribution along the strand and its development with force was investigated. The different failure modes of the pull-out tests are also discussed. Existing pull-out studies have not quantified the effect of the strand embedment length upon bond; however, results of earlier research indicate that the strand embedment length affects the bond behavior significantly. This investigation of the relationship between the strand embedment length and the failure mode of the pull-out

tests provides a new way to determine the transfer length and will serve as a basis in predicting bond performance in flexural beam tests.

3.2 Research Significance

The lack of research on the bond performance of the 18-mm-(0.7-in.-) diameter strand prevents the wide application of this strand despite its increased efficiency attractiveness. Thus, a thorough study of the bond characteristics of this strand in high strength concrete is necessary and important to provide guidelines for design. Also, there is no current standard testing method to evaluate the bond strength for this strand. For the strands of smaller size, pull-out tests are applied to short specimens to determine bond properties. However, these tests do not consider the effect of strand embedment length; which our study shows significantly affects bond behavior. In this research, three different strand embedment lengths were used: 0.5 Lt, 1.0 Lt, and 1.5 Lt. Different bond behaviors for these specimens were analyzed in this research.

3.3 Material Properties

3.3.1 18-mm-(0.7-in.-) diameter strand

The 18-mm-(0.7-in.-) diameter, Grade 1860 (270 ksi) strands used in this study were uncoated seven wire low-relaxation strands with a nominal area of 190 mm^2 (0.294 in^2). By comparison, the nominal area of 13-mm-(0.5-in.-) diameter strand is 99 mm^2 (0.153 in^2) and that of 15-mm-(0.6-in.-) diameter strand is 140 mm^2 (0.217 in^2). Thus, the nominal area of the 18-mm-(0.7-in.-) diameter strand is 92% larger than that of the 13-mm-(0.5-in.-) diameter strand and 35% larger than that of the 15-mm-(0.6-in.-) diameter strand. Accordingly, the ultimate strength of the 18-mm-(0.7-in.-) diameter strand of the same grade is significantly higher. For the 18-mm-(0.7-in.-) diameter strand, the yield

strength is 318 kN (71.5 kips), which is 90% of ultimate tension strength. The nominal breaking strength is 353 kN (79.4 kips) and the minimum load at 1% extension is 318 KN (71.5 kips). The minimum ultimate elongation in 610 mm (24 in.) gauge length is 3.5%. The modulus of elasticity is 196500 MPa (28500 ksi).

Three strand tension tests were conducted using a Tinius-Olson universal test machine in the Laboratory at the University of Tennessee, as shown in Figure 3.1(a). All strand specimens were cut from the same spool. A tensioning chuck was attached to the strand, below which was attached a load cell which electronically recorded the load being applied to the strand. The data from the load cell were compared to the tensile force measured by the universal testing machine to check the calibration of the load cell. The breaking strength of the strands were 346 kN (77.8 kips), 366kN (82.4 kips), 362 kN (81.5 kips), respectively. The average breaking strength was 358 kN (80.6 kips). For all specimens, the modulus of elasticity was approximately 199,948 MPa (29000 ksi). As shown in Figure 3.1 (b), the strand always broke at the chuck along a plane at about 45 degrees to the twist direction. Figure 3.1 (c) shows a typical unraveling of the strand after failure.

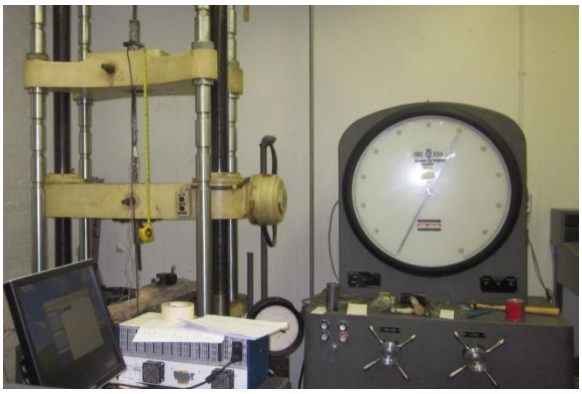

(a) Strand Tension Test

(b) Strand Break at Chuck (c) Strand Unraveling

Figure 3.1 Strand tension test

3.3.2 High strength concrete

High strength concrete (HSC) was used in the test. The concrete mix design is shown in Table 3.1. Cement type III was used to achieve high strength at an early concrete age. No.8 limestone was used as coarse aggregate, and the fine aggregate was manufactured. The water cement ratio was 0.309. Chemical admixtures, including a high-range water-reducing admixture, water reducer and workability-retaining admixture were added to reduce water content, improve early-age compressive strength, and adequate slump without retardation. A series of 152.4 by 304.8 mm (6 by 12 in.) cylinders were cast to

obtain the concrete compressive strength when the prism specimens for pull-out tests were cast. On the first day, these cylinders were sealed with a plastic lid to prevent water loss and then cured with the prism specimens in the same environment. The temperature was 24.4 ^{0}C (76 ^{0}F). On the second day, they were demolded and capped with a sulfur cap. After capping, the cylinders were stored in the moist room where the temperature is 23.3 ^{0}C (74 ^{0}F) and the relative humidity was 100%. The typical failure mode is shown in Figure 3.2. Through compression testing, the average concrete compressive strength at one-day was 58.6 Mpa (8.5 ksi), and the average strength at two-days was 62.7 Mpa (9.1 ksi). All of the failure modes were Type 3 (Columnar vertical cracking through both ends, no well-formed cones) as defined by ASTM C39.

Table 3.1 Concrete mix design (per 1 m^3)

Cement type III	kg	466.1
Coarse aggregate	kg	826.9
Fine aggregate	kg	887.3
Water	kg	144.0
High-range water-reducing admixture	ml	3959.9
Water reducer	ml	1228.9
Workability-retaining admixture	ml	1843.4

1 m^3 = 1.3079 yd^3; 1 kg = 2.2046 lbs; 1 ml = 0.0338 oz

Figure 3.2 Typical failure mode in concrete compression test

3.4 Existing Pull Test Methods

ASTM A981 (2011) prescribes a pull test to evaluate bond strength for 15-mm-(0.6-in.-) diameter steel prestressing strand. The procedure specifies that untensioned strand shall be embedded in grout with compressive strength of 24 to 28 MPa (3500 to 4000 psi) for a bond length of 400 mm (16 in.). Three other tests are also defined for untensioned prestressing strands (Ramirez and Russell 2008). They include the PTI Bond Test, the North American Strand Producers (NASP) Bond test and the Moustafa Test.

For the PTI Bond Test, the strands are pulled out from neat cement mortar; for the NASP test, the strands are pulled out from a mortar consisting of Type III cement, sand and water. The Moustafa Test (Moustafa 1974) is known as Large Block Pull-out Test (LBPT), which consists of 610 mm (24 in.) deep concrete blocks with a length and width dependent upon the number of strands. For both NASP test and LBPT, the embedment length is 457 mm (18 in.). LBPT was used by Logan (1997) and Rose and Russell (1997). With LBPT for both 13-mm-(0.5-in.-) and 15-mm-(0.6-in.-) diameter strands, Logan (1997) stated that LBPT was an accurate predictor of the general transfer and development characteristics of pretensioned members. Ramirez and Russell (2008) found

that the Moustafa and NASP test established the best correlation of a measure of bond quality for strand and measured transfer length.

Obviously, bond performance is different for strands embedded in mortar and strands in concrete. Thus, for the purpose of evaluating the bond performance of strands in pretensioned concrete members, LBPT is more attractive. However, the typical LBPT test only considers one specific stand embedment length, thus the effect of the strand embedment length on the bond behavior cannot be analyzed using only this test.

3.5 Pull-out Specimen Size Consideration

In 1970, Stocker and Sozen (1970) conducted 486 simple pull-out tests on a variety of strand configurations. In 433 specimens, the typical bonded length was only 25.4 mm (1 in.). In the remaining specimens, the bonded length was varied from 13 mm (0.5 in.) to 508 mm (20 in.). The tests were discontinued when the slip reached 3.81 mm (0.15 in.). The tests provided the basic information on the relationship between bond force and slip to understand the nature of bond. A parametric study was conducted to investigate the effect of size of strand, strength, consistency, curing conditions, age, and settlement conditions of concrete, lateral confining pressure, and time effects. Bearley et al. (1990) studied the effects of a grit-impregnated epoxy coating on the bond behavior of strand. The specimens were 203 mm × 203 mm × 305 mm (8 in. × 8 in. × 8 in.) concrete prisms. However, the strand embedded length in these tests was significantly shorter than the transfer length of the strands.

When investigating the bond behavior of prestressing strand within the transfer length, the pull-out tests of very short specimens can only provide very limited information. One objective of this research is to investigate the influence of strand embedded length on the

bond behavior. For 18-mm-(0.7-in.-) diameter strand, the transfer length (Lt) was varied from 610 mm (24 in.) to 788 mm (31 in.). These lengths were chosen to offer a comparison to tests conducted by Morcous et al. (2010). Song et al. (2013) published that the transfer length of 18-mm-(0.7-in.-) diameter strand in an AASHTO type I girder was approximately 533 mm (21 in.). In this research, three different specimen lengths were considered: 305 mm (1 ft.), 610 mm (2 ft.) and 915 mm (3 ft.). These lengths correlate with the aforementioned studies and approximate what is believed to be 0.5, 1.0, and 1.5 times the transfer length.

Two specimens (A and B) were cast for the each specimen length. Thus, a total of 6 specimens (1A, 1B, 2A, 2B, 3A and 3B) were cast for non-pretensioned strand pull-out testing. Each of the specimens was labeled with a two character identification code (ID). The first character represents the specimen length or the strand embedment length (unit: ft.). The second character designates the specimen number. An example prism is 2B, which is 2-foot (609.6 mm) long and is the second specimen tested of that length.

Typical spacing between prestressing stands within girders is 50.8 mm (2 in.). According to Song et al.[2], 50.8 mm (2 in.) spacing is also appropriate for 18-mm-(0.7-in.-) diameter strand. To ensure adequate concrete cover for the strand, a cross section of 152.4 mm (6 in.) by 152.4 mm (6 in.) was selected. The non-pretensioned strand was centered within the cross section and embedded parallel to the prism specimen.

3.6 Specimen Fabrication and Test Set up

The concrete prisms were cast in reusable steel forms. The concrete was consolidated using a vibrator. The prisms were stored in the lab where the temperature was 24.4 ^{0}C (76 ^{0}F). They were covered with two layers: wet burlap and then covered with plastic

sheeting. The prisms were stripped on the next day, and tested on the third day. In this way, the age of concrete on the pull-out test day was 2 days, which was the same for the pretensioned strand pull-out tests addressed in the next chapter.

A DEtachable MEChanical (DEMEC) strain measurement system was used to measure the concrete surface strain. The DEMEC strain points have small metallic discs of 6.35-mm (0.25- in.) in diameter, which were placed along the centerline of the prestressing strands and attached to the both sides of the concrete surfaces. The gage length was 200 mm (7.874 in.). Thus, the average concrete surface strain within the gauge length could be calculated through the change of the distance between two DEMEC strain points. The location of these strain points is shown in Figure 3.3. For the 305 mm (1 ft.) specimen, two DEMEC strain points were symmetrically attached to the concrete surface along the specimen, and the spacing is the gage length 200 mm (7.874 in.). Thus, only one average strain in the middle length could be obtained for one side of the prism. For the 610 mm (2 ft.) and 915 mm (3 ft.) specimens, the spacing of two adjacent points was a half of the gage length and they were symmetrically placed along the specimen length. Thus, 4 strains could be measured for the 610 mm (2 ft.) specimen on each side and 7 strains for the 915 mm (3 ft.) specimen on each side. In the pull-out test, there were two ends: jacking end and free end. Strain 1 is the strain closest to the jacking end while Strain 4 in the 610 mm (2 ft.) specimens or Strain 7 in the 915 mm (3 ft.) specimens is the one closest to the free end.

(a)

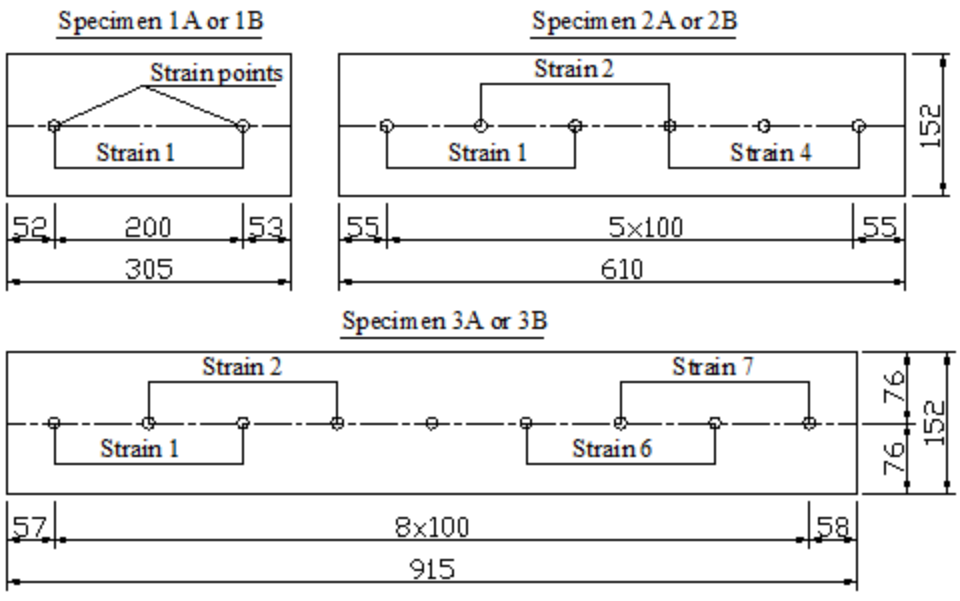

Figure 3.3 Location of the strain points (unit: mm); 1mm = 0.039 in.

A detailed description of the test set-up is given in Figure 3.4. It shows a horizontal steel frame using Hollow Structural Sections HHS$7 \times 7 \times 3/8$ that was anchored to a strong floor with bolts. A hollow hydraulic jack cylinder operated by a manually-controlled pump was used to pull the strand, which was run concentrically through the steel frame and the hollow jack. A doughnut load cell was placed behind the jack, and a chuck was placed against the load cell. Therefore, a pull-out force was created with the elongation of the jack cylinder.

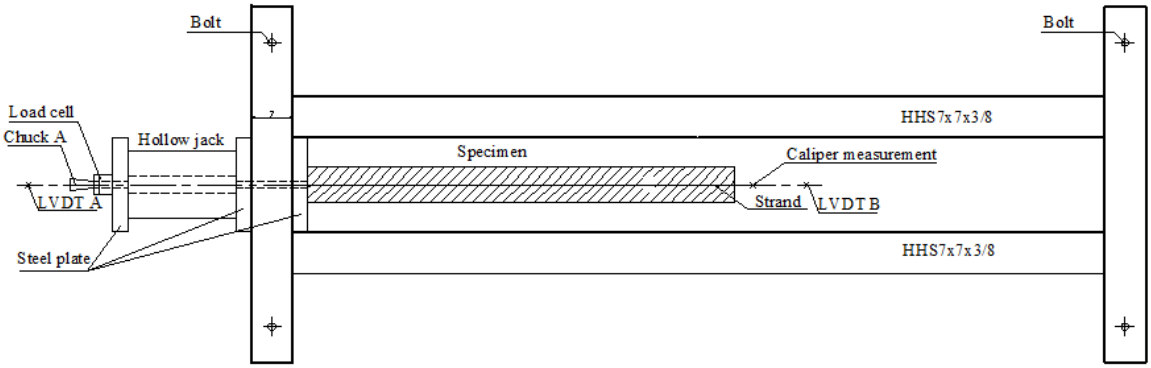

(a) Test setup

(b) Free end slip measurement with LVDT and caliper

(c) Jack elongation measurement with micrometer

Figure 3.4 Test apparatus

The pull-out tests focused on the relationship among pull-out force, the end slip, and the strain distribution. The force was recorded from the load cell. The jack cylinder was manually controlled to increase the pull-out force step-by-step. The pull-out force increased by 22 to 44 kN (5 to 10 kips) for each step. There were two strand end slips: the jacking end slip and the free end slip. Typically, an LVDT (Linear Variable Differential Transducer) was used to record the end slips. A metal hook attached to the strand with tape was connected to the LVDT. To validate the LVDT data, a micrometer was used to measure the jack cylinder elongation reflecting the jacking end slip, and a caliper was used to measure the "draw-in" at the free end of the strand. When the pull-out force was sufficient to induce free end slip, the free end of the strand would rotate, making an accurate measurement of free end slip with the LVDT difficult. The caliper measurement of the draw-in was then used as the free end slip measurement instead of the LVDT reading.

As mentioned previously, the concrete surface strain was taken using the DEMEC strain system. The change of the concrete strain always lagged behind the increase of the pull-out force. If the pull-out force was held constant, the concrete strain would slowly increase with time. But the rate of strain increase extent would decrease with time. Thus, there was a delay of about 3 minutes between strain measurements for each loading step. After the measurement of the concrete strain on two sides, the average concrete surface strain was obtained for each loading step. Typically, one pull-out test was completed within 3 hours.

3.7 Test Results for each Specimen

The pull-out loads versus free end slip and jacking end slip are shown in Figure 3.5 (a) through Figure 3.5 (c). In the legend in Figure 3.5, the first two characters designated the specimen ID; the rest designated the type of slip (free end or jacking end). Due to the significant difference of both the slip and the pull-out force among different specimens, the scale is only the same for the specimens with the same length. The jacking end slip gradually increased as the pull-out force elongated the jack cylinder. In contrast, the free end slip remained zero until the pull-out force increased to a force that caused relative slip along the entire embedded strand.

The development of the concrete surface strains at different locations is shown in Figure 3.6 (a) through Figure 3.6 (f). The location of the measured strain, which is represented by the strain identification number, is already shown in Figure 3.3. For specimen 1A/1B, only strain 1 was obtained which was in the middle of the specimen. For other specimens, the distance of two adjacent strains was 100 mm (3.937 in.), and the measured end strain was approximately 55 mm (2.165 in.) away from the specimen end. Strains 1 through 4 were measured for specimen 2A/2B while Strains 1 through 7 were measured for specimen 3A/3B. It should be noted that the strain could not always be recorded for the last load step due to strand slip failure. The failure mode for different specimens is discussed in a later section.

The 305 mm (1 ft.) long specimens (1A and 1B): As shown in Figure 3.5 (a), the ultimate pull-out forces for these two specimen was very close, with the average of both being 153 kN (34.4 kips); the free end slip for both was 6.553 mm (0.258 in.) and 3.632 mm (0.143 in.), respectively. The free end slip started when the pull-out force was

approximately 10 kN (2.2 kips). Both the pull-out force and the slip gradually increased until failure of the specimens occurred. The relationship between the force and the free end slip was parabolic, while the jacking end slip increased linearly with the load. As shown in Figure 3.6 (a) and (b), the concrete surface strain 1 linearly increased with the load. The strain was approximately 150 microstrain when the load reached 150 kN (33.7 kips).

The 610 mm (2 ft.) long specimens (2A and 2B): As shown in Figure 3.5 (b), free end slip occurred in these specimens when the pull-out force was approximately 30 kN (6.7 kips), indicating that the adhesion force between the strand and the concrete was lost at this loading. Adhesion between the strand and concrete caused the initial slope of the curves to be extremely steep. The maximum pull-out force of the strand was 263 kN (59.1 kips), while the ultimate force for the last loading was 227 kN (51.0 kips) with a corresponding free end slip of about 25 mm (0.984 in.). The load versus free end slip curve shows two stages of slip development; the free end slip increased linearly before the load reaches approximately 200 kN (45.0 kips) with a slip approximately 2 mm (0.079 in.). The loading then increased slowly and dropped suddenly at various intervals. For specimen 2A, the recorded first pull-out force drop occurred when the load reached 213 kN (47.9 kips), and the corresponding free end slip was 7.2 mm (0.283 in.); for specimen 2B, the recorded first pull-out force drop occurred when the load reached 232 kN (52.2 kips) and the corresponding free end slip was 8.5 mm (0.335 kips). A force drop then occurred when the test was temporarily suspended to manually record the concrete surface strain. If the strand had been pulled continuously instead of by step-by-step loading, a force drop would not likely have occurred. During the stage of the force drop,

there was increase in the free end slip and the jacking end slip, indicating the development of the stand slip along the entire specimen. It was apparent that the extent of force drop at the early time was smaller. For Specimen 2A, there were two distinct force drops, both of which drop back to 227 kN (51.0 kips) three minutes after the previous load; for specimen 2B, the ultimate force also dropped to 227 kN (51.0 kips). The pull-out tests were discontinued, and the repeated force drops was regarded was deemed a strand slip failure. It was observed that as the force drop occurred an accompanying strand rotation occurred as well. The free end strand began to rotate when the pull-out force reached approximately 200 kN (45.0 kips). With the increase in the force, the strand continued to rotate. The ultimate free end rotation for specimens 2A and 2B was about 9.5 degrees and 7 degrees, respectively. The deviation was measured between the strand centerline and the LVDT string, and the rotation angle was calculated. It should be noted that the measured rotation angle was not very accurate.

In Figure 3.6 (c) and (d), the measured concrete surface strains at four locations along the specimen are plotted. The strain 1 (jacking end) occurred earlier than the others, then strain 2, strain 3, and finally strain 4, indicating that the pull-out force was gradually transferred to the strand from the jacking end to the free end. At low loads, the concrete surface strains slowly increased linearly with the load. When the load approached the maximum, the strains began to drastically increase. Two reasons contributed to this phenomenon. One is that the larger pull-out force results in a significant concrete strain increase. The second reason is that time is required for the pull-out force to be transferred to the strand and then to the surrounding concrete. Although there was a 3 minute pause between loading steps, it seems that this waiting time was not long enough to allow the

force to fully transfer to the concrete. A similar phenomenon occurred for the stress transfer after the release of the prestressing strand, verifying that the concrete surface stress within the transfer length develops with time (Song et al. 2013).

The 915 mm (3 ft.) long specimens (3A and 3B): As shown in Figure 3.5 (c), when the pull-out force reached 60 kN (13.5 kips), free end slip occurred, and the adhesion along the entire specimen was lost. The maximum pull-out force was approximately 350 kN (78.7 kips), which was the strand breaking strength. The ultimate free end slip for specimen 3A was 1.6 mm (0.063 in.), and the slip for specimen 3B was 3.6 mm (0.142 in.). The curve of free end slip at the beginning was very steep. This was followed by a distinct plateau for the jacking end slip curve when the pull-out force approached the yield strength 318 kN (71.5 kips) and plastic tension behavior occurred within the strand. On the other hand, the plateau for the free end slip curve is very short, and was test was terminated when the strand broke at the chuck. A force drop also occurred for the longer specimens. When the force was increased to 226 kN (50.8 kips), the force dropped 5 kN (1.1 kips) which is only 2% of the pull-out force. It was noted that the strand rotation was not detected for this longer specimen. Also, the strand break force was less than the strand breaking strength measured in the previous strand tension tests, although these strands are from the same spool, indicating that the pull-out force may have reached the stand breaking force before the strand break failure in the pull-out tests. This phenomenon may be attributed to the boundary condition change caused by the local behavior at the chuck. In Figure 3.6 (e) and (f), the measured concrete surface strains at seven locations along the specimen are plotted. The strain 1 (jacking end) developed

earlier than other strains, then strain 2, strain 3, through strain 7. The curves for different strain locations are almost parallel.

Figure 3.5 Pull-out force versus strand slip at two ends for non-pretensioned specimens; 1 mm = 0.039 in.; 1 kN = 0.225 kips

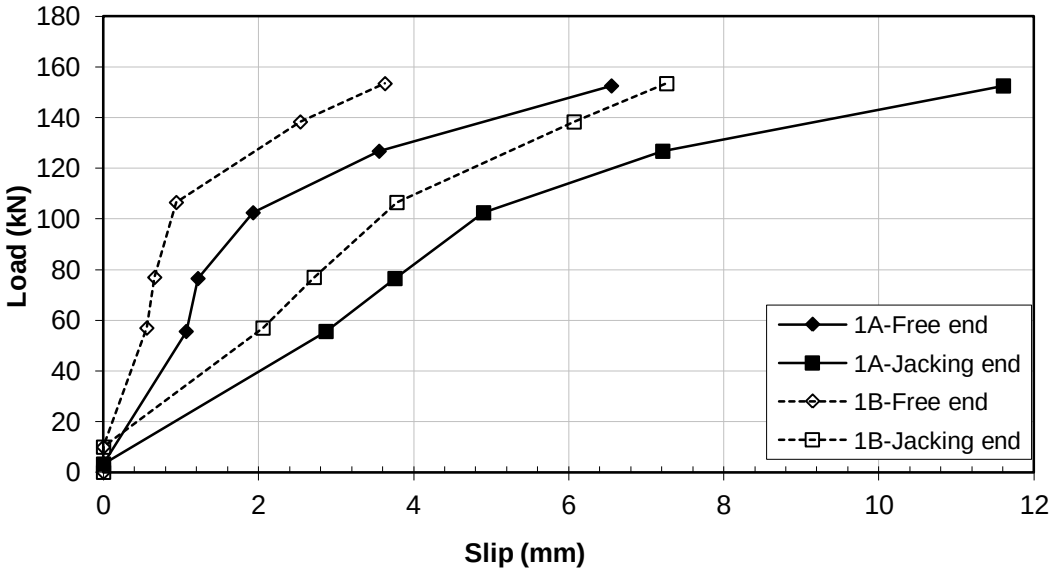

(a) 305-mm (1-ft.) Specimens

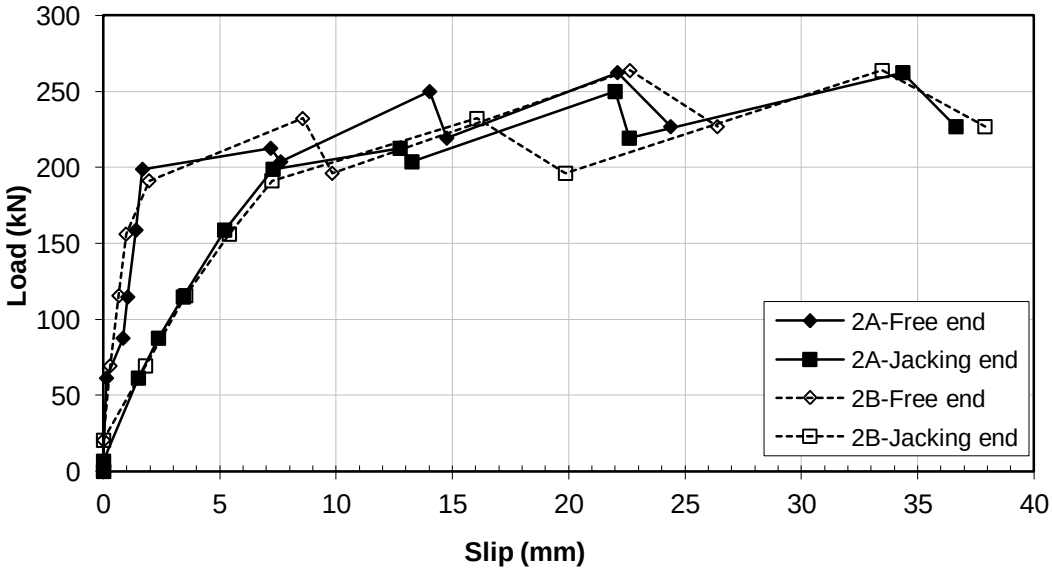

(b) 610-mm (2-ft.) Specimens

Figure 3.5 continued

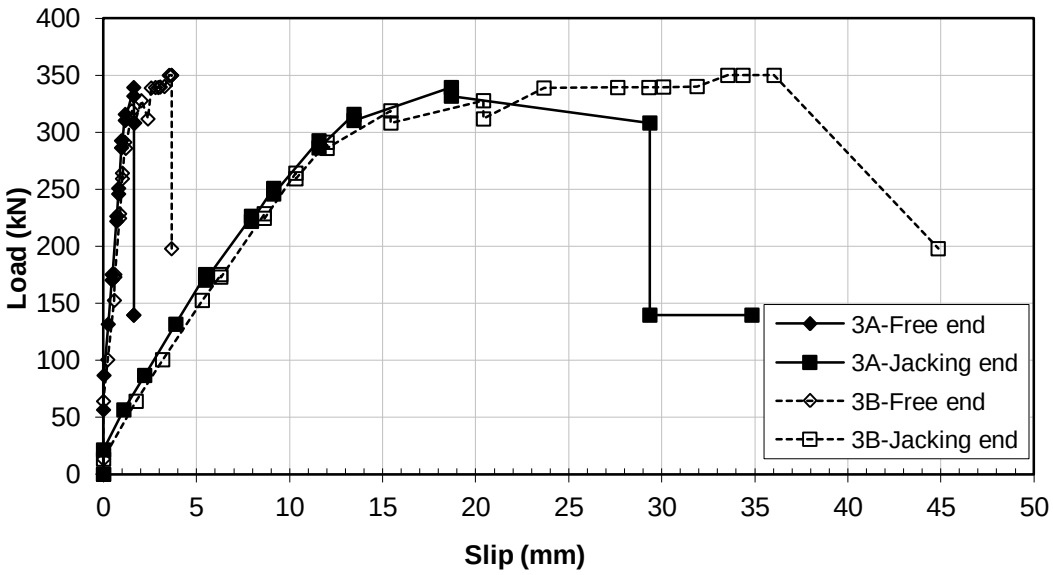

(c) 915-mm (3-ft.) Specimens

Figure 3.5 continued

Figure 3.6 Development of concrete surface strain for non-pretensioned specimens;

1 kN = 0.225 kips

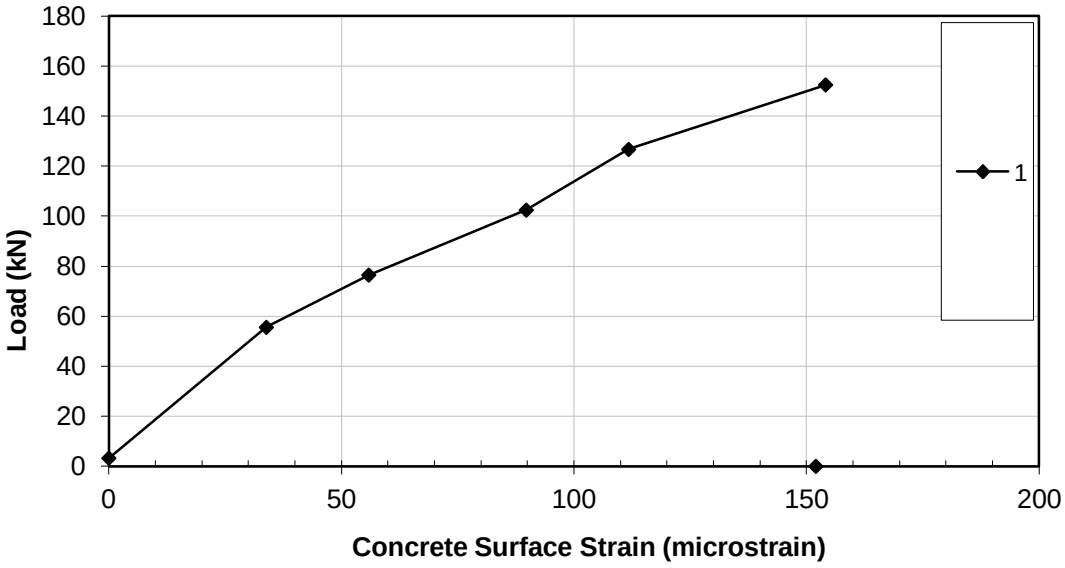

(a) Specimen 1A

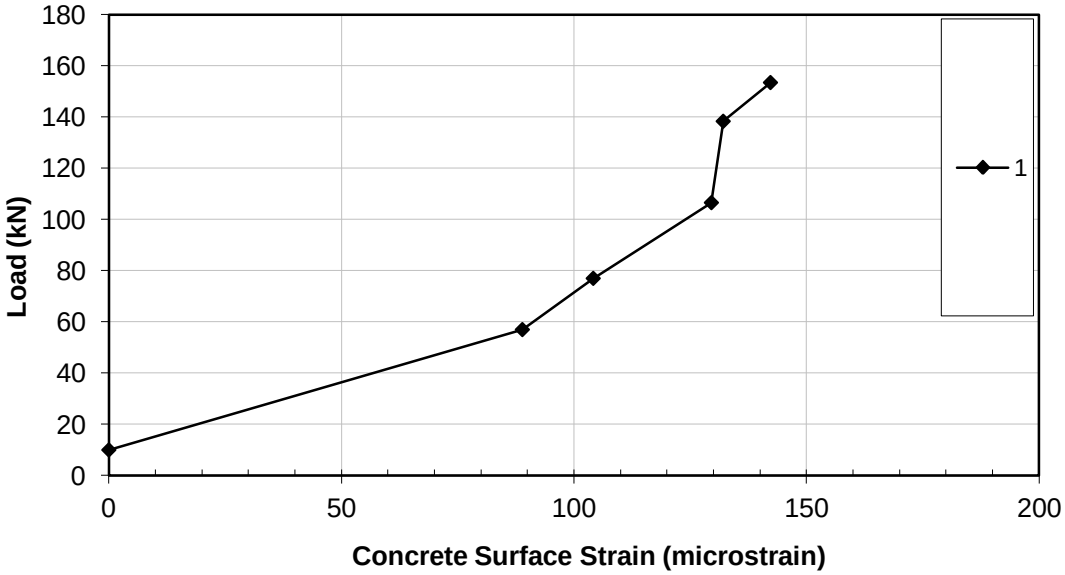

(b) Specimen 1B

Figure 3.6 continued

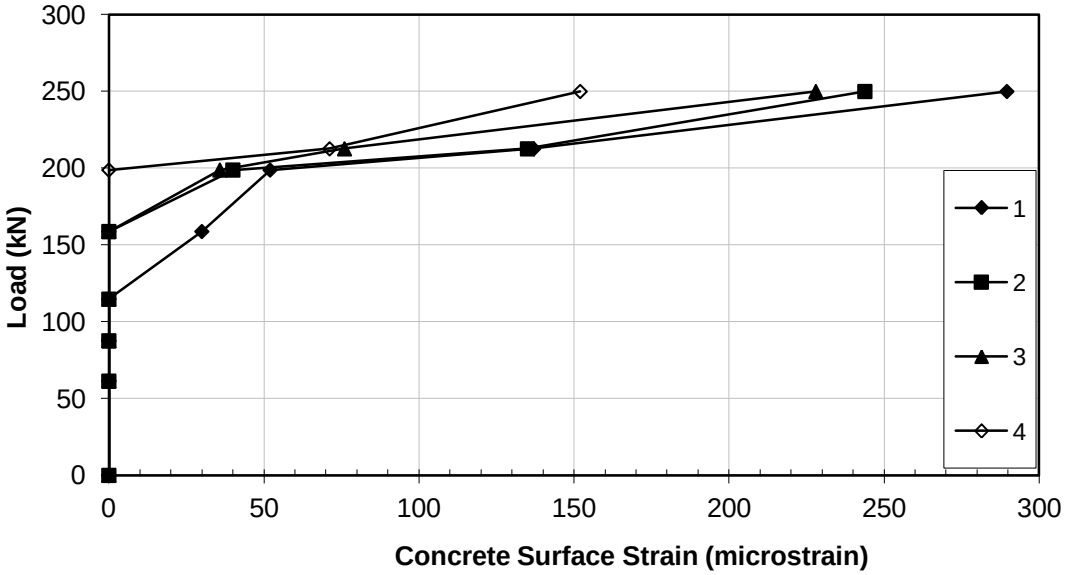

(c) Specimen 2A

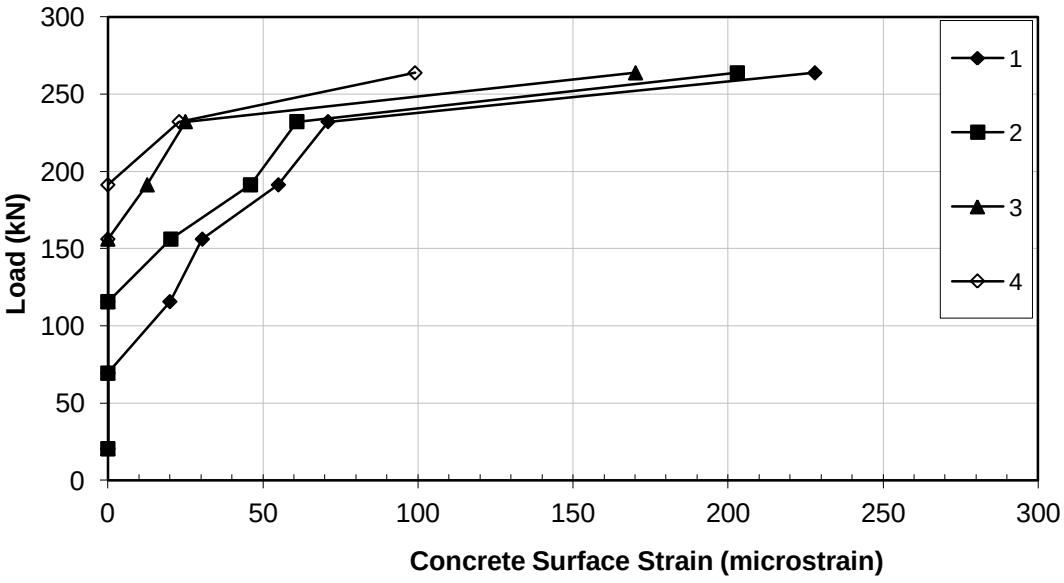

(d)

(d) Specimen 2B

Figure 3.6 continued

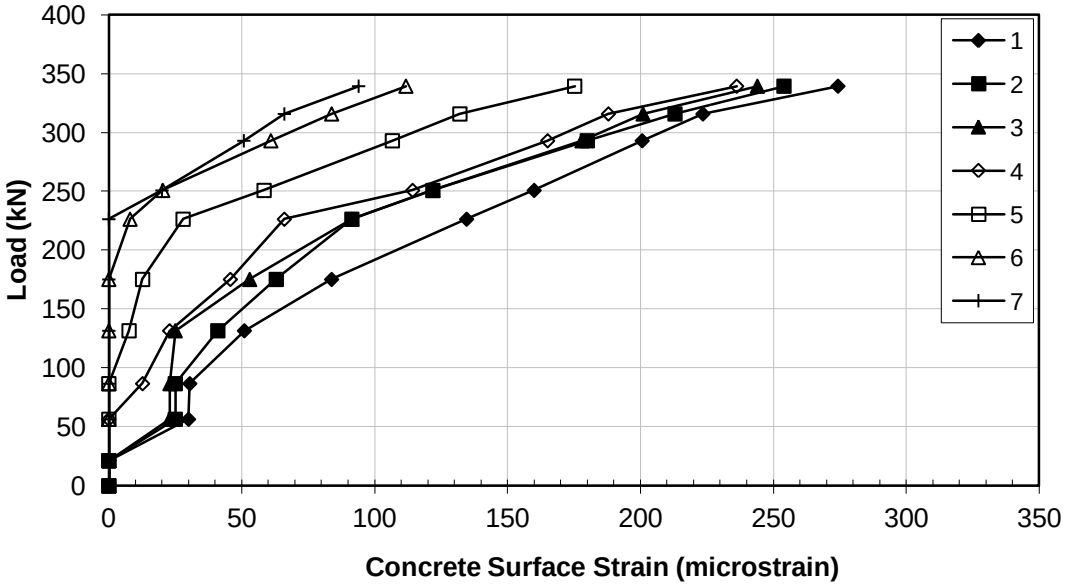

(e) Specimen 3A

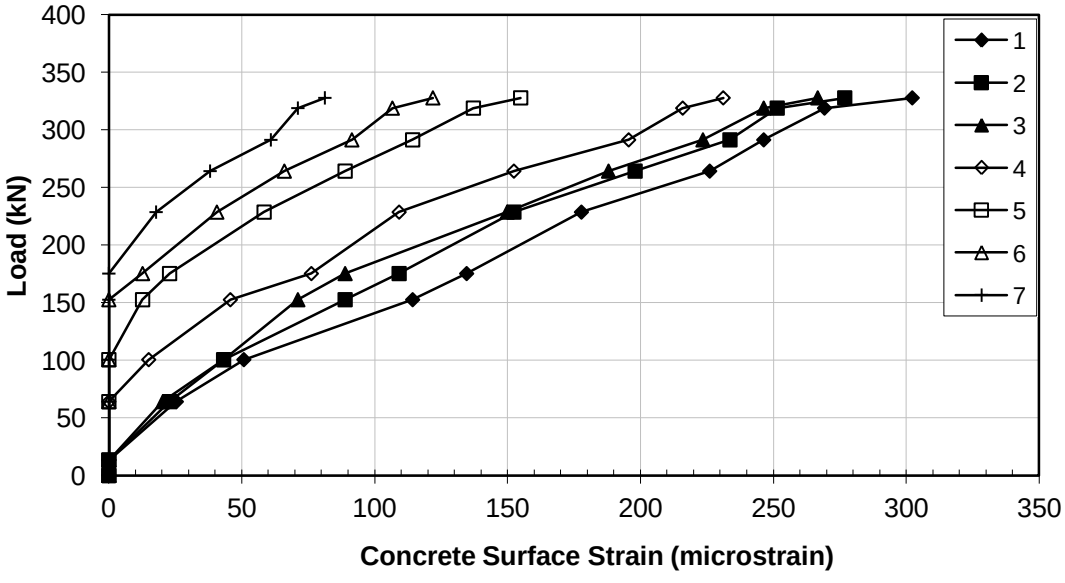

(f) Specimen 3B

Figure 3.6 continued

3.8 Test Results Analysis and Comparison

***Failure mode*:** For specimens with different lengths, the failure modes were totally different. The failure of specimens 1A, 1B, 3A, and 3B was very brittle and sudden, while the failure of specimens 2A and 2B was ductile. For specimens 1A and 1B with length 0.5 Lt, the free end slip gradually increased with the pull-out force until a sudden concrete splitting failure occurred. As shown in Figure 3.7 (a), a splitting crack located along the entire specimen at the centerline of the specimen occurred separating the specimen into two parts. Some grout powder was observed at the splitting interface between the strand and the concrete. Also, distinct abrasion marks were detected at the concrete/strand interface, indicating that the sudden slip severely damaged the interface which resulted in the development of splitting cracks across the cross section.

For specimens 2A and 2B, the failure mode was strand slip and rotation, as shown in Figure 3.7(b). After the pull-out force exceeded 200 kN (45.0 kips), the free end slip drastically increased while the force fluctuated. Finally, the tape used for the LVDT hook in the free end is close to the specimen free end. Accompanying the significant slip was distinct strand rotation, which was observed from the angle between the strand and the LVDT string.

For specimens 3A and 3B, the failure mode was the strand break at the chuck on the jacking side (the strand dent is caused by the constraint of the chuck), as shown in Figure 3.7 (c). The fracture plane for each wires of the strand was approximately 45 degree to the twist direction. At the beginning of the strand break, only one or some wires broke, and then the whole strand broke as the jack continued to induce elongation.

(a) Concrete splitting Failure for 0.5 Lt Specimens

(e)

(b) Strand slip and rotation Failure for 1.0 Lt Specimens

(f)

(c) Strand break at the Chuck Failure for 1.5 Lt Specimens

Figure 3.7 Failure modes for specimens with different strand embedment length

The relationship between the pull-out force and the free end slip: For the 305, 610 and 915 mm (1, 2 and 3 ft.) long specimens, the maximum pull-out force were 153, 263 and 350 kN (34.4, 59.1 and 78.7 kips), respectively. If we assume the bond stress is uniformly distributed along the specimen, the average pull-out force per unit length for these

specimens would be 0.50, 0.43 and 0.39 kN/mm (2.86 , 2.46 and 2.18 kips/in.), individually. This indicates that the shorter specimen has a higher bond stress to resist the pull-out force, or the shorter specimen has a greater bond capacity per unit length in comparison with the longer specimen. The ultimate free end slip of the 305 mm (1 ft.) long specimens and the 915 mm (3 ft.) long specimens were significantly smaller than that of the 610 mm (2 ft.) long specimens. As shown in Figure 3.8 (a), the initial slope of the curves for the longer specimen was significantly greater than that of the shorter specimen. For the 305, 610 and 915 mm (1, 2 and 3 ft.) long specimens (i.e. 0.5 Lt, 1.0 Lt, 1.5 Lt specimens), the average ratio of the pull-out force to the free end slip in the initial stage was 90, 140 and 270 kN/mm (513.91, 799.42 and 1541.74 kips/in.). The ratio for the 1.5 Lt specimens was almost twice of the ratio for the 1.0 Lt specimens, and is triple of the 0.5 Lt specimens. The typical relationship between the pull-out force and the free end slip is plotted in Figure 3.8 (b). For the 0.5 Lt specimens, the curve is parabolic until a sudden concrete splitting. For the 1.0 Lt specimens, the free end slip initially linearly increases with the pull-out force, and then the curve reaches a plateau where the slip continuously increases while the pull-out force fluctuates. For the 1.5 Lt specimens, the free end slip initially slowly linearly increases with the force, then the slip increases faster, finally the strand breaks. Because of the adhesion force, the required pull-out force is larger for the longer specimens to cause the initial free end slip. The loss of chemical adhesion will be compensated by friction and mechanical interlock. The pull-out forces activating the free end strand slip for the 305, 610 and 915 mm (1, 2 and 3 ft.) long specimens approximate to 10, 30, and 60 kN (2.25, 6.74 and 13.49 kips), respectively.

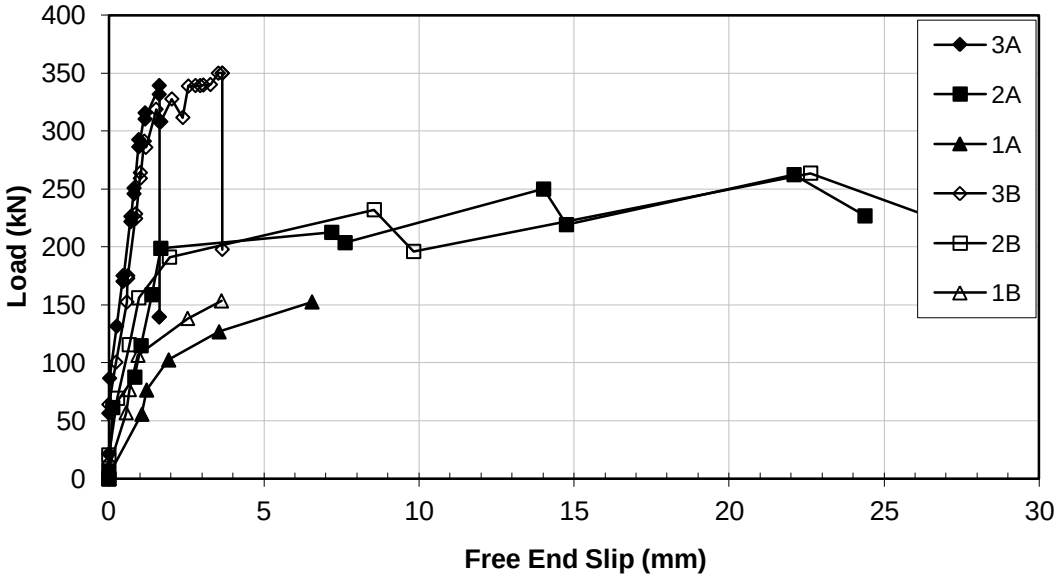

(a) Measured Curves for Specimens

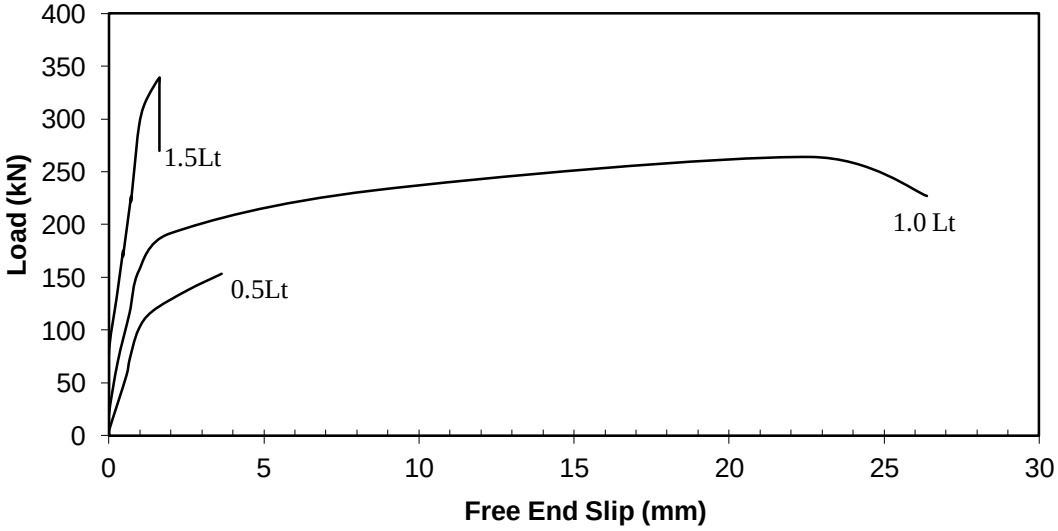

(b) Typical Curves

Figure 3.8 Pull-out force versus free end slip; 1 mm = 0.039 in.; 1 kN = 0.225 kips

Concrete strain distribution: The development of the concrete surface strains at different locations under loading is presented in Figure 3.6. We observed that the development of the concrete surface strain for the specimens of the same length is similar. For the purpose of comparison, the concrete strain distribution measured at the pull-out force close to the failure (the last measured strain for each pull-out test) was investigated. In Figure 3.9 (a) and (b), the legend includes two parts: the first part is the specimen ID, and the second part is the value of the pull-out force. It is shown that the concrete surface strain along the specimen approximately linearly decreases from the jacking end to the free end. Figure 3.9 (a) shows that the position of the curves for the longer specimen is higher due to the larger pull-out force. Figure 3.9 (b) shows the concrete surface strain distribution when the pull-out force is close to 250 kN (56.2 kips), indicating the position of the curves for the longer specimen is lower because the pull-out force is transferred to concrete within a longer length.

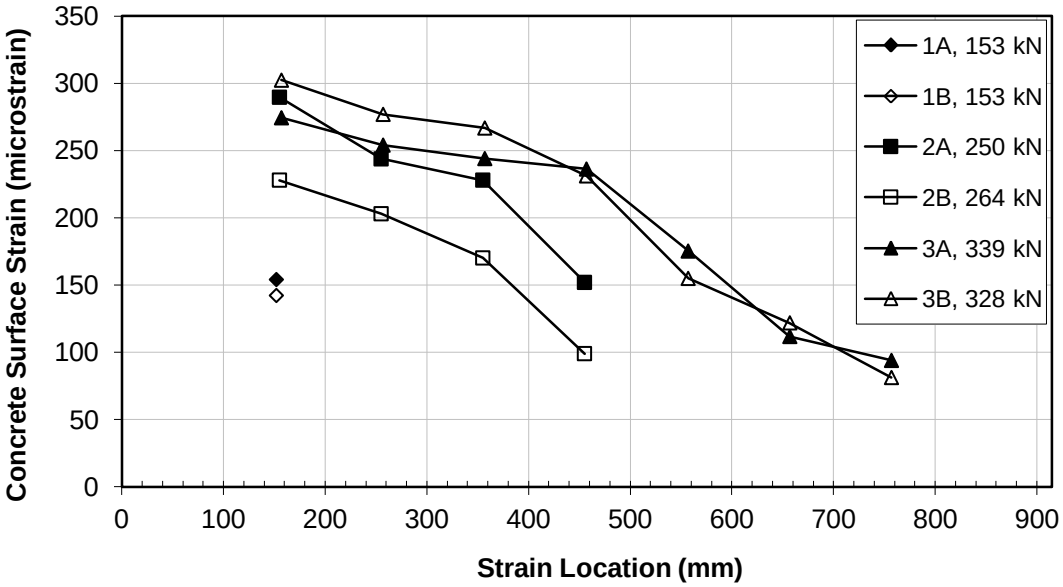

(a) Last Measured Concrete Surface Strain

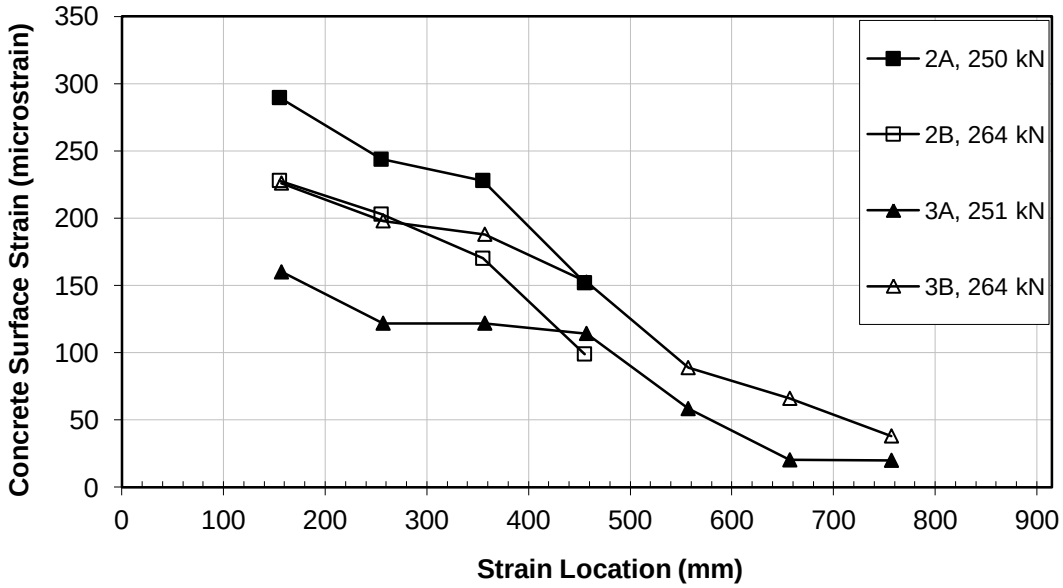

(b) Concrete Surface Strain at a Specific Load

Figure 3.9 Comparison of the selected measured concrete surface strain distribution; 1 mm = 0.039 in.; 1 kN = 0.225 kips

3.9 Conclusions and Discussion

The bond behavior of 18-mm-(0.7-in.-) diameter strands was studied through six non-pretensioned pull-out tests of specimens with different strand embedment lengths (0.5 Lt, 1.0 Lt and 1.5 Lt,). The effect of strand embedment length on the bond behavior was addressed. The relationship between the pull-out force and the slip, the concrete surface strain distribution and development, and the specimen failure modes were investigated. Based on the present study, the conclusions can be drawn as follows:

1. The specimens with different strand embedment length have different failure modes. For the 0.5 Lt specimens, the failure mode was brittle concrete splitting along the entire specimen. For the 1.0 Lt specimens, the failure mode was the significant strand slip accompanied with strand rotation; the ultimate pull-out force fluctuates while strand keeps slipping. For the 1.5 Lt specimens, the failure mode is the sudden break of strand at the chuck.

2. The relationship between the pull-out force and the free end slip is different for the specimens with different length. For the 0.5 Lt specimen, the curve is parabolic until a sudden concrete splitting. For the 1.0 Lt specimen, the free end slip initially linearly increases with the pull-out force, and then the curve reaches a plateau where the slip continuously increases while the pull-out force fluctuates. For the 1.5 Lt specimen, the free end slip initially slowly linearly increases with the force, then the slip increases faster than before, and finally the strand breaks. The ultimate free end slips for the 0.5 Lt and 1.5 Lt specimens are very small due to their brittle failure.

3. Although the maximum pull-out force for the longer specimen is larger, the shorter specimen has a greater bond capacity per unit length. For the 305, 610 and 915 mm (1, 2

and 3 ft.) long specimens, the maximum pull-out forces (bond capacity) are 153, 263 and 350 kN (34.4, 59.1 and 78.7 kips), respectively; the average pull-out forces per unit length for these specimens are 0.50, 0.43 and 0.39 kN/mm (2.86 , 2.46 and 2.18 kips/in.), respectively.

4. The initial slope of the force-free end slip curves of the longer specimen is significantly greater than that of the shorter specimen. The slope for the 1.5 Lt specimen is almost twice of the ratio for the 1.0 Lt specimen, and is triple of the 0.5 Lt specimen.

5. Except for the 0.5Lt specimen, pull-out force drop occurs during the pause of the jack elongation when the force exceeds a certain level. However, the extent of the force drop for the 1.0 Lt specimen is more distinct than that for the 1.5 Lt specimen. Furthermore, the strand rotation is accompanied with the force drop for the 1.0 Lt specimen while no apparent strand rotation is detected for the 1.5 Lt specimen.

6. The adhesion between strand and concrete was studied. Initially, the pull-out force results in the loss of the adhesion to activate the free end slip. Once the slip occurs, the loss of chemical adhesion will be compensated by friction and mechanical interlock. The required force to cause the initial free end slip is larger for the longer specimen. The pull-out forces activating the free end strand slip for 305 mm, 610 mm and 915 mm (1, 2 and 3 ft.) specimens are approximately 10, 30, and 60 kN (2.25, 6.74 and 13.49 kips), respectively.

7. The concrete surface strain linearly increases with the pull-out force. The distribution of the strains along the entire specimen is approximately linear.

Through the analysis of the pull-out test results, it revealed that the bond behavior was dependent on strand embedment length. The previous pull-out studies have not

considered this factor; however, it is suggested that the three different strand embedment lengths (0.5 Lt, 1.0 Lt, and 1.5 Lt) be considered as standard to evaluate the bond behavior for the strand. Also, the relationship between the strand embedment length and the bond capacity can be directly used as design guideline. When the 18-mm-(0.7-in.-) diameter strand is used in prestressed concrete girders, it is suggested that 1.5 Lt should be used as the minimum embedment length to avoid anchorage failure. The transfer length could be analyzed from the failure mode of the pull-out test, because the failure mode shall be strand break once the strand embedment length is longer than the transfer length and the failure mode shall be strand slip when the embedment length is close to the transfer length. This provides a new thinking way to determine the transfer length.

Finally, this pull-out testing revealed that the bond was a time-dependent process. Although we waited about 3 minutes and then measured the concrete surface strain at the end of the each loading step, it seemed that the time was not enough long to allow the pull-out force to fully transfer from the strand to the concrete. No distinct concrete surface strain was detected during the first several loading steps. The occurrence of force drop indicated the development of strand slip from the jacking end to the free end.

Chapter 4 : Bond Mechanism and Pull-out Tests of Pretensioned Specimens

4.1 Introduction

Bond refers to the interaction and transfer of force between steel strands and concrete. Without the bond, the pretensioned concrete members would not be possible. For the pretensioned concrete members, the anchorage and development of prestressing force exclusively depend on the bond since the release of strands. The bond in pretensioned concrete members may be categorized as the transfer bond and the flexural bond. The former exists at the release of the prestressing strand through the transfer of the prestress force from the strand to the concrete in the end zone. The latter starts acting when the external loads is applied and causes the increase of the strand stress and concrete cracking. In essence, bond controls the behavior of the pretensioned concrete members; the effect of bond is of great interest.

Extensive research on the transfer bond and flexural bond has been conducted parametrically. There are a number of variables affecting the bond: strand diameter, strand location and spacing, strand release method, strand surface condition, concrete strength, concrete cracking, concrete age, curing condition and so on. Janney (1954) tested the prestressed concrete prisms to determine the distribution of prestress transfer bond when the strand was released. Also, the short beam specimens were three-point-loaded to failure to investigate the flexural bond. The effect of the diameter and surface condition of the steel wire, and concrete strength was studied. Hanson and Kaar (1959) conducted an investigation of flexural bond in 47 beams pretensioned with seven wire strands. The effect of the embedment length and diameter of strand on the bond performance was studied. Stocker and Sozen (1970) conducted 486 tests of simple pull-

out specimens with short embedment lengths. The basic information on the relationship between bond and slip was provided. A number of variables were investigated: size of strand, concrete, lateral confining pressure and time effect. A hypothesis on the nature of bond for plain wire and strand was developed, and a simple conceptual model was proposed to explain the bond characteristics. Abrishami and Mitchell (1993) studied the bond characteristics of pretensioned strand along the transfer length and the development length. The average bond stress was directly obtained from measured forced in the strand rather than the strains measured on the strands or concrete surface.

However, the understanding of the nature of bond is still incomplete because the sources of bond are microscopic in nature. Bond originates from the chemical adhesion, friction and mechanical interlock between the strand and concrete. A rational understanding of the bond mechanism would help reduce the amount of required testing and develop the guideline for the design of pretensioned concrete members. General concept of bond was discussed by the previous research (Leonhardt, 1964; Stocker and Sozen, 1970; Russell and Burns, 1993). Very little effort has been made to quantify the elements of bond mechanism. Due to the rigid brittle behavior of the adhesion bond, it disappears as soon as the relative slip occurs between the strand and the surrounding concrete. The slip within the concrete members cannot be directly detected or measured, causing the difficulty in quantifying its contribution. This component is ignored in most cases. Friction, a recognized main component of bond, is of large variability and unpredictability. According the classic Column friction theory, there are two main factors for the friction: normal pressure and friction coefficient. The normal pressure is hard to obtain at the interface, and its distribution along the strand and around the strand is

complicated. Furthermore, the friction coefficient is dependent of the surface condition of the strands, causing the large variability. Mechanical interlock is attributed to the normal force, friction coefficient between the strand and the concrete, and the pitch angle of the outer wires of the strands. Therefore, it is very difficult to quantify its contribution to the bond although it is traditionally regarded as the largest contributor to the flexural bond.

4.2 Research Significance

The primary objective of the research in this chapter was to investigate the bond behavior of the prestressing 18-mm-(0.7-in.-) diameter strand in high strength concrete through the pull-out tests of specimens with different pretension levels and specimen length (strand embedment length). Firstly, 18-mm-(0.7-in.-) diameter strand is attractive due to its larger strength capacity and concrete with high early strength contributes to accelerated bridge construction. However, the bond of the prestressing strand is unknown. Secondly, it is very important to introduce a standardized feasible and reliable pretensioned pull-out test method. The previous research (Stocker and Sozen, 1970; Bearley and Johnson, 1990) studied the bond behavior through the typical simple pull-out tests of the non-pretensioned concrete members. Some members and participants of PCI's Prestressing Steel Committee even objected that a non-pretensioned pull-out test may not provide the true bond information of pretensioned strand (Logan, 1996). In fact, it is reasonable to believe there is a difference between the non-pretensioned and pretensioned strand because of the Hoyer's effect. Thirdly, both the level of pretension force and the specimen length affect the bond; however, the effect of these two parameters has not been addressed in the previous pull-out tests. Finally, the contribution of each component of the bond mechanisms has never been quantified. By comparison of the results of the

pull-out tests of the non-pretensioned and pretensioned speciemens, the bond mechanism in the end zone of the pretensioned concrete members will be deeply investigated in this chapter. Thus, a reliable pretensioned pull-out test method is proposed in this chapter, to help understand the bond behavior of the pretensioned strand and quantify bond mechanism.

4.3 Bond Mechanism

The resource of the bond between the prestressing strand and concrete includes adhesion, Hoyer's effect and mechanical interlock. Although the friction is not listed as a separate bond mechanism, both Hoyer's effect and mechanical interlock are dependent of the friction (Russell and Burns, 1993). Without friction, the bond stress from Hoyer's effect would be zero and that from mechanical interlock would be reduced.

4.3.1 Adhesion

Adhesion is a chemical mechanism between the concrete and the steel. As shown in Figure 4.1(a), it effectively prevents the relative slip at the interface until a critical stress is reached. The adhesion is easily destroyed once slip has occurred, and the loss of adhesion is immediate. The transfer zone is, in essence, characterized by the strand slip. Since the release of the prestressing force, adhesion would have not contributed to the bond in the transfer zone and can be neglected due to the relative slip.

4.3.2 Hoyer's effect

Hoyer's effect, referred to as "wedge action", was investigated in 1939 (Hoyer and Friedrich 1939). It is active exclusively in the transfer zone in the pretensioned concrete members. This mechanism is shown in Figure 4.1(b). When the steel strand is pretensioned, the tensile force causes a reduction of the strand diameter by Poisson's ratio

as it is elongated. The tensile force is released once the surrounding concrete hardens. Upon the release of the prestressing force, the strand loses its initial prestress and tries to regain the original shape. However, the surrounding concrete prevents the lateral expansion of the strand, causing a radial pressure and activating a high friction at the interface between concrete and strand. This friction resistance opposes relative movement at the interface. It is apparent that the bond stress and the radial pressure due to the Hoyer's effect are larger for the strand close to the free end.

4.3.3 Mechanical interlock

In the seven wire strand, six outside wires wrap a central wire in a helical pattern. As shown in Figure 4.1(c), the "humped" shape of the strand bears against the ridges of the surrounding concrete in the interstices of the strand. When the strand attempts to slip relative to the concrete "envelope", these concrete ridges will resist the displacement of the strand. The concrete stress distribution around the strand is not uniform due to the mechanical interlock. After the initial shear failure of the interlocking concrete ridges, the interface become relatively rough. With further sliding, the concrete surface is abraded and loose wear particles are formed at the interface.

Mechanical interlock is the largest contributor to the flexural bond. It depends on the pitch angle of the outer wires of the strand, the friction coefficient and the normal force at the interface.

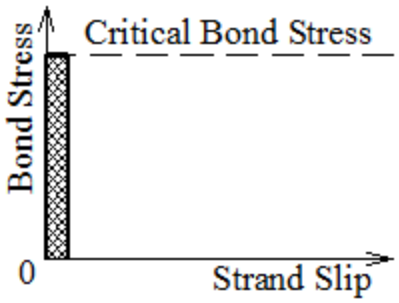

(a) Adhesion

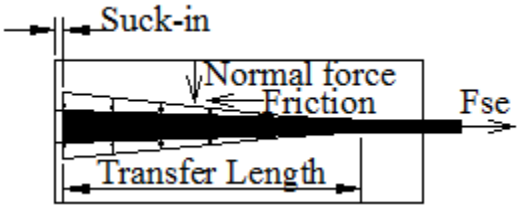

(b) Hoyer's effect

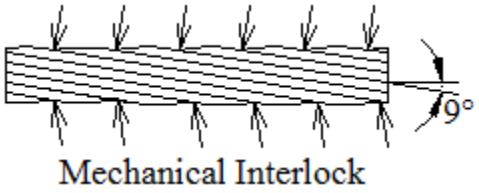

(c) Mechanical interlock

Figure 4.1 Bond mechanisms for pretensioned concrete members

4.4 Idealization of Bond Mechanism in Transfer Zone

Russell and Burns (1993) proposed an idealized bond mechanism in the anchorage end zone. As shown in Figure 4.2, the bond for the transfer of pretensioned force is mainly from Hoyer's effect and mechanical interlock. Janney's test results (Janney, 1954) supported that most of the transfer bond developed due to the Hoyer's effect, because the wires were smooth in his transfer length experiments and thus mechanical interlock could

not contribute to bond. As for the pretensioned strand, the relative contribution of each bond mechanism is unknown, although Russell and Burns (1993) claimed that most of the transfer bond probably was from Hoyer's effect because mechanical interlock had not been fully developed.

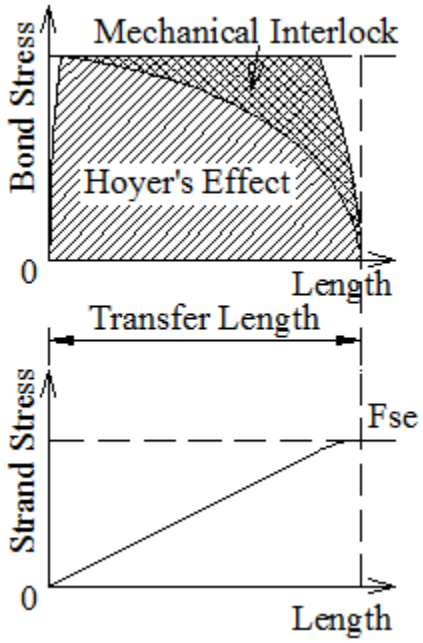

Figure 4.2 Idealization of bond mechanism in transfer zone

4.5 Test Program

One objective was to quantify the contribution of each transfer bond mechanism. Three sets of prisms with different specimen length were cast as shown in Table 4.1. The strand and the concrete were the same as in the non-pretensioned pull-out test addressed in chapter 3. The strand was located at the concrete center through the length of the specimen. The identification code of the specimen includes two parts connected by "-". The first part represents the specimen length or the strand embedment length (unit: ft.).

The second character designates the pretension force (unit: kips). Therefore, an example prism was 1-60, which was the 1 ft (305 mm) specimen with pretension force 60 kips (267 kN). It was noted that there were two non-pretensioned specimens for each set (their test results have been shown in chapter 3); thus, they were named as "X-00A" or "X-00B", in which "X" was specimen length (unit:ft). In chapter 3, these non-pretensioned specimens were named as "XA" or "XB".

As mentioned, the main objective was to investigate the bond property of the pretensioned specimens. Three pretension levels were considered: 20, 40 and 60 kips (89, 178 and 267 kN). The specimens were cast and stored in the same environment as the non-pretensioned specimens. The prisms were stripped and the pretensioned strand was cut with the electrical saw 24 hours after concrete cast. The pullout test was conducted two days after the concrete cast. In this way, the age of concrete on the pull-out test day was 2 days, which was the same for the non-pretensioned strand pull-out test. Therefore, the only difference of the pretenioned specimens in this chapter and the non-pretensioned specimens in chapter 3 was the consideration of the pretension force which causing one Hoyer's effect within the transfer zone. Through the comparison of the pull-out test for both non-pretensioned and pretensioned specimens, the bond mechanism could be quantitatively investigated. In addition, with consideration of different specimen length and pretension force, the relationship between the transfer length and the pretension force level will be studied.

Table 4.1 Summary of tests

Specimen ID	Length (mm)	Pretension force (kN)	Effective pretension force (kN)	suck-in before pull-out (mm)	Pull-out force activating free end strand slip(kN)	Maximum pull-out force (kN)	Maximum free end slip (mm)	Measured maximum concrete surface strain (μ)	Force drop	Strand rotation	Failure mode
1-00A	305	0	0	0	6	153	6.6	154	No	No	Concrete split
1-00B	305	0	0	0	10	153	3.6	142	No	No	Concrete split
1-20	305	89	62	1.9	85	181	50.3	219	Yes	Yes	Strand slip
1-40	305	178	32	2.3	80	187	49.7	244	Yes	Yes	Strand slip
1-60	305	267	61	3.0	80	190	99.8	218	Yes	Yes	Strand slip
2-00A	610	0	0	0	30	262	24.4	290	Yes	Yes	Strand slip
2-00B	610	0	0	0	25	264	26.4	228	Yes	Yes	Strand slip
2-20	610	89	13	0.5	110	321	89.6	330	Yes	No	Strand slip
2-40	610	178	159	0.9	222	331	21.7	455	Yes	No	Strand slip
2-60	610	267	236	1.9	268	329	14.3	465	Yes	No	Strand slip
3-00A	915	0	0	0	57	339	1.6	274	Yes	No	Strand break
3-00B	915	0	0	0	64	350	3.3	302	Yes	No	Strand break
3-20	915	89	72	1.2	96	323	2.4	467	No	No	Strand break
3-40	915	178	130	1.6	202	367	2.5	442	No	No	Strand break
3-60	915	267	217	2.2	240	374	1.5	483	No	No	Strand break

1 mm = 0.039 in.; 1 kN = 0.225 kips

As shown in Figure 4.3, an II-shape horizontal steel frame using HHS$7 \times 7 \times 3/8$ were anchored to the ground using bolts. Two chucks (Chuck A and B) were used in both ends of the strand. Through the elongation of the jack cylinder, the strand was pretensioned. The Load Cell against the Chuck A provided the value of the pretension force. The concrete specimen was cast using steel forms. One day after the concrete cast, the pretensioned strand was cut at the right cut point. The stand in the right free end lost the initial prestress and swelled, resulting in a Hoyer's effect. The suck-in in the free end at transfer can be measured with caliper; the pretension force drop was recorded by the load cell. In the pullout test, the pullout force was caused by the jack cylinder. The load cell behind the Chuck A recorded the pullout force; LVDT A and B recorded the slip of strand in the jacking end and the free end. During the process of the pull-out test, the concrete surface strain along the specimen can be recorded using DEMEC strain gauge system. The layout of the strain points was the same as that for the non-pretesnsioned specimens. The concrete surface strain was measured twice before the start of the pull-out test: just at the release of the pretension force and just before the pull-out test (one day after the strand cutting). During the step-loaded pull-out test, the pull-out force was manually controlled by the elongation of the cylinder, and the concrete surface strain was measured 3 minutes after pause of cylinder elongation.

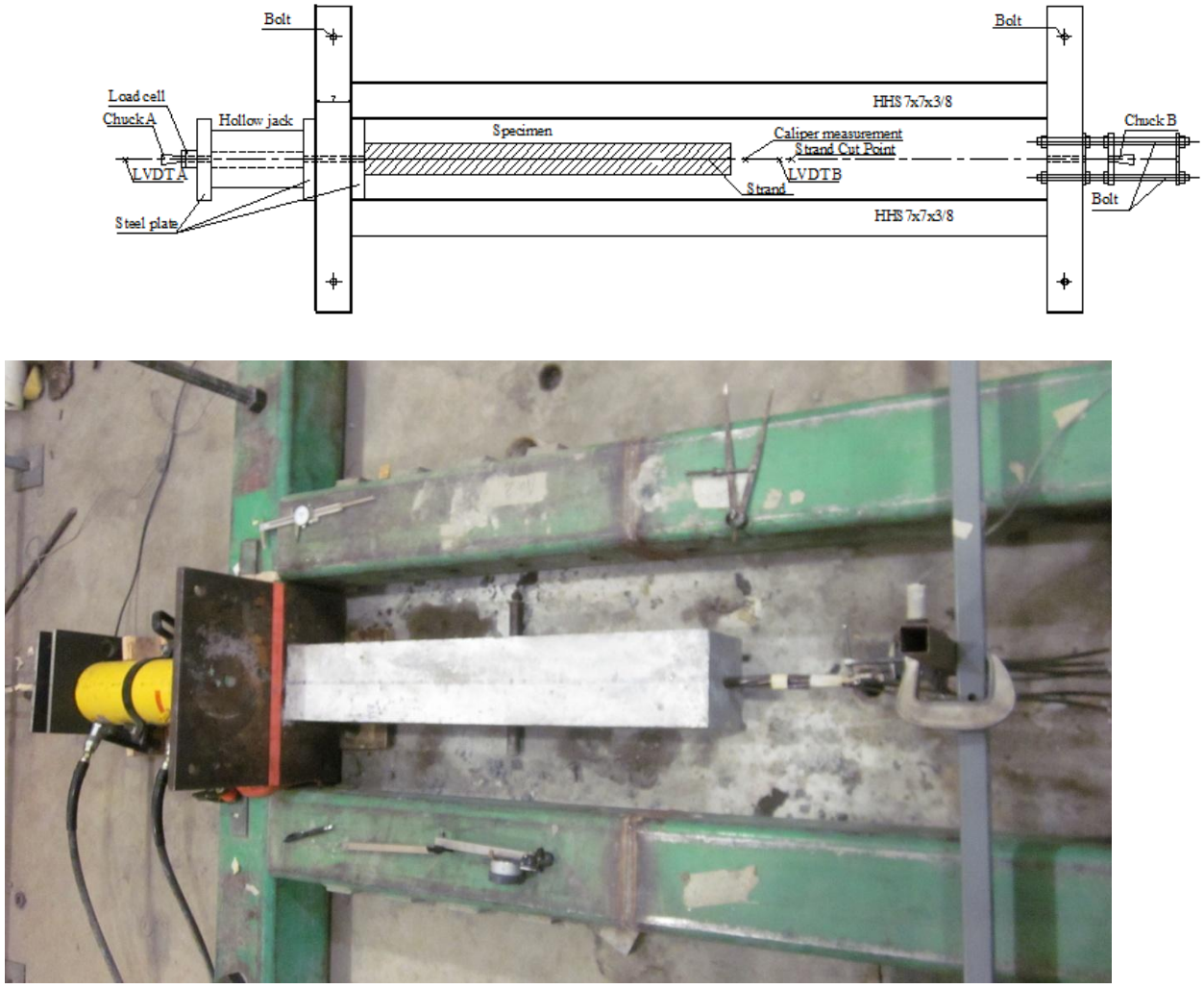

Figure 4.3 Pull-out test setup for pretenisoned specimens

4.6 Test Results for each Specimen

The pull-out loads vs. free end slip and jacking end slip are shown in Figure 4.4 (a) through Figure 4.4 (i). Due to the significant difference of both the slip and the pull-out force among different specimens, the scale was only the same for the specimens with the same length. The jacking end slip keeps increase since the pull-out force was caused by the elongation of the jack cylinder. In contrast, the free end remains at zero until the pull-out force increases to the extent that causes the strand slip along the entire specimen. The

relationship between the pull-out force and the concrete surface strains at different locations is shown in Figure 4.5(a) through Figure 4.5(i). The number in the legend represents the strain point, and the location of the strain points is shown in Figure 3.3.

The 305 mm (1 ft.) long specimens (1-20, 1-40 and 1-60): Generally, the pretension level was 75% of the strand ultimate strength. For the 18-mm-(0.7-in.-) diameter strand, 75% of the strand ultimate strength was 267 kN (60 kips). For the specimen 1-20, 1-40 and 1-60, their pretension force was 89, 178 and 267 kN (20, 40 and 60 kips), respectively; and their effective pretension force after strand release was 62, 32 and 61 kN (13.9, 7.2 and 13.7 kips), respectively. Although the pretension levels were significantly different, the effective pretension forces were very close. It indicates that the 305 mm (12 in.) long specimen has a bond capacity limit to effectively transfer the pretension force to the concrete. The transfer length was related to the pretension level. When the pretension force was larger than 178 kN (40 kips), the transfer length for the 18-mm-diatmeter strand was longer than 305 mm (12 in.). This was validated by our previous findings that the transfer length of the 18-mm-(0.7-in.-) diameter strand approximates to 610 mm (24 in.) when the pretension force was 267 kN or 60 kips (Ma and Burdette, 2011).

Force drop (described in chapter3) during the pull-out process was detected when the pull-out force reaches a certain level. The force drop extent for the specimen 1-60 was more apparent than that for specimen 1-40 and 1-20. For all pretensioned 305 mm (12 in.) specimens, the strand in the free end starts to rotate when the pull-out force approximates to 170 kN (38.2 kips). However, neither force drop nor strand rotation was detected for the non-pretensioned specimen 1-00A and 1-00B. The ultimate pull-out force for the non-

pretensioned specimen was about 150 kN (33.7 kips) while force drop in the pretensioned pull-out force appears when the pull-out force approximate to 150 kN (33.7 kips). For all pretensioned 305 mm (12 in.) specimens, the strand in the free end does not slip at the beginning of the pull-out force. Instead, the free end strand slip starts when the pull-out force increases from the initial effective strand force to 80 kN (18.0 kips) which was close to the pretension level for specimen 1-20. For the non-pretensioned specimens, the adhesion contributes little to the bond and it can be neglected; the free end slip occurs once the pull-out force damage the chemical adhesion along the entire specimen. For the pretensioned specimens, adhesion has already disappeared upon the release of the strand; this initial steep load-slip curve was attributed to the Hoyer's effect, and the free end slip was activated because the tension in strand reduces the steel area and the radial pressure on concrete, causing the damage of the Hoyer's effect.

As shown in Figure 4.5(a) through (c), the concrete surface strain developes with time and increasing pull-out force. The load-strain curve was composed of two stages. In stage I (transfer stage), which was from the strand cut to the start of pull-out, the strain continuously increases while the effective pretension force in the jacking end strand decreases with time. In stage II (pull-out stage), which was the pull-out process, the concrete surface strain developes with the increasing pull-out force. For all 305 mm (12 in.) pretensioned specimens, the ultimate pull-out force and the ultimate strain were very close despite of the different pretension level, indicating the bond capacity limit for this short specimen.

The 610 mm (2 ft.) long specimens (2-20, 2-40 and 2-60): Apparent force drop occurs for all three specimens, and this phenomenon was more notable for the specimen with

higher pretension level. By comparison with the 305 mm (12 in.) specimens of the same pretension force, the extent of force drop was larger. However, unlike the pretensioned 305 mm (12 in.) specimens, no stand rotation was detected. For the specimen 2-20, 2-40 and 2-60, the effective pretension force after strand release was 13, 159 and 236 kN (2.9, 35.7 and 53.1 kips). Unlike the pretensioned 305 mm (12 in.) specimens, higher pretension level causes larger effective pretension force in the strand for the 610 mm (24 in.) pretensioned specimens, and the effective pretension force does not decrease with time. For the specimen 2-20, 2-40 and 2-60, due to the Hoyer's effect, the free end strand starts to move into the concrete until the pull-out force increases from the initial effective pretension force to 110, 222 and 268 kN (24.7, 49.8 and 60.2 kips), respectively.

As shown in Figure 4.5(d) through (f), the concrete surface strain developes with time and pull-out force. In stage I, the concrete surface strain keeps increase while the effective pretension force remains the same since the release of the prestressing strand. This indicates the pretension force transfer was a time-dependent process. In the transfer zone, the pretension force transfer to the surrounding concrete, and result in the redistribution of strain within concrete. Higher pretension force causes higher effective pretension force higher concrete surface strain. In stage II, the concrete surface strain increases with the pull-out force. The slope of the strain development curve of the points close to the jacking end was smaller while that close to the free end was steeper. In other words, the concrete strain close to the jacking end always increases faster than that close to the free end with the increase of the pull-out force. Although the maximum pull-out force was close for all 610 mm (24 in.) pretensioned specimens, the measured concrete surface strain was higher for the specimen with higher pretension level, especially the

specimen 2-20. This was because the effective pretension force of specimen 2-20 was significantly lower than the other two specimens, resulting in the smaller concrete surface strain in stage I. As mentioned in the section "Test program", it was one day that was from the strand cutting to the start of the pull-out test, while the pull-out test lasts only three to four hours. Concrete strain distribution is a time-dependent process; longer time helps the transfer of the force from the strand to the concrete and the development of the concrete strain.

The 915 mm (3 ft.) long specimens (3-20, 3-40 and 3-60): As shown in Figure 4.5 (g) through (i), neither apparent force drop nor stand rotation was detected. For the specimen 3-20, 3-40 and 3-60, the effective pretension force after strand release was 72, 130 and 217 kN (16.2, 29.2 and 48.8 kips), respectively. However, for the non-pretensioned 915 mm (36 in.) specimen 3-00A and 3-00B, force drop of small amplitude occurs when the pull-out force exceeds a certain level. Higher pretension level causes larger effective pretension force in the strand for the 915 mm (36 in.) pretensioned specimens, and the effective pretension force does not decrease with time. For the specimen 3-20, 3-40 and 3-60, due to the Hoyer's effect, the free end strand start to move into the concrete until the pull-out force increase from the initial effective pretension force to 96, 202 and 240 kN (21.5, 45.5 and 53.9 kips), respectively.

As shown in Figure 4.5(g) through (i), the development of the concrete surface strain was similar to that of the 610 mm (24 in.) pretensioned specimens. The concrete surface strain developes with time and pull-out force. In stage I, the concrete surface strain keeps increase while the effective pretension force remains the same since the release of the

prestressing strand. Higher pretension force results in higher concrete surface strain, and higher pull-out force results in higher concrete surface strain.

Figure 4.4 Pull-out force versus strand slip at two ends for pretensioned specimens; 1 mm = 0.039 in.; 1 kN = 0.225 kips

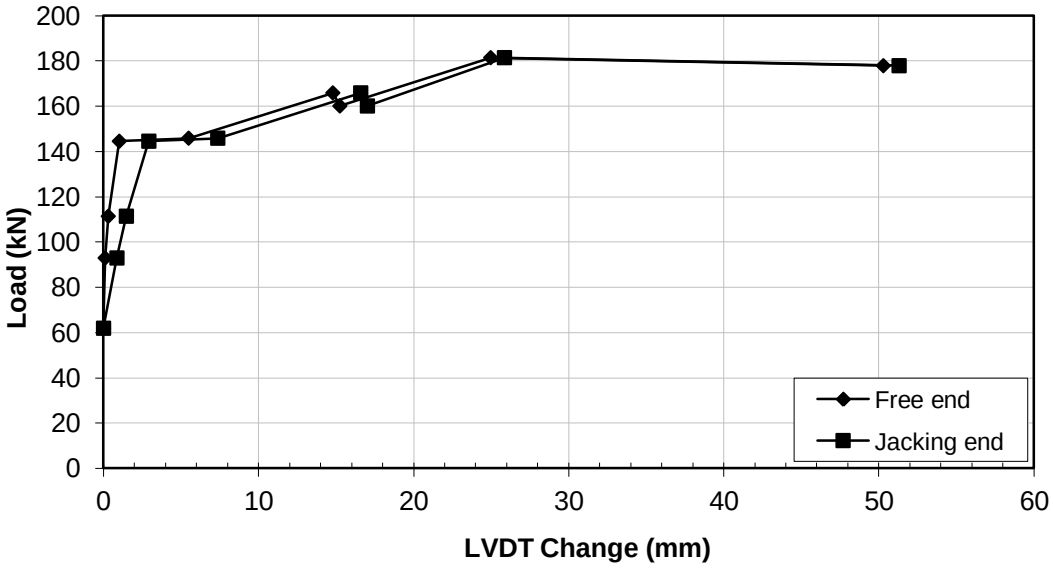

(a) Specimen 1-20

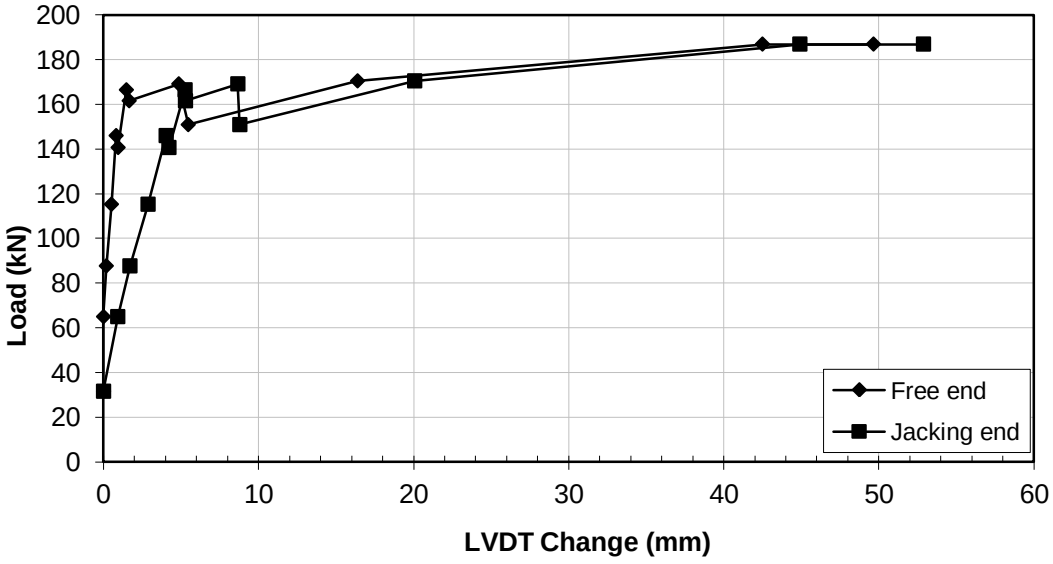

(b) Specimen 1-40

Figure 4.4 continued

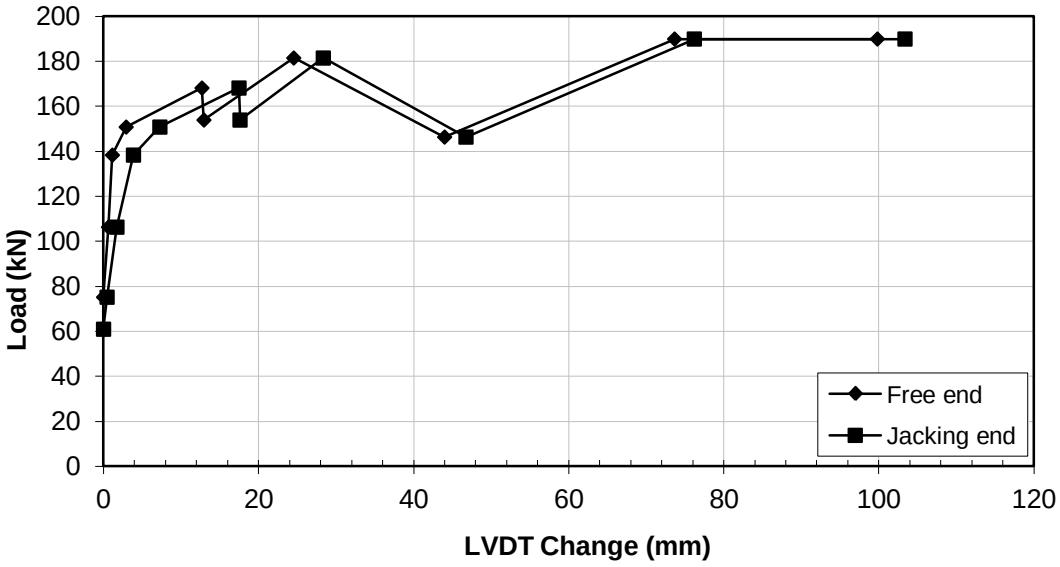

(c) Specimen 1-60

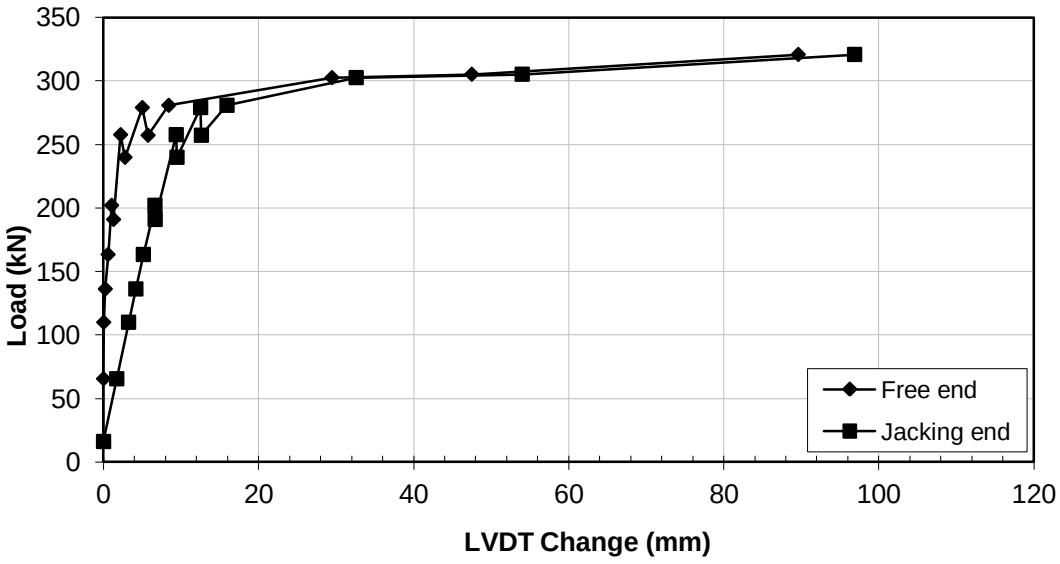

(d) Specimen 2-20

Figure 4.4 continued

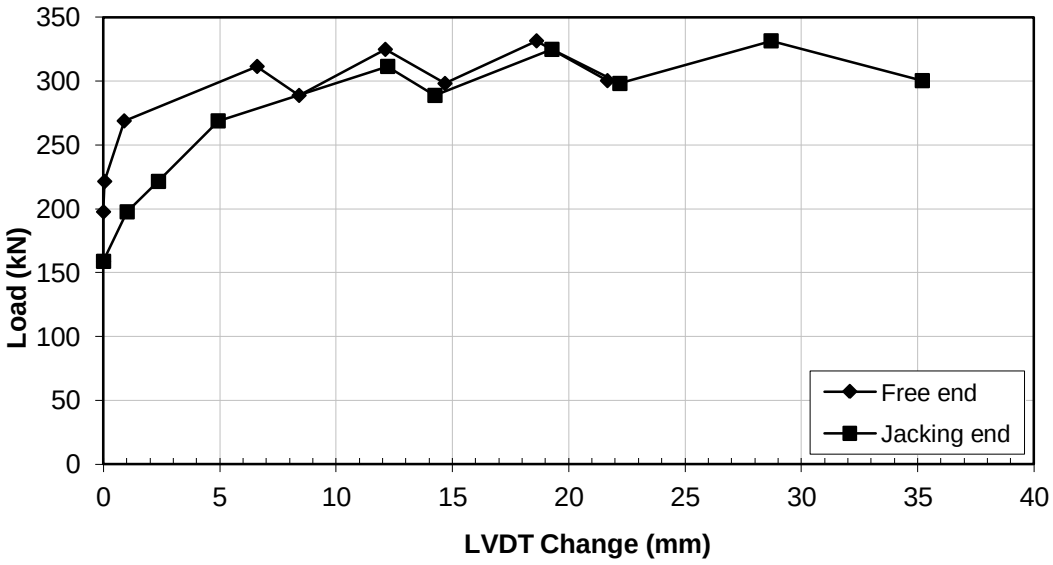

(e) Specimen 2-40

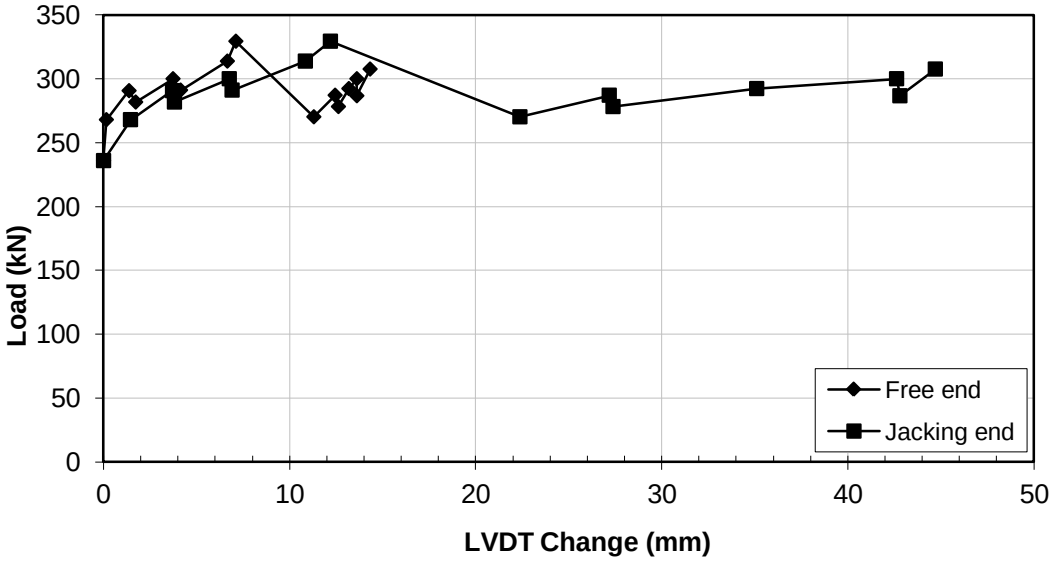

(f) Specimen 2-60

Figure 4.4 continued

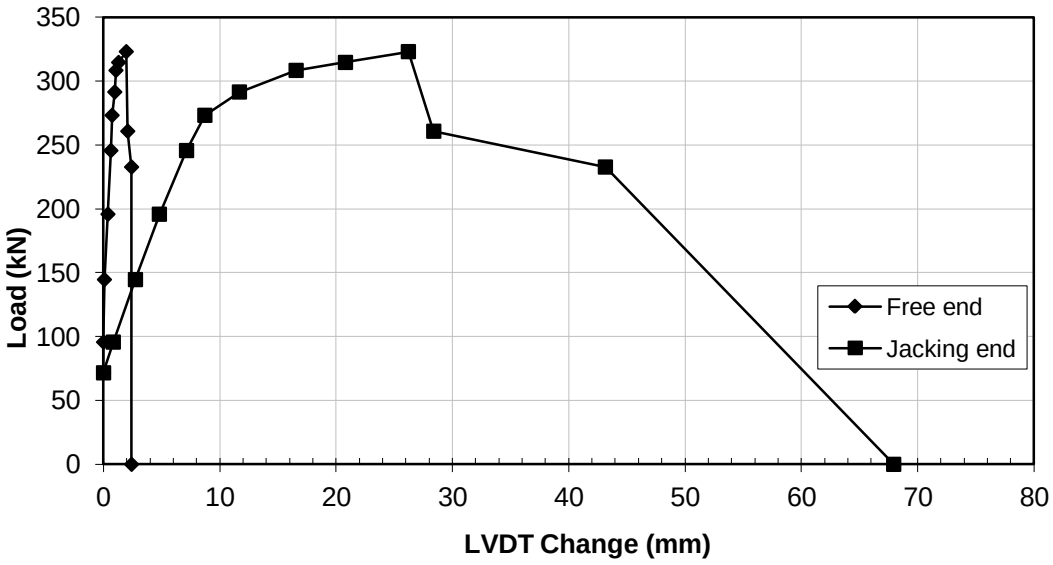

(g) Specimen 3-20

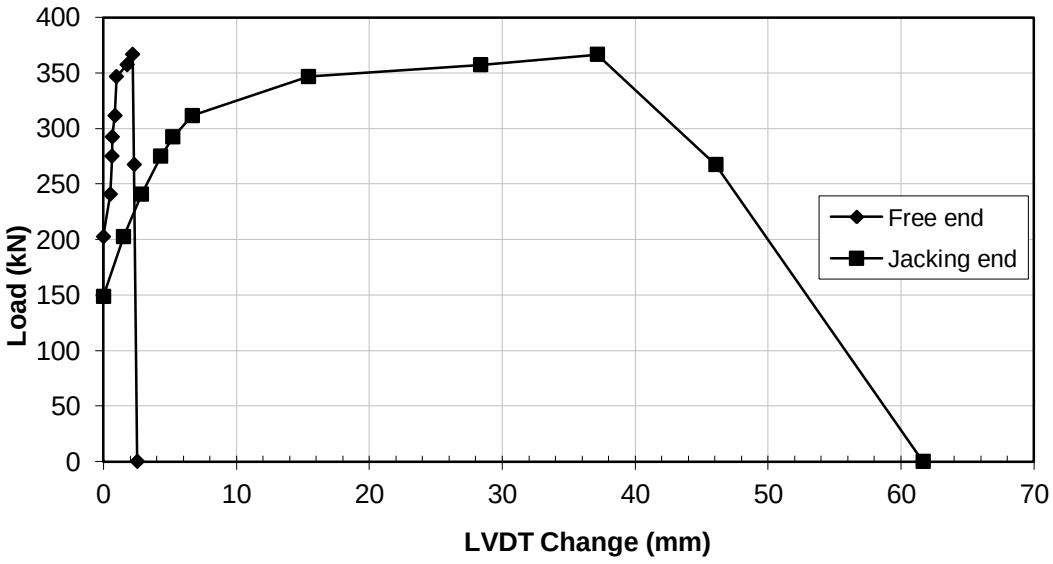

(h) Specimen 3-40

Figure 4.4 continued

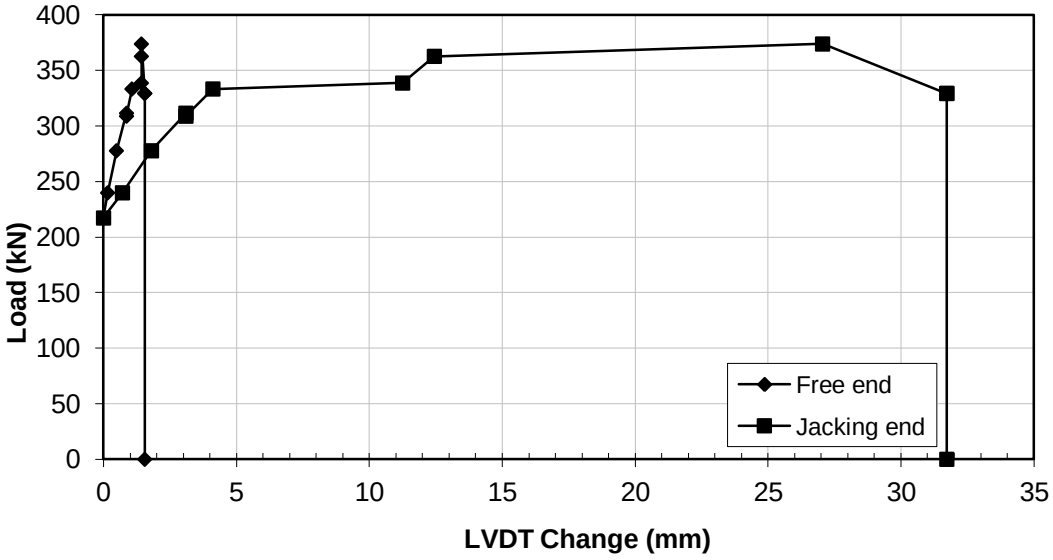

(i) Specimen 3-60

Figure 4.4 continued

Figure 4.5 Development of concrete surface strain for pretensioned specimens; 1kN = 0.225 kips

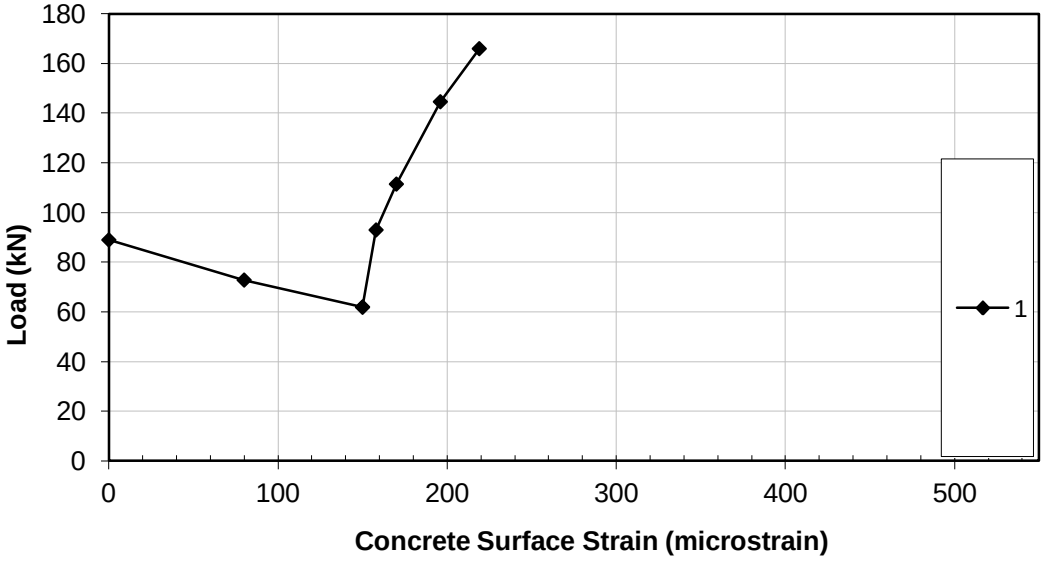

(a) Specimen 1-20

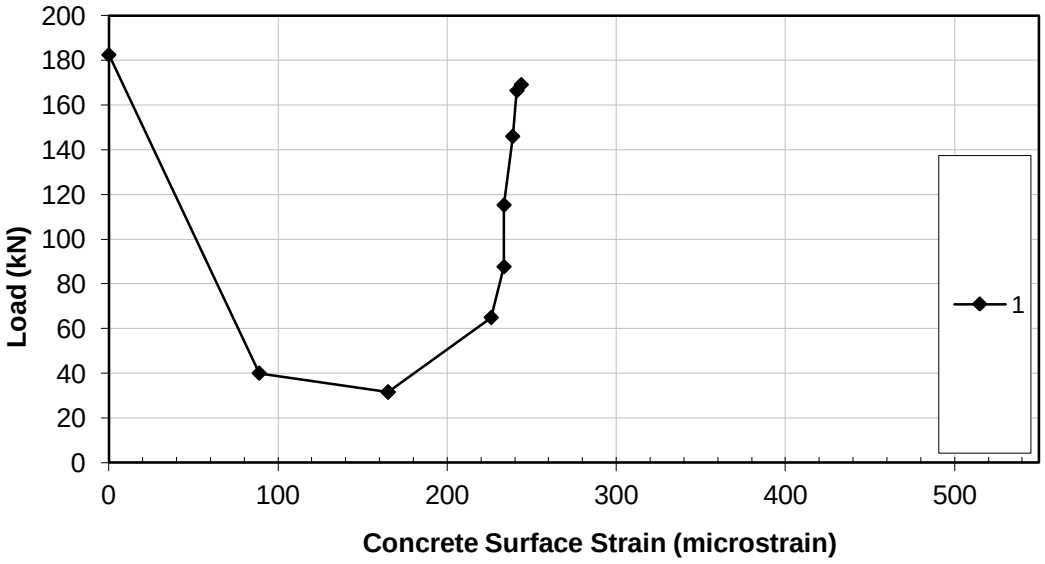

(b) Specimen 1-40

Figure 4.5 continued

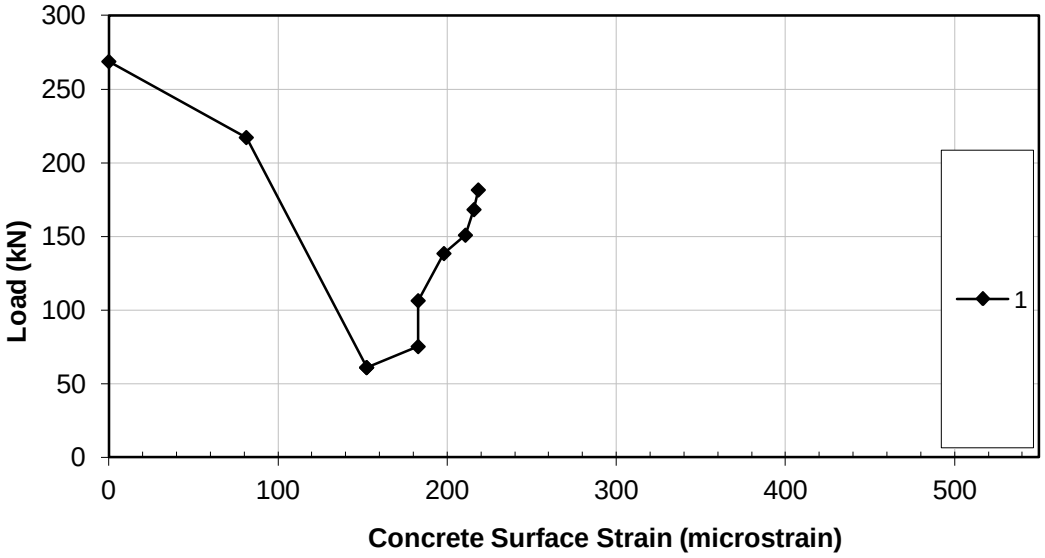

(c) Specimen 1-60

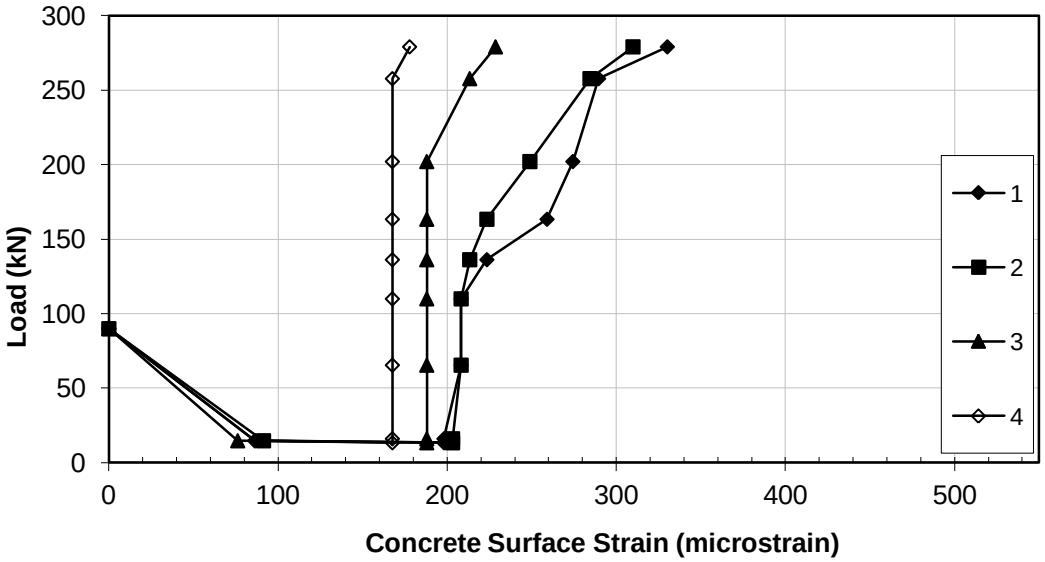

(d) Specimen 2-20

Figure 4.5 continued

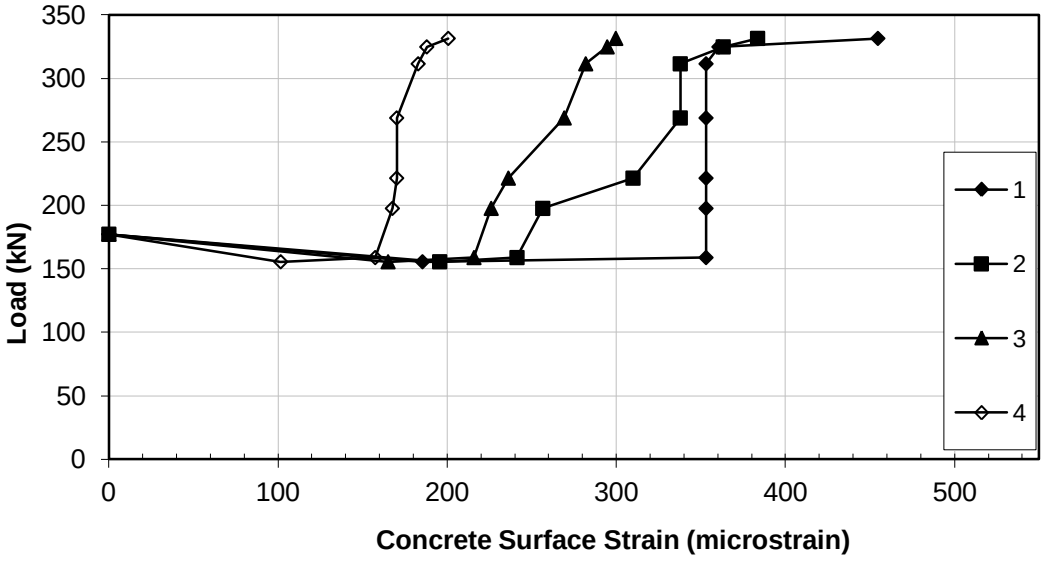

(e) specimen 2-40

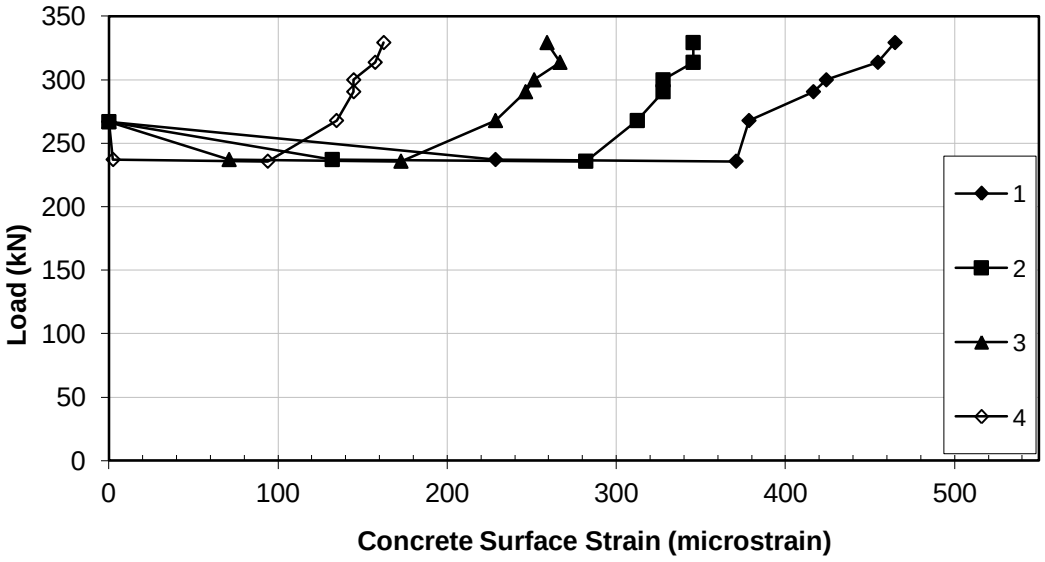

(f) Specimen 2-60

Figure 4.5 continued

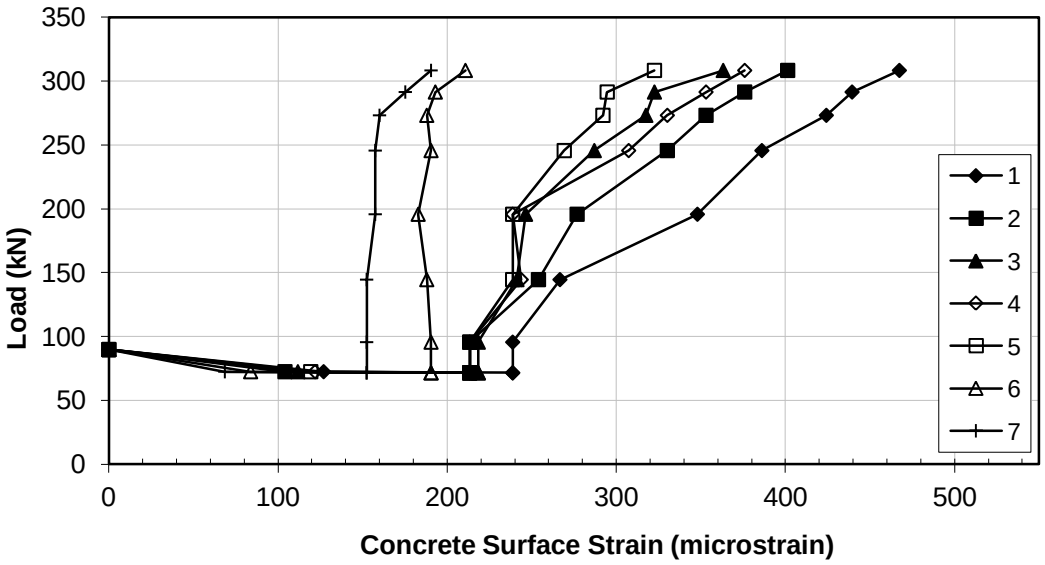

(g) Specimen 3-20

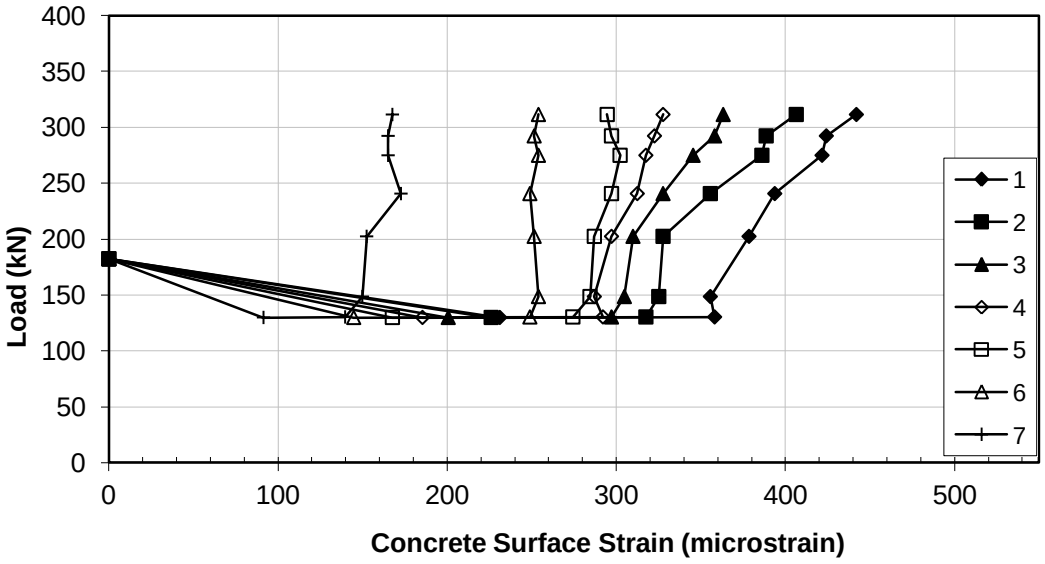

(h) Specimen 3-40

Figure 4.5 continued

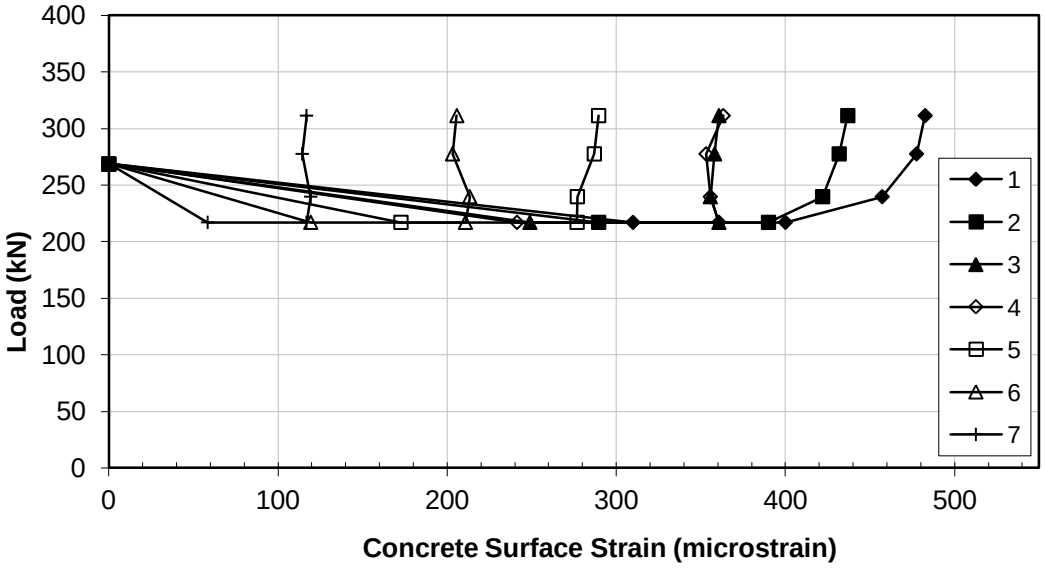

(i) Specimen 3-60

Figure 4.5 continued

4.7 Test Results Analysis and Comparison

One day after concrete cast, the pretensioned strand was cut using an electrical saw. The strand close to the cut point unraveled because of the sudden release of the pretension force, as shown in Figure 4.6. It seems that a higher level of unraveling was accompanied with a larger suck-in. The number in the legends in Figure 4.7 and Figure 4.8 represents the specimen length (unit: ft). For example, the curve 1 represents the results for all three 1 ft (305 mm) pretensioned specimens with 89, 178 and 267 kN (20, 40 and 60 kips) pretensioned levels. As shown in Figure 4.7, higher pretension force results in larger strand suck-in for the specimens of the same length. However, higher pretension level does not always cause larger effective pretension force. In Figure 4.8, for the 610 mm (2ft) and 915 mm (3ft) specimens, higher pretension level leads to larger effective pretension force, and the two curves were close to each other; for the specimens of 305 mm (1ft), the effective pretension force (one day after strand cut) was at the same level despite the different pretension force. This disparity was because of the specimen length. As mentioned, the transfer length for the 18-mm-(0.7-in.-) diameter strand approximates to 610 mm (24 in.) when the pretension force was 75% of the ultimate strand strength. Once the specimen was longer than the transfer length, the bond within the transfer zone can be fully developed to transfer the pretension force from strand to concrete. Otherwise, due to the bond capacity limit, the bond in the end zone (shorter than transfer length) cannot effectively transfer the pretension force no matter how high the pretension level was. In Figure 4.9, two series of concrete surface strain distribution along the specimen was plotted: one was the strain distribution one day after strand cut (just before the pull-out test), and the other was the last measured strain distribution during the pull-out test. The

legend includes two parts: the first part was the specimen ID, and the second part was the corresponding effective pretension force or the pull-out force. As shown in Figure 4.9(a), the concrete surface strain for the 305 mm (12 in.) specimens was located at the lowest level due to the lowest effective pretension force. For the specimen 2-20 and 3-20, the concrete surface strain along the entire specimen was also at the low level due to their low effective pretension force. For the rest specimens in which the effective pretension level was at a higher level, the concrete strain was at a higher level, and concrete strain gradually decrease from the jacking end to the free end. The curves of the specimen 3-40 and 3-60 were located higher than those of the specimen 2-40 and 2-60, and the slope of the former two was smaller than the latter two. In addition, the curve for the 915 mm (36 in.) specimens was composed of two parts: the curve part adjacent to the jacking end was relatively flat and the curve part adjacent to the free end was steeper. In essence, the transfer length was the length from the free end to the point from which concrete strain stay constant. Based on this point, the transfer length for Specimen 3-20, 3-40 and 3-60 were approximately 350 mm, 450 mm and 650 mm, respectively, as marked with arrows in Figure 4.9(a). This indicates that the higher pretension force requires longer transfer length. In Figure 4.9(b), the strain curves for the longer specimens were located at higher positions. The strain distribution along the specimen was approximately linear; the slope of the curves for the longer specimens was smaller than that for the shorter specimens.

One day after strand cut, the pull-out test was conducted. The relationship between the free end strand slip and the pull-out force for both non-pretensioned and pretensioned specimens was plotted in Figure 4.10. The legend in Figure 4.10 shows the specimen ID. For the specimens of the same length, the curves for the pretensioned specimens were

located at higher position than those for the non-pretensioned specimens, and the curves for the pretensioned specimens with higher pretension level were located at higher position. The area enclosed by the curve of force vs. slip can be regarded as the pull-out work; higher position of the curve indicates that larger pull-out work was required to achieve the same free end strand slip. This disparity of required pull-out work was because of the Hoyer's effect. For the non-pretensioned specimens, the strand in the free end starts slip when the pull-out force overcomes the adhesion bond of the entire specimen. Once the chemical adhesion for a part of the strand was lost, the relative slip occurs, activating the friction and mechanical interlock for that part of the strand. Slip occurs at the jacking end at the beginning, and gradually accumulates to cause the free end slip. For the pretensioned specimens, the adhesion was lost since the release of the strand. Due to the Hoyer's effect, the diameter of the prestressing strand swells, causing a high pressure on the surrounding concrete and friction resistance. With the increase of the pull-out force, the external force will result in the increase of the strand tension and decrease of the strand diameter, causing the decrease of the radial pressure on the surrounding concrete. This was detrimental to the Hoyer's effect. When the pull-out force increases to some degree, the strand in the free end starts to move into concrete. The pull-out force at this moment can be regarded as the bond resistance due to the Hoyer's effect. With the further increase of the pull-out force and the strand tension, the decreasing bond contribution from Hoyer's effect will be compensated by mechanical interlock. More involvement of mechanical interlock may increase the total bond capacity to resist the external force. Thus, larger pull-out force was required to activate the free end slip for the longer specimen. As shown in Table 4.1, for the 305, 610 and 915 mm (1 ft., 2 ft. and 3ft.)

non-pretensioned specimens, the free end slip starts when the pull-out force approximates to 10, 30 and 60 kN (2.2, 6.7 and 13.5 kips), respectively. For the pretensioned specimen 1-20, 1-40 and 1-60, the free end slip starts when the pull-out force approximated to 80 kN (18.0 kips). For the pretensioned specimen 2-20, 2-40 and 2-60, the free end slip starts when the pull-out force reach 110, 222 and 268 kN (24.7, 49.9 and 60.2 kips), respectively. For the pretensioned specimen 3-20, 3-40 and 3-60, the free end slip starts when the pull-out force reach 96, 202 and 240 kN (21.6, 45.4 and 54.0 kips), respectively. It reveals that the required pull-out force activating the free end strand slip was close to the pretension force, and larger than the effective pretension force.

In Table 4.1, the behavior difference between the non-pretensioned specimens and the pretensioned specimens was revealed. For the 305 mm (1 ft.) speciemens, the existence of the pretension force results in strand slip as the failure mode, instead of concrete split for the corresponding non-pretensioned specimens; the maximum pull-out force for the pretensioned specimens was close to 190 kN (42.7kips) while that for the non-pretensioned specimens was close to 150 kN (33.7 kips), indicating that the former was approximately 25% higher. For the 610 mm (2 ft.) speciemens, the failure mode was strand slip; the maximum pull-out force for the pretensioned specimens was close to 330 kN or 74.2 kips (approximate 90% of the strand strength) while that for the non-pretensioned specimens was close to 260 kN (58.5 kips), indicating that the former was approximately 25% higher. For the 915 mm (3 ft.) speciemens, the failure mode was strand break at the chuck in the jacking end; therefore, all specimens of this length were regarded to have the same bond capacity although the maximum pull-out force was different. It was noted that the 305 mm (1 ft.) and 610 mm (2 ft.) specimens were within

the transfer zone while the 915 mm (3 ft.) specimens were longer than the transfer length. The main difference of the bond mechanism between the pretensioned and non-pretensioned members was the existence of the Hoyer's effect. 25% higher bond capacity for the pretensioned 305 mm (1 ft.) and 610 mm (2 ft.) specimens was due to the Hoyer's effect. For the 915 mm (3 ft.) specimens, although the bond capacity was the same for both non-pretensioned and pretensioned specimens, the components of bond mechanism were different. The bond capacity for the non-pretensioned specimens was dependent of the friction and mechanical interlock while the bond capacity for the pretensioned specimens was composed of Hoyer's effect and mechanical interlock. By comparison of the measured maximum concrete surface strain, the strain for the pretensioned specimens was approximately 60% higher than that for the non-pretensioned specimens. In addition, the different bond behavior for non-pretensioned and pretensioned specimens of different length can be studied based on the existence of force drop and strand rotation, as shown in Table 4.1. Due to the pretension force, the extent of force drop and strand rotation could be reduced or even eliminated, indicating its stronger bond compared to the non-pretensioned members.

Figure 4.6 Different levels of Suck-in and strand unraveling

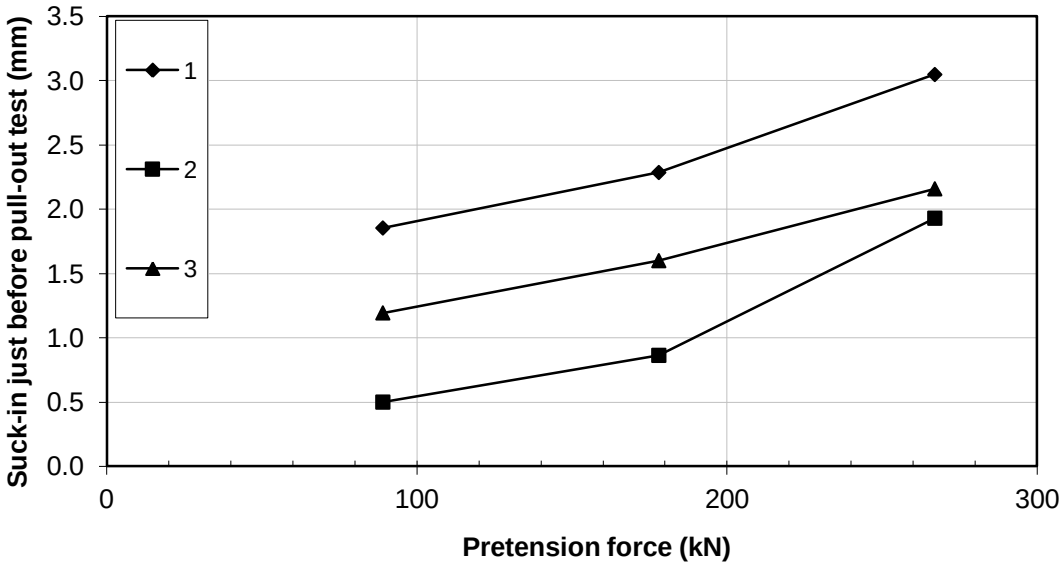

Figure 4.7 Suck-in versus pretension force; 1 mm = 0.0393 in.; 1 kN = 0.2248 kips

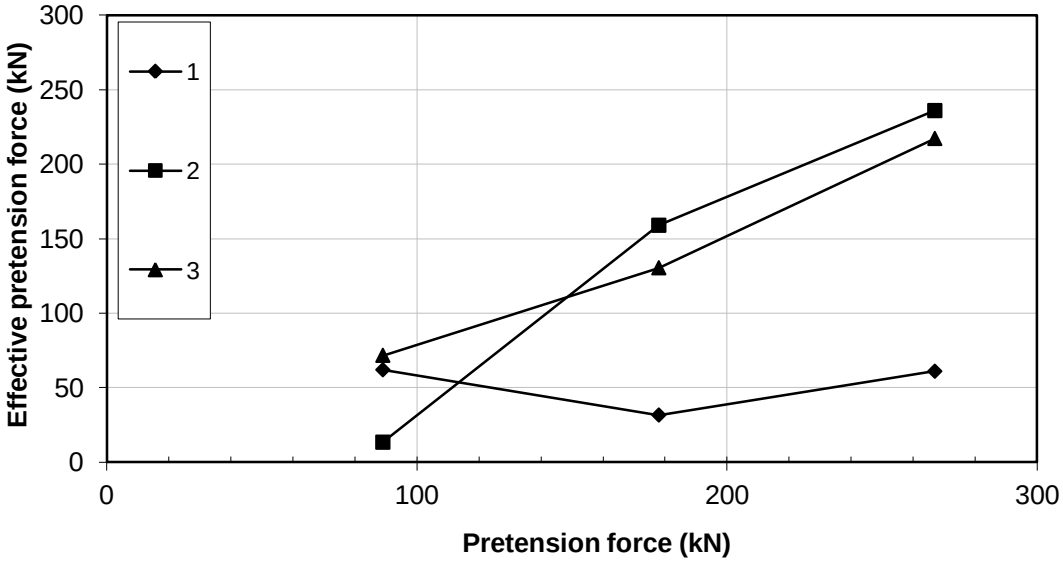

Figure 4.8 Effective pretension force versus pretension force; 1 kN = 0.2248 kips

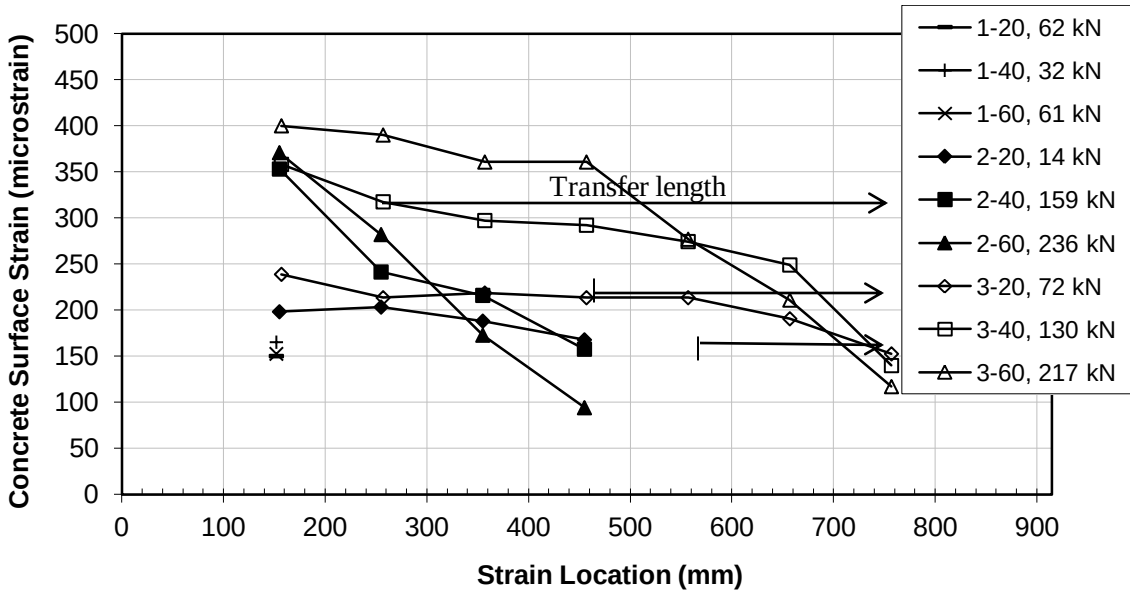

(a) Strain distribution one day after strand cut

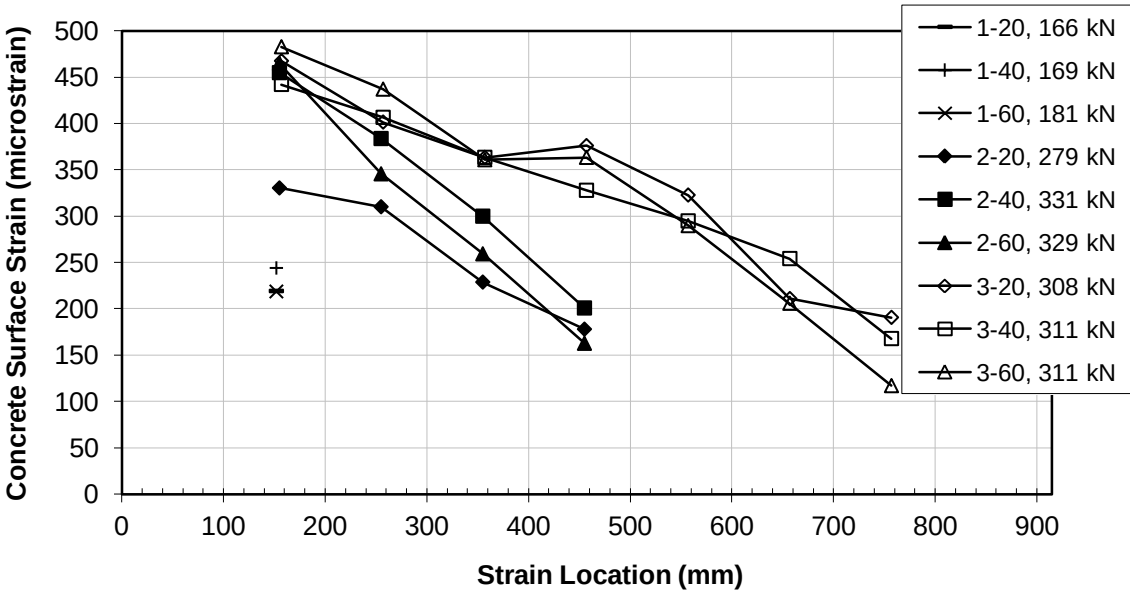

(b) The last measured strain distribution during the pull-out test

Figure 4.9 Strain distribution at specific load steps; 1 mm = 0.0393 in.

Figure 4.10 Comparison of force-slip curves during pull-out stage; 1 mm = 0.0393 in.; 1 kN = 0.2248 kips

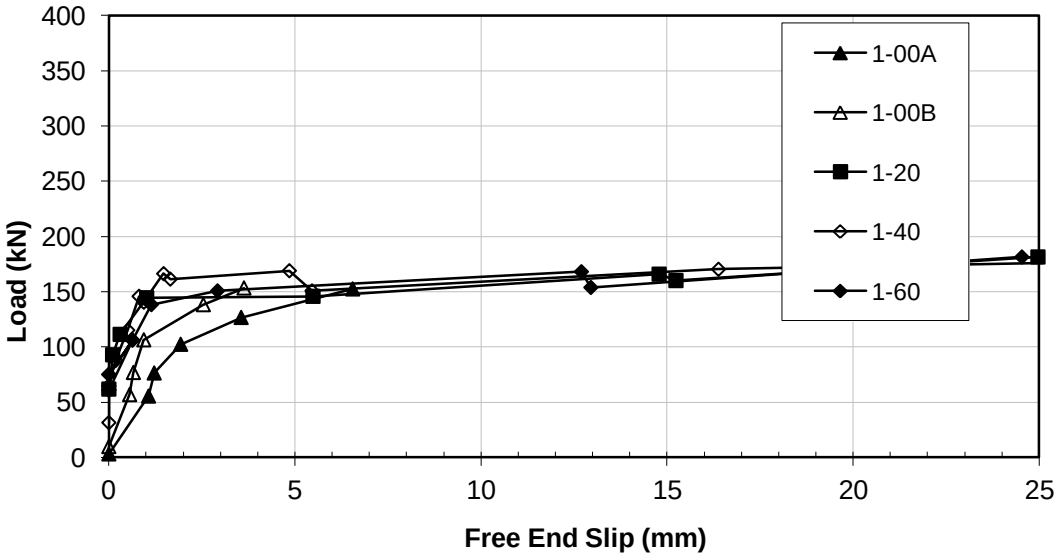

(a) 305 mm (1 ft.) specimens

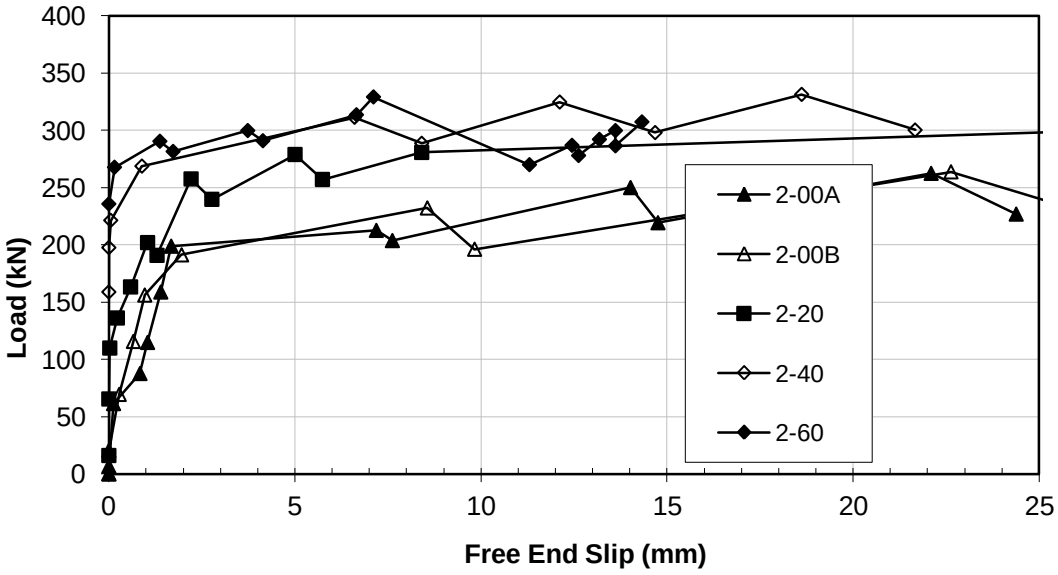

(b) 610 mm (2 ft.) specimens

Figure 4.10 continued

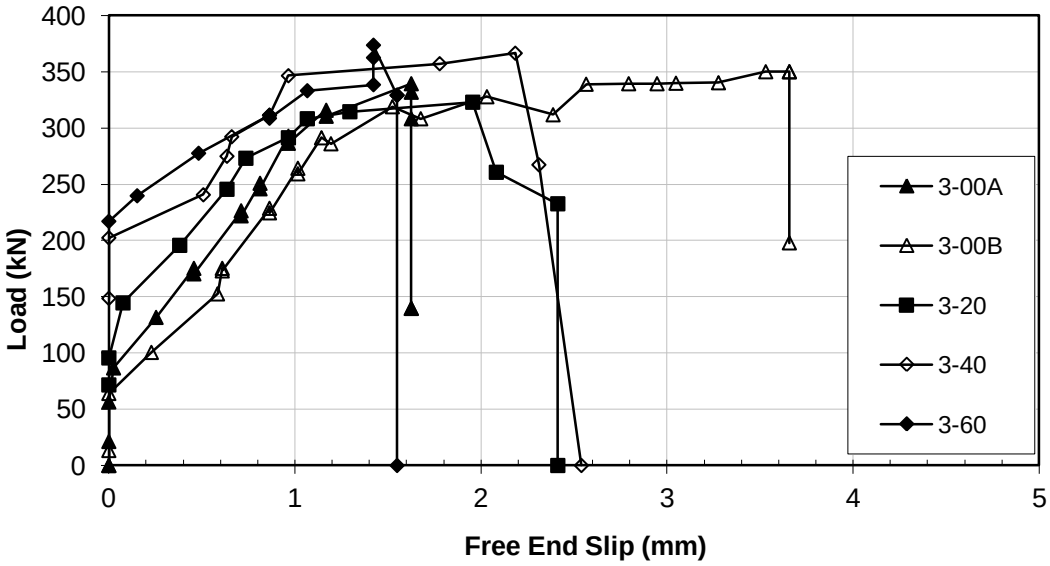

(c) 915 mm (3 ft.) specimens

Figure 4.10 continued

4.8 Conclusions and Discussion

A reliable and feasible pretensioned pull-out test method was proposed in this chapter, contributing to better understand the bond mechanism and evaluate the bond behavior of pretensioned strand. The bond behavior of the 18-mm-(0.7-in.-) diameter strand was studied with consideration of specimen length (strand embedment length) and pretension level. Three sets of pretensioned pull-out tests of specimens with different lengths were tested, and there were three different pretension levels for each set. The specimens were investigated at two stages: transfer stage and pull-out stage. The different bond behavior can be investigated based on the relationship between the pull-out force and strand slip, the extent of force drop and strand rotation, the concrete surface strain development and distribution, and the failure mode. By comparison of the pull-out test results for both pretensioned specimens and non-pretensioned specimens, the bond mechanism was quantitatively studied. In particular, the Hoyer's effect, which was active exclusively within the transfer zone for the pretensioned members, was analyzed based on the pull-out test. The conclusions can be drawn as follows:

1. The pretension level affects the bond behavior significantly; larger pull-out work was required to cause the same free end strand slip for the specimen with higher level pretension. For the specimens of the same length, the pull-out-force-slip curves for the pretensioned specimens were located at higher position than those for the non-pretensioned specimens, and the curves for the pretensioned specimens with higher pretension level were located at higher position. The higher position of the curve indicates the larger pull-out work.

2. The pull-out test results for the pretensioned prisms with different strand embedment length were different. For the 305 mm (1 ft.) pretensioned specimens, the failure mode was strand slip, and both apparent force drop and strand rotation occur during the pull-out test. For the 610 mm (2 ft.) pretensioned specimens, although the failure mode was still strand slip, no apparent strand rotation was detected. For the 915 mm (3 ft.) pretensioned specimens, the failure mode was strand break at the chuck; neither force drop nor strand rotation was detected. For the non-pretensioned 305, 610 and 915 mm (1, 2 and 3 ft.) specimens, their failure mode was concrete split, strand slip and strand break, respectively.
3. The effective pretension force was dependent of both the pretension level and specimen length; a higher pretension force requires longer transfer length. For the 305 mm specimens, which were the half length of the typical transfer length, the effective pretension was at the same low level no matter how high the pretension force was. For the 610 and 915 mm (2 and 3 ft.) specimens, the higher pretension force lead to higher effective pretension after strand cutting. This difference could be explained by the bond capacity limit for the shorter specimen. Once the specimen was longer than the transfer length, the bond within the transfer zone can be fully developed to transfer the pretension force from strand to concrete. Otherwise, due to the bond capacity limit, the bond in the end zone (shorter than transfer length) cannot effectively transfer the pretension force no matter how high the pretension level was. From the concrete surface strain distribution along the specimen at transfer, for the specimens at 89, 178 and 267 kN (20, 40 and 60 kips) pretension level, the transfer length approximate to 350, 450, and 650 mm

(13.8, 17.7 and 25.6 in.), respectively. This also verifies that higher pretension force requires longer transfer length.

4. During the pull-out test, the concrete strain close to the jacking end always increase faster than that close to the free end, indicating that the pull-out force was gradually transferred from the jacking end to the free end. For the concrete strain distribution, when the pull-out load was close to the maximum, the strain distribution along the specimen was approximately linear; the slope of the curves for the longer specimens was smaller than that for the shorter specimens while the strain curves for the longer specimens were located at higher positions.
5. The Hoyer's effect was evaluated quantitatively in two ways: the required pull-out force activating free end strand slip, and the maximum pull-out force. For the pretensioned specimen 1-20, 1-40 and 1-60, the free end slip starts when the pull-out force approximated to 80 kN (18.0 kips). For the pretensioned specimen 2-20, 2-40 and 2-60, the free end slip starts when the pull-out force reach 110, 222 and 268 kN (24.7, 49.9 and 60.2 kips), respectively. For the pretensioned specimen 3-20, 3-40 and 3-60, the free end slip starts when the pull-out force reach 96, 202 and 240 kN (66.5, 45.4 and 54.0 kips), respectively. Higher effective pretension force will cause the Hoyer's effect more notable. Next, due to the Hoyer's effect, the maximum pull-out force (the bond capacity) for the pretensioned 305mm (1 ft.) and 610 mm (2 ft.) specimens was 190 and 330 kN (42.7 and 74.2 kips) while that for non-pretensioned 305mm (1 ft.) and 610 mm (2 ft.) specimens was 150 and 260 kN (33.7 and 58.5 kips); the bond capacity for pretensioned specimens was 25 % higher than that for the non-pretensioned specimens. For the 915 mm (3 ft.)

specimens, the bond capacity was the same (the ultimate force was the strand break strength 353 kN or 79.4 kips) for both non-pretensioned and pretensioned specimens because the mechanical interlock compensates the lack of Hoyer's effect for the non-pretensioned members.

Through the pull-out tests of both non-pretensioned and pretensioned specimens, the understanding of the bond behavior was more comprehensive with consideration of the specimen length and pretension level. To begin with, the proposed pretensioned pull-out test could be applied to analyze the bond in the transfer zone. Stand slip could be regarded as an anchorage failure. For the pretensioned concrete members, the weakening or the damage of the Hoyer' effect in the transfer zone may result in anchorage failure. Within the transfer zone, when the strand tension force was larger to some extent than the effective pretension at transfer, the free end strand start to slip, indicating the damage of the Hoyer's effect. For the pretensioned concrete members, if the tension force at the transfer length can be controlled to make the Hoyer's effect effective, the anchorage failure in the transfer zone may be avoided. In addition, the flexural bond may be evaluated based on the pull-out test. If the pretensioned specimen was enough long, the free end slip could be zero even though the pull-out force reaches the breaking strength of the strand. The development length of the pretensioned strand may be obtained through the pull-out test. In this way, no trial-and-error beam test is needed to analyze the development length.

Chapter 5 : Conclusions and Future Work

This chapter summarizes the accomplishments of this study along with conclusions and recommendations for the future research.

5.1 Conclusions

The bond performance of the 18-mm-(0.7-in.-) diameter strand was studied. The finite element method was applied to analyze the factor influencing the transfer length. Both non-pretensioned and pretensioned pull-out tests were introduced to investigate the bond behavior. Based on the finite element analysis and experimental study, the following conclusions were made:

1. The parametric analysis of the partially bonded FE models indicated that the transfer length increased with the decrease of the friction coefficient, and the slip at the end increased with the decrease of friction coefficient. 50.8 mm (2 in.) spacing of adjacent strands could be appropriate for 18-mm-diameter strand.
2. For the non-pretensioned pull-out test, the specimens with different strand embedment length had different failure modes. For the 0.5 Lt, 1 Lt and 1.5 Lt non-pretensioned speciemen, their failure mode was concrete split, strand slip and strand break, respectively.
3. For the non-pretensioned pull-out test, the relationship between the pull-out force and the free end strand slip was different for the specimens with different strand embedment length. For the 0.5 Lt specimen, the curve was parabolic until a sudden concrete splitting. For the 1 Lt specimen, the free end slip increased linearly initially with the pull-out force, and then the curve reached a plateau where the slip continuously increased while the pull-out force fluctuated. For the

1.5 Lt specimen, the free end slip initially linearly increased slowly with the force, then the slip increased faster than before, and finally the strand broke. The ultimate free end slip for the 0.5 Lt and 1.5 Lt specimens was very small due to their brittle failure.

4. For the non-pretensioned pull-out test, although the maximum pull-out force for the longer specimen was larger, the shorter specimen had a greater bond capacity per unit length. The initial slope of the force-free end slip curves of the longer specimen was significantly greater than that of the shorter specimen.
5. For the pretensioned pull-out test, the strand embedment length also affected the failure mode. For the 305 mm (1 ft.) pretensioned specimens, the failure mode was strand slip, and both apparent force drop and strand rotation occur during the pull-out test. For the 610 mm (2 ft.) pretensioned specimens, although the failure mode was still strand slip, no apparent strand rotation was detected. For the 915 mm (3 ft.) pretensioned specimens, the failure mode was strand break at the chuck; neither force drop nor strand rotation is detected.
6. The force drop and strand rotation may be detected in the step-loaded pull-out test. Their occurrence was related to the strand embedment length and the pretension level.
7. The pretension level affected the bond behavior significantly; larger pull-out work was required to cause the same free end strand slip for the specimen with higher level pretension.
8. The effective pretension force was dependent on both the pretension level and specimen length; a higher pretension force required longer transfer length. From

the concrete surface strain distribution along the specimen at transfer, for the specimens at 89, 178 and 267 kN (20, 40 and 60 kips) pretension level, the transfer length was approximately 350, 450, and 650 mm (13.8, 17.7 and 25.6 in.), respectively.

9. The force activating the free end strand slip was investigated. For the non-pretensioned specimen, the free end strand started to slip once the adhesion along the entire strand was lost. For the pretensioned specimen, the free end strand slip was caused by the weakening or damage of Hoyer's effect when the increasing tension in strand results in the decrease of the strand diameter and radial pressure on concrete.
10. The adhesion between strand and concrete was studied based on the non-pretensioned pull-out test. The pull-out force activating the free end strand slip for 305, 610 and 915 mm (1, 2 and 3 ft.) specimens was approximately 10, 30, and 60 kN (2.2, 6.7 and 13.5 kips), respectively.
11. Based on the pretensioned pull-out test, the Hoyer's effect was evaluated quantitatively in two ways: the required pull-out force activating free end strand slip, and the maximum pull-out force. For the pretensioned specimen 1-20, 1-40 and 1-60, the free end slip starts when the pull-out force was approximatly 80 kN (18.0 kips). For the pretensioned specimen 2-20, 2-40 and 2-60, the free end slip starts when the pull-out force reached 110, 222 and 268 kN (24.7, 49.9 and 60.2 kips), respectively. For the pretensioned specimen 3-20, 3-40 and 3-60, the free end slip started when the pull-out force reached 96, 202 and 240 kN (66.5, 45.4 and 54.0 kips), respectively. Higher effective pretension force will cause the

Hoyer's effect more notable. Next, due to the Hoyer's effect, the maximum pull-out force (the bond capacity) for the pretensioned 305mm (1 ft.) and 610 mm (2 ft.) specimens was 190 and 330 kN (42.7 and 74.2 kips) while that for non-pretensioned 305mm (1 ft.) and 610 mm (2 ft.) specimens was 150 and 260 kN (33.7 and 58.5 kips), respectively; the bond capacity for pretensioned specimens was 25 % higher than that for the non-pretensioned specimens. For the 915 mm (3 ft.) specimens, the bond capacity was the same (the ultimate force is the strand break strength 353 kN or 79.4 kips) for both non-pretensioned and pretensioned specimens because the mechanical interlock compensates the lack of Hoyer's effect for the non-pretensioned members.

12. Force drop and the concrete surface strain change over time during the pull-out test indicate that bond is a time-dependent process.

5.2 Future Work

With the existing pull-out test results, a mathematical model to predict the bond behavior should be developed. The relationship between the bond stress and the strand slip should be introduced into the finite element analysis to help predict bond behavior for the large-scale pretensioned structures. In addition, the proposed pull-out test has provided a new thinking way to determine the transfer length; similarly, the development length may be determined based on the pull-out test.

References

AASHTO. (2012). “AASHTO LRFD bridge design specifications.” sixth Edition, American Association for State Highway and Transportation Officials, 2012, Washington, D.C.

Abrishami, H. H., and Mitchell, D. (1993). “Bond characteristics of pretensioned strand.” ACI Materials Journal, 90(3): 228-235.

ASTM. (2011). “Standard test method for evaluating bond strength for 0.600-in. (15.24-mm) diameter prestressing steel strand, grade 270 (1860), uncoated, used in prestressed ground anchors.” A981, West Conshohocken, PA.

ASTM (2012). “Standard test method for compressive strength of cylindrical concrete specimens.” C39, West Conshohocken, PA.

Baxi, A. N. (2005). “Analytical modeling of fully bonded and debonded pre-tensioned prestressed concrete members.” Ph.D. Dissertation, University of Texas at Austin. TX, 2005, 451 pp.

Bolmsvik, R., and Lundgren, K. (2006). “Modelling of bond between three-wire strands and concrete.” Magzine of Concrete Research, 58(3): 123-133.

Brearley, L. M., and Johnston, D. W. (1990). “Pull-out bond tests of epoxy-coated prestressing strand.” Journal of Structural Engineering, 116(8): 2236-2252.

Burgueno, R., and Sun, Y. (2011). “Effects of debonded strands on the production and performance of prestressed concrete beams.” Report CEE-RR-2011/01, Michigan State University, East Lansing, MI, 180 pp.

Guyon. Y. (1953). “Prestressed concrete.” Contractors Record and Municipal Engineering, London.

Hanson, N. W., and Kaar, P. H. (1959). “Flexural bond tests of pretensioned prestressed beams.” ACI Journal, Proceedings, 55(7): 783-802

Hoyer, E., and Friedrich, E. (1939). “Beitrag zur Frage der Haftspannung in Eisenbetonbauteilen,” Beton und Eisen, 30(6): 107-110.

Janney, J. R. (1954). “Nature of bond in pre-tensioned prestressed concrete,” Journal of the American Concrete Institute, May, Proceedings, 50: 717-736.

Kannel, J., French, C. and Stolarski, H. (1997). “Release methodology of strands to reduce end cracking in pre-tensioned concrete girders.” PCI Journal, 42(1): 42-54.

Leonhardt, F. (1964). “Prestressed concrete: design and construction.” Wilhelm Ernst & Sohn, Berlin Munich.

Logan, D. R. (1997). “Acceptance criteria for bond quality of strands for pretensioned prestressed concrete application.” PCI Journal, 42(2): 52-90.

Ma, Z. J., and Burdette, E. G. (2011). “Transfer length and girder-end confinement of aashto-pci bt girders with larger capacity prestressing strands.” Technical Report: RES-2010-23, The University of Tennessee Knoxville, Knoxville, TN, 139 pp.

Morcous, G., Hanna, K., and Tadros, M. (2010). “Transfer and development length of 0.7 in. diameter strands in pretensioned concrete bridge girders.” http://www.hpcbridgeviews.com/i64/Article3.asp (Apr. 2012).

Morcous, G., Hatami, A., Maguire, M., Hanna, K., and Tadros, M. K. (2012). “Mechanical and bond properties of 18-mm-(0.7-in.-)diameter prestressing strands.” Journal of Materials in Civil Engineering ASCE, 24(6): 735-744.

Moustafa, S. (1974). “Pull-out strength of strand and lifting loops.” Concrete Technology Associates Technical Bulletin, 74-B5, Precast/Prestressed Concrete Institute, Chicago.

Ramirez, J., and Russell, B. (2008). “Transfer, development, and splice length for strand/reinforcement in high-strength concrete.” NCHRP Report 603, Washington, DC.

Rose, D. R. and Russell, B. W. (1997). “Investigation of standardized tests to measure the bond performance of prestressing strand.” PCI Journal, 42(4): 56-80.

Russell, B.W., and Burns, N. H. (1993). “Design guidelines for transfer, development and debonding of large diameter seven wire strands in pretensioned concrete girders.” Report No. 1210-5F, Center for Transportation Research, University of Texas at Austin, TX.

Russell, B. W., and Burns, N. H. “ measured transfer lengths of 0.5 and 0.6 in. strands in pretensioned concrete,” PCI Journal, Vol. 49, No.3, September-October, 1996, pp.44-65.

Schuler, G. (2013). “Producer’s Experience with 10,000 psi Concrete and 0.7-in. Diameter Strands.” HPC Bridge Views, <http://www.hpcbridgeviews.com/i54/Article4.asp> (Aug. 2013), No. 54, 2009.

Song, W., Ma, Z., Vadivelu, J., and Burdette, E. (2013), “Transfer Length and Splitting Force Calculation for Pretensioned Concrete Girders with High-capacity Strands,” ASCE Journal of Bridge Engineering, posted ahead of print October 7. doi:10.1061/(ASCE)BE.1943-5592.0000566.

Stocker, M. T., and Sozen, M. A. (1970). “Investigation of prestressed reinforced concrete for highway bridges, part V: Bond characteristics of prestressing strand.” Engineering Experiment Station Bulletin 503, University of Illinois, Urbana-Champaign, IL.

Tabatabiai, H. and Dickson, T. J. (1993). "The history of the prestressing strand development length equation." PCI Journal, 38(6): 64-75.

Appendix: Other Papers Published during the Dissertation Research Program

Jiang, X., Ma, Z., and Ren, W. (2012). "Crack Detection from the Slope of the Mode Shape Using Complex Continuous Wavelet Transform," Computer-Aided Civil and Infrastructure Engineering, Vol. 27, No. 3, pp. 187 - 201

Jiang, X., Ma, Z. and Song, J. (2012). "Effect of Shear Stud Connections on Dynamic Response of an FRP Deck Bridge under Moving Loads," Journal of Bridge Engineering, Vol. 18, No. 7, pp. 644 - 652

Computer-Aided Civil and Infrastructure Engineering **27** (2012) 187–201

Crack Detection from the Slope of the Mode Shape Using Complex Continuous Wavelet Transform

Xin Jiang

School of Civil Engineering and Architecture, Central South University, Changsha, China & Department of Civil and Environmental Engineering, University of Tennessee, Knoxville, TN, USA

Zhongguo John Ma*

Department of Civil and Environmental Engineering, University of Tennessee, Knoxville, TN, USA

&

Wei-Xin Ren

School of Civil Engineering and Architecture, Central South University, Changsha, China

Abstract: *A new method for cracks detection in beams is proposed by using the slope of the mode shape to detect cracks, and by introducing the angle coefficients of complex continuous wavelet transform. This study is aimed at detecting the location of the nonpropagating transverse crack. A series of beams with cracks that are simulated by rotational springs with equivalent stiffness are analyzed. The mode shape and the slope of this lumped crack model are calculated. Through complex continuous wavelet transform of the slope of the mode shape using Complex Gaus1 wavelet (CGau1), the locations of cracks are detected from the modulus line and the angle line of wavelet coefficients. By comparison, the singularity is much more apparent from the angle line of complex continuous wavelet transform. This demonstrates that the proposed method outperforms the existing method of wavelet transform of the mode shape with real wavelets. Also, this method can detect cracks in beams with different boundary conditions. The influence of crack locations and crack depth on crack detection is discussed. Finally, the noise effect is studied. Through the multiscale analysis, the locations of cracks may be detected from the angle of wavelet coefficients.*

*To whom correspondence should be addressed. E-mail: *zma2@utk.edu*.

DOI: 10.1111/j.1467-8667.2011.00734.x

1 INTRODUCTION

In recent years, structural health monitoring and damage detection have increasingly captured the attention of many researchers (Surace and Ruotolo, 1994; Al-Khalidy et al., 1997; Ren and De Roeck, 2002a,b; Ren and Jaishi, 2006; Jiang and Adeli, 2007; Xu et al., 2007; Ren et al., 2008; Moaveni et al., 2009; Jafarkhani and Masri, 2011; Xia et al., 2011). Cracks have the potential to degrade the integrity of the structure, hence it is important to identify cracks and repair resultant damage in time to assure the safety and durability of the structure. Since cracks result in the decrease of local stiffness and the increase of damping, contributing to changes of frequencies and vibration mode shapes (Chondros and Dimarogonas, 1980; Yuen, 1985), most of the reported modal parameter-based damage detection methods try to find the correlations between damage and modal parameters (Pandey et al., 1991; Kim and Stubbs, 2002; Yin et al., 2010).

Because of its localization characteristics, wavelet transform helps to examine local data with a fine focus to provide multiple levels of details and approximations of signals (Mallat, 2001). In the past decade, wavelet transform has been a prominent tool applied in many fields, such as transportation engineering

(Adeli and Karim, 2000; Adeli and Samant, 2000; Samant and Adeli, 2000, 2001; Ghosh-Dastidar and Adeli, 2003, 2006; Jiang and Adeli, 2004), earthquake engineering (Zhou and Adeli, 2003a,b), and structural engineering (Jiang and Adeli, 2005; Kim and Adeli, 2005a,b; Adeli and Jiang, 2006; Jiang et al., 2007). As an extension of the Fourier transform with adjustable window location and size (Daubechies, 1992), this method becomes popular in damage detection. Han et al. (2005) introduced wavelet packet energy rate index to detect damage; both simulation and experiment showed that this index was sensitive to structural local damage in beams. Ren and Sun (2008) tested a series of damaged beams and an intact beam, and detected damage from measured vibration signals based on wavelet transform combined with Shannon entropy.

To date, several researchers have tried to detect cracks in beams via wavelet transform of static deflection profile or vibration mode shape. Liew and Wang (1998) presented the attempt of an application of wavelet transform in the spatial domain crack identification of structures. They identified the position of a transverse open crack in a simply supported beam, whereas such a crack was hardly detected via traditional eigenvalue analysis. Quek et al. (2001) examined the sensitivity of wavelet technique in the detection of cracks in beams. The crack location was determined and its depth was estimated through the wavelet analysis of the vibration mode of a cracked cantilever beam. Hong et al. (2002) identified the depth of a crack via continuous wavelet transform (CWT) and implemented the Lipschitz exponent as an indicator of the damage extent. Douka et al. (2003) analyzed the fundamental vibration mode of a cracked cantilever beam based on CWT. The position of the crack was determined by the sudden change in the spatial variation of the transformed response, and the size of the crack was predicted by an established intensity factor that related the depth of the crack to the coefficients of CWT. Ovanesova and Suarez (2004) conducted numerical studies on a fixed-end beam and detected the crack based on wavelet transform of response signal from static or dynamic loads. Spanos et al. (2006) discussed spatial wavelet analysis of the static displacement of Euler–Bernoulli damaged beams, and built a wavelet transform modulus map eliminating boundary effect. Chasalevris and Papadopoulos (2006) analyzed the dynamic behavior of a shaft with two cracks that were characterized by depth, position, and relative angle. The method can identify these three parameters of cracks. Cao and Qiao (2008) proposed a novel methodology of using integrated wavelet transform to vibration mode shapes. This technique can improve the robustness of abnormality analysis of mode shape and identify minor damage in a relatively lower signal-to-noise ratio (SNR) environment. Umesha et al. (2009) used results of wavelet (Symlet) transform of the static deflection profile and carried out a parametric study through varying location and size of crack, intensity of load, flexural rigidity, and length of the beam. In these cases, a crack model was introduced and crack was identified based on wavelet analysis results of static deflection profile or vibration mode shape. However, the singularity is not evident enough to localize cracks because sometimes the wavelet coefficients near cracks are too small due to boundary condition, cracks location, cracks depth, or noise effect. Thus, it is meaningful to obtain distinct characteristics of wavelet coefficients at cracks to identify singularity.

It is known that crack influences the curvature and the slope more than the deflection of the beam, because the curvature is the second derivative of the deflection and the slope is the first derivative. This means that derivative operation contributes to the detection of singularity for the signal uncontaminated by noise. Therefore, as for the signal without noise, if the wavelet transform of the curvature or the slope is conducted, the singularity near the crack will be more distinct and easier to detect. However, noise has an adverse effect on the derivative operation so that such operation can enormously mask the singularity (Gentile and Messina, 2003). To compromise the pros and cons of derivative operations for singularity identification, it is feasible and desirable to conduct the CWT of the slope of either the deflection (static analysis) or the mode shape (dynamic analysis). Additionally, Tu et al. (2005) claimed that singularity can be detected from the modulus maxima, and the complex wavelets outperform real wavelets when the signal is contaminated by noise.

The existing methods of crack detection concentrate on the wavelet transform of the mode shape. In this article, two ideas are introduced into the new method: proposing the slope of the mode shape to detect cracks, and introducing complex continuous wavelet transform (Complex CWT) into crack detection. Especially, it is proposed to detect crack from the angle characteristics of complex wavelet coefficients. This method is easier to detect the exact locations of singularities, compared with the CWT of the mode shape. Also, this new method proves effective when it is used to detect singularity contaminated with noise. All results show that the proposed method has potential in detection of cracks in beams.

2 CRACK MODEL

Three damage models were widely used including the lumped crack model, the continuous crack model, and the smeared crack model (Pakrashi et al., 2007). To

date, some researchers have focused on how to simulate the performance of crack in beams using the lumped crack model (Rizos and Aspragathos, 1990; Ostachowicz and Krawczuk, 1991; Narkis, 1994). In the lumped model (Dimarogonas and Paipetis, 1983; Liang et al., 1992), the crack is simulated by a rotational spring of stiffness K_r, which is a function of d/h, where d is the depth of the crack and h is the height of the beam. A greater value of d/h results in a lower value of K_r. The beam is divided into two separate parts by per crack. The mode shapes of the two segments (Liang et al., 1992), left and right of the crack, respectively, are

$$u_1 = A_1 \cosh\lambda\beta + A_2 \sinh\lambda\beta + A_3 \cos\lambda\beta + A_4 \sin\lambda\beta \tag{1}$$

$$u_2 = B_1 \cosh\lambda\beta + B_2 \sinh\lambda\beta + B_3 \cos\lambda\beta + B_4 \sin\lambda\beta \tag{2}$$

where A_i and B_i, i =1, 2, 3, 4, are constants to be determined from the boundary conditions, λ^2 is the nondimensional natural frequency. $\beta = x/L$, where x is the coordinate along the beam, with the origin at the left end, and L is the length of the beam.

At the crack $\beta = R$,

$$u_1 = u_2|_{\beta=R},\ u_1'' = u_2''|_{\beta=R},\ u_1''' = u_2'''|_{\beta=R},\ u_1' + \left(\frac{EI}{K_r}\right) u_1'' = u_2'|_{\beta=R} \tag{3}$$

where the slopes of the two beam segments, respectively, are

$$u_1' = \lambda\,(A_1 \sinh\lambda\beta + A_2 \cosh\lambda\beta - A_3 \sin\lambda\beta + A_4 \cos\lambda\beta) \tag{4}$$

$$u_2' = \lambda\,(B_1 \sinh\lambda\beta + B_2 \cosh\lambda\beta - B_3 \sin\lambda\beta + B_4 \cos\lambda\beta) \tag{5}$$

Thus, if we find the discontinuity of the slope of the mode shape shown in Equation (3) (Pakrashi et al., 2007), we can identify the location of crack in the beam.

From the boundary conditions and the continuity condition at the crack, we can obtain the eigenequation; and furthermore, the frequency (eigenvalue) and corresponding mode shape (eigenvector) of this cracked beam are obtained since the determinant of the coefficients in eigenequation should be zero. Liang et al. (1992) derived the mode shape of a simply supported beam with one crack and that of a cantilever beam with one crack. In this article, the same method is used to calculate the mode shape of beams with two or three cracks with MATLAB. In fact, with every additional crack or one more span, the eigenequation will have four more constants (like A_i or B_i) to be determined. For example, in the numerical simulation of a three-span continuous beam with three cracks, the mode shape is divided into u_1, u_2, u_3, u_4, u_5, and u_6, because there are three cracks and two interior support points. Thus, there are 24 constants to be determined to calculate the mode shapes and their corresponding slopes.

3 SINGULARITY DETECTION BASED ON WAVELET TRANSFORM

To create a family of wavelet, a complex-valued function, $\psi(x)$, that is localized in both time and frequency domains is used

$$\psi_{a,b}(x) = \frac{1}{\sqrt{|a|}}\psi\left(\frac{x-b}{a}\right) \tag{6}$$

where a is the scale parameter and b is the translation parameter indicating the position. The CWT is a valuable time-frequency analysis tool to detect singularity effectively. For the square-integrable signal $f(x)$, the CWT Wf is defined as

$$Wf(a,b) = \frac{1}{\sqrt{|a|}}\int_{-\infty}^{+\infty} f(x)\psi^*\left(\frac{x-b}{a}\right)dx \tag{7}$$

where ψ^* denotes the complex conjugate.

When wavelet transform is used for identification of singularities (Mallat and Hwang, 1992), it is very important to choose the appropriate vanishing moments. Gaussian wavelet (Gaus) is pth derivatives of the Gaussian function $f(x) = C_p e^{-x^2}$, whereas Complex Gaussian wavelet (CGau) is developed from the complex Gaussian function $f(x) = C_p e^{-ix} e^{-x^2}$ by taking the pth derivative. Both Gaus$p$ and CGau$p$ have p vanishing moments. When p is odd, the real part of CGau$p$ is antisymmetric whereas the imaginary part is symmetric; however, when p is even, the real part is symmetric whereas the imaginary part is antisymmetric. Unlike CWT with real wavelets, the wavelet coefficients of Complex CWT include two parts: modulus and angle. Because of the symmetric characteristic of CGau wavelet, at the position of singularity, the real/imaginary part of the wavelet coefficient arrives at a peak whereas the imaginary/real part vacillates locally and has a zero-crossing at the same position, contributing to a great value of angle of the wavelet coefficient.

When the signal is continuous but its derivatives discontinuous, the least vanishing moments should be two so that the singularity can be detected via wavelet transform. Thus, when the signal is the mode shape of the cracked beam, the least vanishing moments (the vanishing moments of Gaus2 is 2) should be two; when the signal is the slope, the least vanishing moments (the vanishing moments of both Gaus1 and CGau1 are 1) should be one. Mallat and Hwang (1992) discussed how

to use wavelet transform modulus maxima to detect singularity of a signal and how to measure such singularity with Lipschitz index. Tu et al. (2005) extended this method and demonstrated that the modulus maxima of a complex-valued wavelet can also detect and characterize singularity, and it outperformed real wavelet when a signal was embedded in an additive white Gaussian noise environment. Considering the robustness and convenience of detecting singularity, the CGau wavelet family is employed in this article and the singularity can be identified from the characteristic of wavelet coefficients of Complex CWT, especially from the angle.

4 CRACK DETECTION IN A SIMPLY SUPPORTED BEAM

To validate the method of crack detection based on the slope of mode shape using Complex CWT, a simply supported beam with two cracks is analyzed in this section. Both the mode shapes (Mode 1 and Mode 2) and the corresponding slopes (Slope 1 and Slope 2), as shown in Figure 1, are obtained using the mentioned method. The depth, width, and length of the beam are taken as 0.04 m, 0.02 m, and 1 m, respectively. The Young's modulus and the density of the beam are assumed to be 190×10^9 N/m^2 and 7850 kg/m^3, respectively. There are two nonpropagating transverse cracks in the beam. One crack (d/h =0.2) is located at $x = 100$ mm and the other (d/h =0.4) at $x = 400$ mm. The nondimensional natural frequencies corresponding to the first and the second mode shape (λ_1^2 and λ_2^2) change from 3.14159 (π) and 6.28318 (2π) to 3.12146 and 6.25581 due to cracks, which means the crack has slight influence on the frequency. Accordingly, the mode shapes are basically the same despite the cracks; therefore, it is hard to identify the locations of the two cracks from the mode shape directly.

In Figure 2, the first two mode shapes (Mode 1 and Mode 2) have been analyzed according to the traditional crack identification method using CWT (Gentile and Messina, 2003; Chang and Chen, 2003). Since the singularities of such signals are due to the discontinuity of the slope (the first derivative) of the mode shapes at the locations of cracks, Gaus2 wavelet whose vanishing moment is two has been chosen for analysis so that there are peaks at the positions of cracks in the C*a,b* (wavelet coefficients of CWT) line. From the gray maps of C*a,b* for scale a from 1 to 30, in Mode 1 only one singularity is evident at $x = 400$ mm, whereas in Mode 2 there are two singularities whose locations are correspondent to two cracks at $x = 100$ mm and $x = 400$ mm in the beam. In the C*a,b* line for scale $a = 6$, there are two peaks at the positions of cracks. It is noted that it is easier to find the singularity information of cracks from the C*a,b* line of the second mode shape (Mode 2) than that of the first mode shape (Mode 1). The singularity of the crack that is $x = 100$ mm is not apparent in Mode 1, whereas both of the two peaks indicating cracks are evident in Mode 2. In fact, the difference of the amplitude of the two peaks is resulted from the different levels of the slope discontinuity at the cracks. For Mode 1, the discontinuity of the slope at the second crack (x = 400 mm) is greater than that at the first crack (x = 100 mm) as shown in Slope 1 in Figure 1, leading to a greater peak amplitude in C*a,b* line at the second crack as shown in Figure 2. In Slope 2, these two discontinuities at the two cracks are almost the same, leading to the same amplitude in C*a,b* line.

The Complex CWT results of Slope 1 and Slope 2 using CGau1 are shown in Figure 3. Not only from the modulus, but also from the angle can we find the locations of the two cracks. In the four gray maps in Figure 3, the singularities are more apparent in Slope 2 than in Slope 1, and the singularities are more evident in angle than in modulus. In the gray map of angle of Slope 2, at $x = 100$ mm and $x = 400$ mm, there are two bold lines that indicate the locations of the two cracks. By comparison with the CWT using Gaus2 as shown in Figure 2, the modulus of the wavelet coefficients based on Complex CWT with CGau1 is similar, whereas the value of coefficients are much greater although these coefficients are on the same scale $a = 6$. This advantage contributes to localize cracks much easier. In the angle line, only the zero-crossing point or the peak means the singularity. In the angle line of Slope 1, at $x = 100$ mm and $x = 400$ mm there are two zero-crossing points indicating the two cracks. In the angle line of Slope 2, the two distinct peaks at $x = 100$ mm and $x = 400$ mm indicate the locations of the two cracks, whereas the two sudden jumps at $x = 250$ mm and $x = 500$ mm do not mean the singularities. In fact, such two jumps also help us to judge whether there is a crack. In the modulus line for Slope 2, as shown in the fourth subfigure in Figure 3, there are two main waves (Wave1 from $x = 0$ mm to $x = 500$ mm, Wave2 from $x = 500$ mm to $x = 1{,}000$ mm) and the joint is at $x = 500$ mm. Accordingly, there is a corresponding jump from –3 to 0 at this joint location in the angle line for Slope 2, as shown in the last subfigure in Figure 3. There is the other jump from 3 to –3 at x = 250 mm, where the wave crest of Wave1 is in the corresponding modulus line (modulus line for Slope 2), indicating that there are cracks in Wave1 from $x = 0$ to x = 500 mm. No such jump appears in Wave2 from $x = 500$ mm to $x = 1{,}000$ mm, indicating no crack in Wave2. In fact, we can ignore such jumps to judge whether there is a crack in a beam segment, because only a typical evident peak in the angle line means a crack in the beam. By comparison, the singularity from the angle

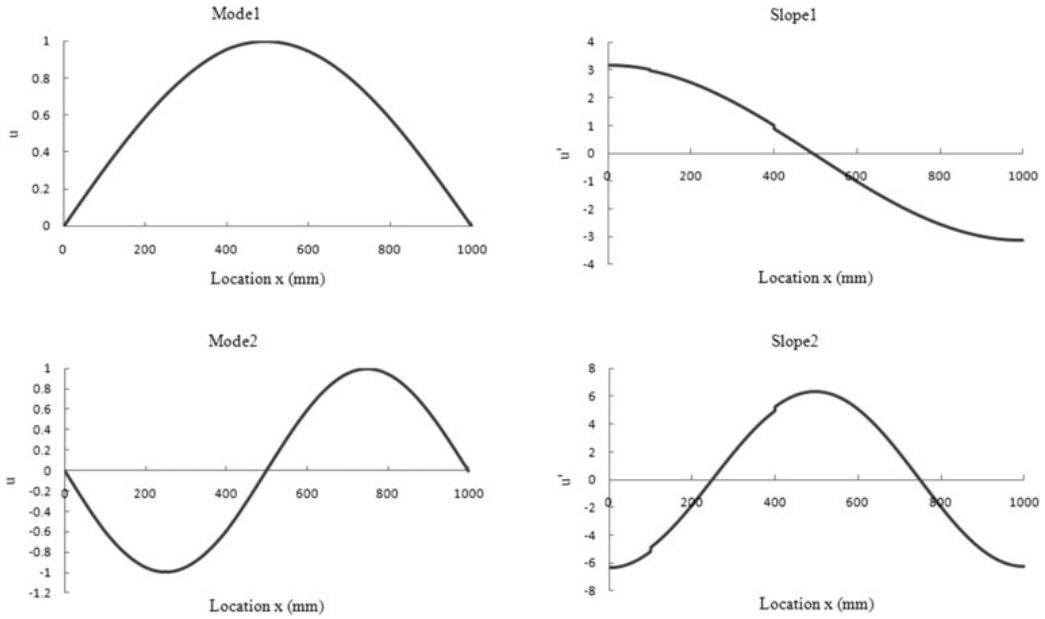

Fig. 1. The first two mode shapes (Mode 1 and Mode 2) and their corresponding slopes (Slope 1 and Slope 2) of the simply supported beam.

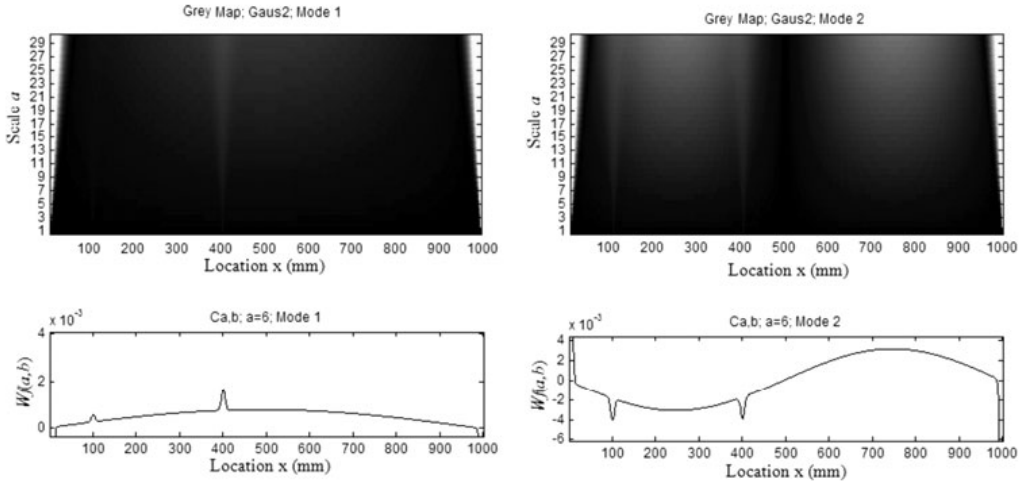

Fig. 2. CWT of the first two mode shapes using Gaus2.

coefficients of the slope is the most apparent to detect crack in beams, because the height of the peak in the angle line is much greater than that in the $C_{a,b}$ line or the modulus line. Also, it is shown in this example that although singularity can be detected from the angle line for Slope 1 and that for Slope 2, the latter is preferable.

5 CRACK DETECTION IN A CANTILEVER BEAM

Through the analysis of a cracked simply supported beam, the method based on the Complex CWT of the slope of the mode shape proves more effective. In this

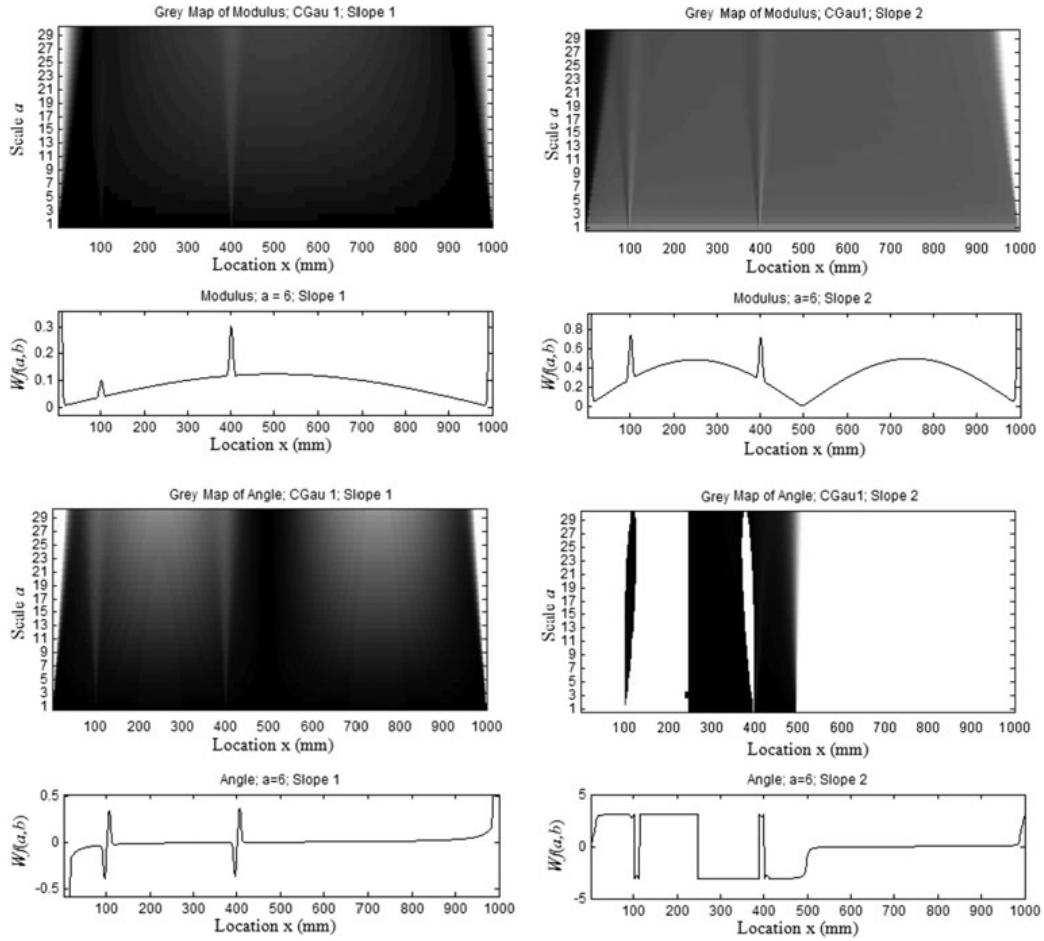

Fig. 3. Complex CWT of the slopes of the first two mode shapes using CGau1.

section, a cantilever beam with two cracks is analyzed. This beam is the same (the same size, the same material property, and the same cracks) as the simply supported beam, only with the different boundary condition (the left end of the beam is fixed whereas the right is free). The fundamental mode shape and its corresponding slope are shown in Figure 4. The wavelet coefficients for scale $a = 5$ and $a = 9$ are calculated based on CWT of the mode shape using Gaus2 (Ca,b; Gaus2; Mode), CWT of the slope using Gaus1 (Ca,b; Gaus1; Slope) and Complex CWT of the slope using CGau1 (modulus; angle; CGau1; Slope), respectively. In Figure 5, the left eight subfigures show the whole coefficients lines whereas the right eight subfigures show the pruned coefficients lines. In the whole coefficients lines, it shows that the extremely large value of coefficients at the boundary make it difficult or even impossible to judge whether the beam is cracked and detect the locations of cracks from Ca,b of CWT or modulus of Complex CWT. To see the detailed information of coefficients, these boundaries are eliminated in the pruned coefficients lines (the boundaries have been eliminated in Figures 2 and 3). In the pruned coefficients lines, two peaks at $x = 100$ mm and $x = 400$ mm indicate the locations of the cracks. The peaks for a higher scale ($a = 9$) are wider than that for a lower scale ($a = 5$), and the coefficients for a higher scale ($a = 9$) are greater than that for a lower scale ($a = 5$). By comparison, the coefficient of the slope at the crack is much greater than that of the mode, which demonstrates the wavelet transform of the slope outperforms that of the mode shape.

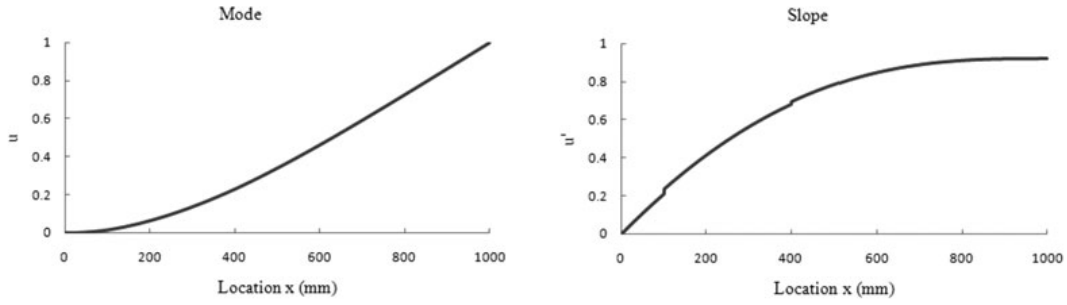

Fig. 4. The mode shape and its corresponding slope of the cantilever beam.

In the angle lines using CGau1, there is boundary effect, too. But, it is easy to find the two distinct peaks at cracks, unnecessary to eliminate the boundary. The peak jumps from –3 to 3 and then back to –3 sharply again. Finding such typical peaks means identifying cracks. This makes crack detection much easier. Compared with CWT, the characteristic of the modulus lines of Complex CWT is similar to that of $C_{a,b}$ lines of CWT, whereas the angle indicates singularities more evidently, which demonstrates the great advantage of Complex CWT. In other words, boundary effect masks the singularity in $C_{a,b}$ of CWT or in the modulus of Complex CWT whereas boundary effect does not mask the singularity in the angle of Complex CWT. It is not necessary to eliminate the boundaries when we detect cracks from the angle lines.

6 WINDOWING BY HANNING AS A REMEDY OF BOUNDARY EFFECT

As previously stated, the boundary effect is detrimental to crack detection. In this article, Hanning window is used to obtain the weighted signal as demonstrated by Gentile and Messina (2003). In Figure 6, it shows the wavelet coefficients lines of the Mode and Slope of the cracked cantilever beam windowing by Hanning. In the $C_{a,b}$ lines of Mode using Gaus2 for $a = 5$, there is only one very small peak at $x = 400$ mm indicating the second crack, whereas it is difficult to find any peak in the $C_{a,b}$ lines of Mode for $a = 9$. In the $C_{a,b}$ lines of Slope using Gaus1 for both $a = 5$ and $a = 9$, there is only one very small peak at $x = 400$ mm indicating the second crack. This demonstrates CWT cannot detect all cracks although the coefficient at the boundary becomes zero after windowing by Hanning. In the modulus lines of Slope using CGau1 for both $a = 5$ and $a = 9$, there is a very small peak at $x = 100$ mm and a distinct peak at $x = 400$ mm indicating the two cracks. However, it is very easy to detect all cracks from the angle coefficients. In the angle lines of Slope using CGau1, the two peaks are very apparent at $x = 100$ mm and $x = 400$ mm. As stated in the example of the simply supported beam, the jumps can be explained in the same way. The jump from –3 to 0 in the angle line is located at $x = 540$ mm, where the joint of the two waves is in the corresponding modulus line. The huge jump from 3 to –3 is at $x = 320$ mm where the wave crest is in the corresponding modulus line, indicating there are cracks in this wave from $x = 0$ mm to $x = 540$ mm. Therefore, through windowing by Hanning, it is also easier to detect cracks from the peaks in the angle line based on Complex CWT of the slope of the mode shape.

7 INFLUENCE OF CRACK LOCATION AND DEPTH ON CRACK DETECTION

A series of cracked cantilever beams with the same size and material properties as the previous example are studied. There are also two cracks C1 (d/h =0.2) and C2 (d/h =0.4). C2 is always located at $x = 400$ mm whereas the location of C1 (x-C1) varies from 50 mm to 900 mm. Generally, the wavelet coefficient increases with the crack depth which indicates the extent of singularity. However, crack locations influence crack detection greatly because different crack locations result in the different levels of the slope discontinuity. The three left subfigures in Figure 7 show the $C_{a,b}$ lines of the Mode using Gaus2 for scale $a = 5$ when the location of C1 is 100 mm, 500 mm, and 700 mm, respectively. When x-C1 = 100 mm, the peak at $x = 100$ mm is larger than the peak at C2 ($x = 400$ mm) although the crack C2 is deeper than C1. When C1 and C2 are close enough (x-C1 = 500 mm), causing the crack location effect negligible, the peak at the deeper crack (C2) is larger than that of the smaller crack. When x-C1 = 700 mm, the peak at C2 is very distinct, although it is difficult to find

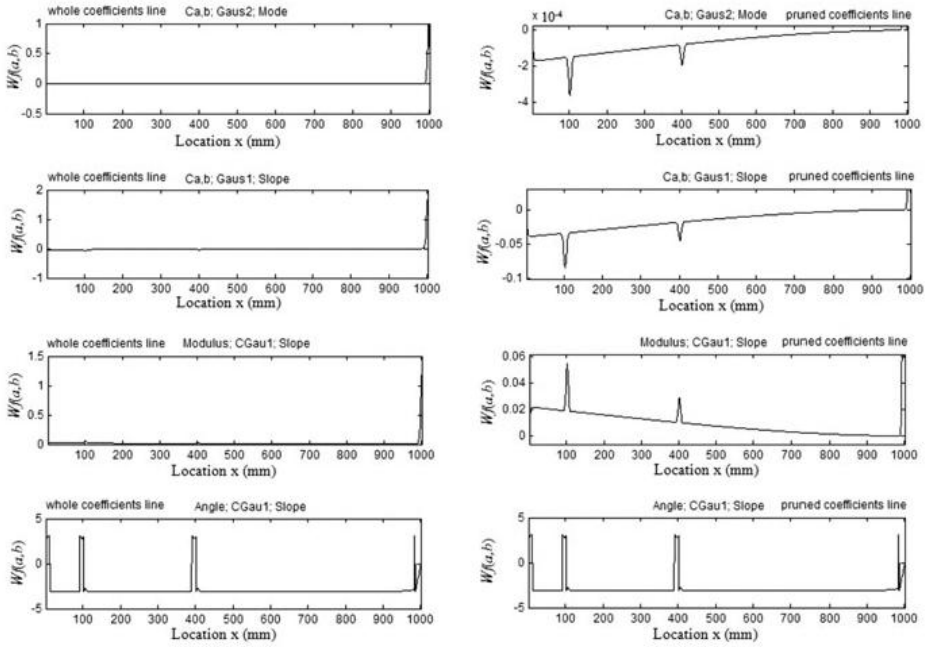

a) Scale a=5

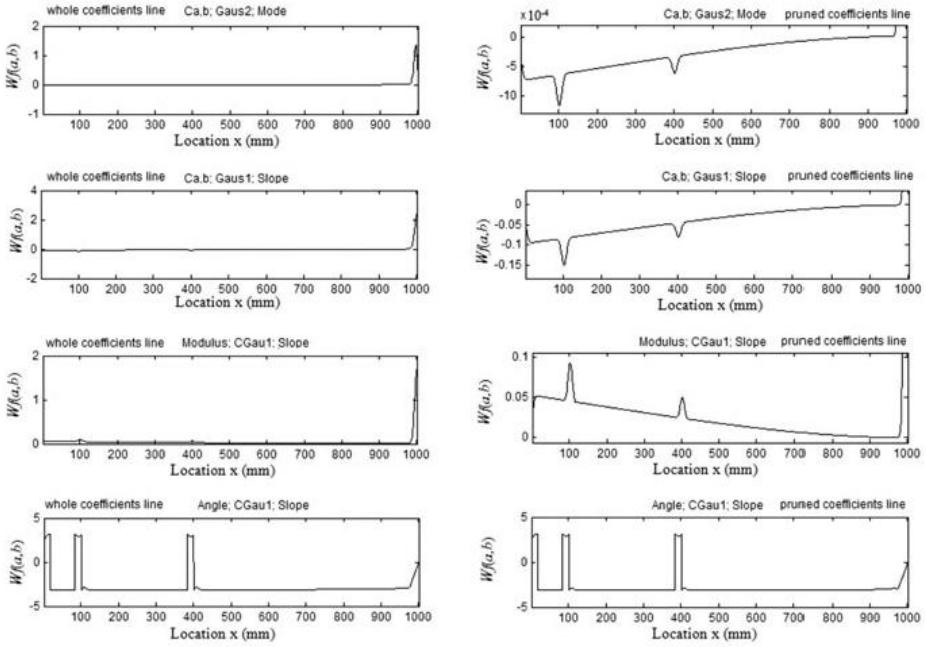

b) Scale a=9

Fig. 5. Wavelet coefficients lines of the cantilever beam, for scale $a = 5$ and $a = 9$.

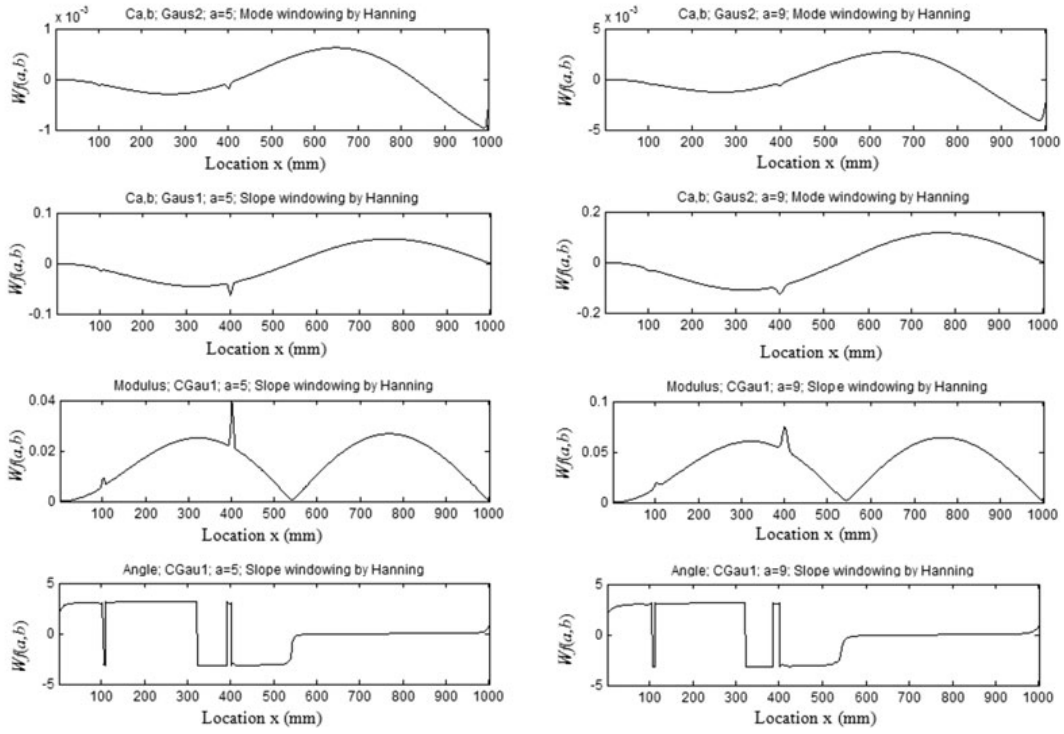

Fig. 6. Wavelet coefficients lines windowing by Hanning, for scale $a = 5$ and $a = 9$.

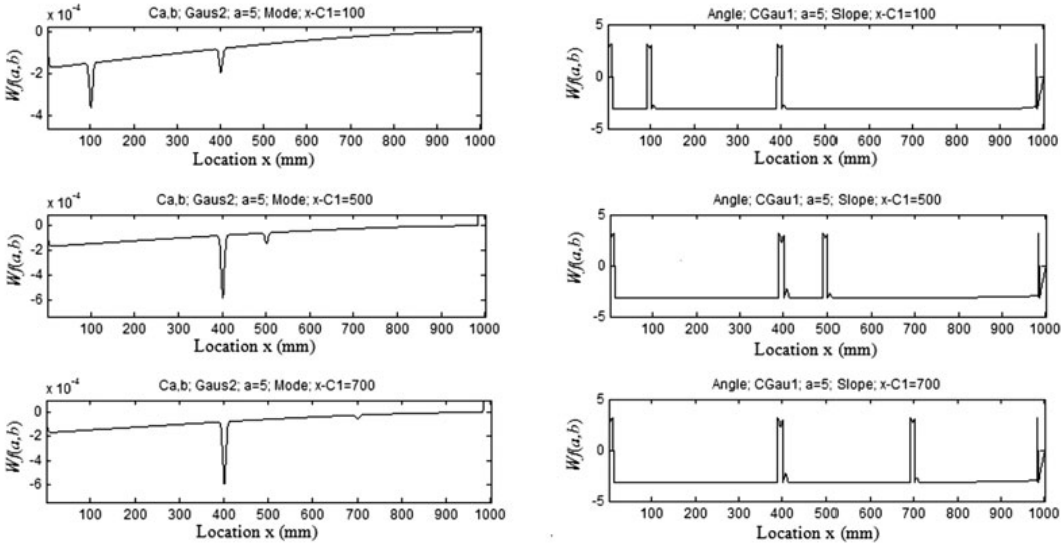

Fig. 7. Wavelet coefficients lines of the cantilever beam with different crack locations, for scale $a = 5$.

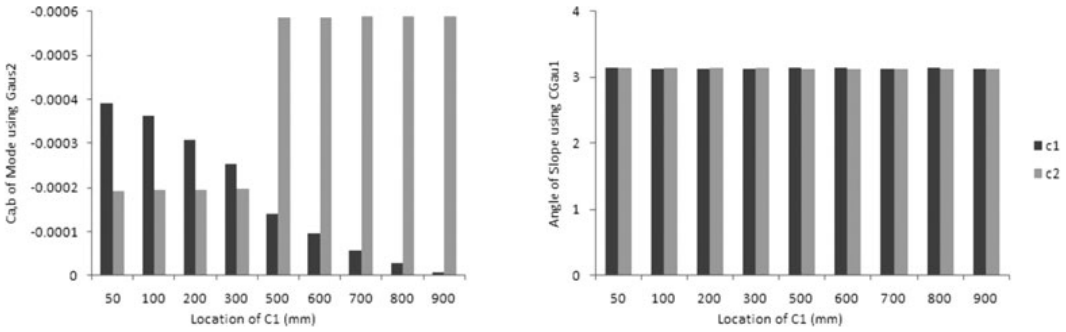

Fig. 8. The influence of crack locations on the wavelet coefficient at the crack, for scale $a = 5$.

the peak at C1. This shows that the singularity increases when the crack is close to the fixed end. However, in the angle lines shown in the three right subfigures in Figure 7, the height of the two peaks are almost the same; therefore, it helps to detect all cracks in the beam without missing any. In Figure 8, it shows how Ca,b and angle change with the location of cracks. When C1 is located in the left side of C2 (i.e., the location of C1 is less than 400 mm), Ca,b at C1 decreases with increasing x-C1 while Ca,b at C2 almost stays the same, and Ca,b of C1 is greater than Ca,b of C2 although C2 is deeper than C1. When C1 is located in the right side of C2 (i.e., the location of C1 is more than 400 mm), Ca,b at C1 still decreases with increasing x-C1, while Ca,b at C2 stays the same at a very high value. When x-C1 is more than 700 mm, the extremely small ratio of Ca,b at C1 to Ca,b at C2 masks singularity of C1 significantly, thereby making it impossible to detect the crack C1. However, the angle coefficient of both C1 and C2 are almost the same, and it does not change evidently with the location of cracks. It means that crack locations and depth have little influence on the angle coefficients. Finding all peaks in the angle lines means detecting all cracks in the beam.

To further demonstrate the influence of crack location and depth on wavelet coefficient, two cases of a cantilever beam are studied as shown in Figure 9. In Case 1, the two cracks are very close, but with different depths. The relative depth (d/h) of the crack at $x1 = 400$ mm is 0.1, whereas d/h of the other crack at $x2 = 450$ mm is 0.6. In the Ca,b line of CWT of Mode, only the deeper crack can be detected. But, in the angle line of Complex CWT of Slope, both cracks can be detected. In Case 2, the smaller crack ($d/h = 0.1$) is close to the fixed end ($x1 = 50$ mm), whereas the deeper crack ($d/h = 0.6$) is close to the free end ($x2 = 950$ mm). In the Ca,b line of CWT of Mode, only the smaller crack close to the fixed end is detected and the deeper crack cannot be detected, although the depth of the crack located at $x2 = 950$ mm is much greater than that of the other crack. But, in the angle line of Complex CWT of Slope, both cracks are detected from the two peaks. Therefore, although the influence of crack depth and locations may result in incapability of detecting all cracks from CWT of the mode shape, the singularities in the angle coefficients show all locations of cracks in the beam.

8 CRACK DETECTION IN A MULTISPAN CONTINUOUS BEAM

Crack detection from the slope of the mode shape using Complex CWT can be also applied in a multispan continuous beam. A three-span continuous beam with three cracks is analyzed in this section. The size of the cross section and the material properties are the same as those in the previously analyzed simply supported beam. The total length of the beam is 2,000 mm. Two interior supporting points are located at 600 mm and 1,400 mm, respectively. The locations of the three cracks are at 640 mm, 1,700 mm, and 1,960 mm, respectively. The depths of the three cracks are the same and $d/h = 0.1$. As shown in Figure 10, both the mode shape and the corresponding slope are obtained. Results of wavelet transform for $a = 5$ and $a = 9$ are shown in Figure 11. In the top two subfigures in Figure 11, it is difficult to detect the crack at $x = 640$ mm and no peak appears at $x = 1{,}960$ mm, based on Ca,b lines of Mode using Gaus2. In the modulus of coefficients lines of Slope using CGau1, the crack at $x = 640$ mm and the crack at $x = 1{,}700$ mm are detected for $a = 5$. In the angle line shown in Figure 11, there are three apparent peaks indicating the locations of three cracks. As previously discussed, the jumps (at $x = 680$ mm and $x = 1{,}320$ mm) appear at the wave joints in the modulus line. The whole beam is divided into three segments by these two jumps. The greater jumps (at $x = 400$ mm and $x = 1{,}600$ mm) are located at the crests of the two waves,

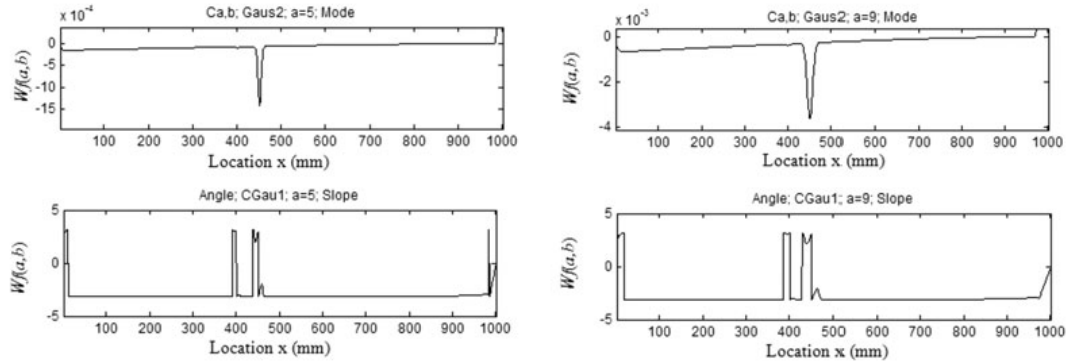

a) Case 1: two cracks locations x1=400mm and x2=450mm

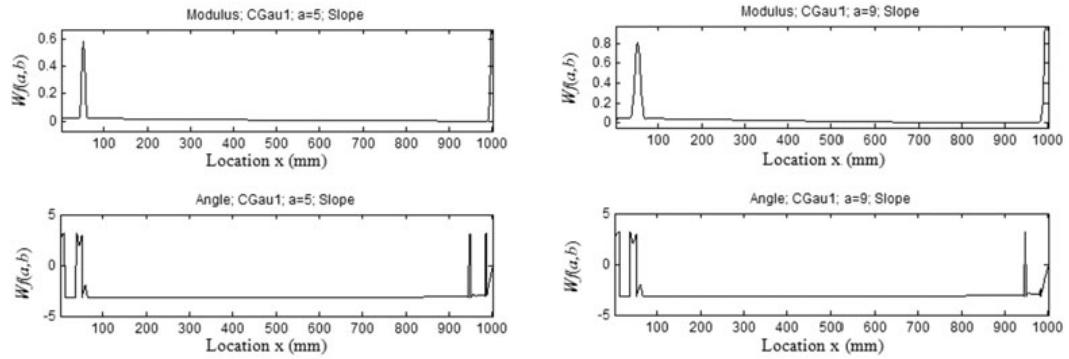

b) Case 2: two cracks locations x1=50mm and x2=950mm

Fig. 9. Wavelet coefficients lines of the two cases of the cantilever beam, for scale $a = 5$ and $a = 9$.

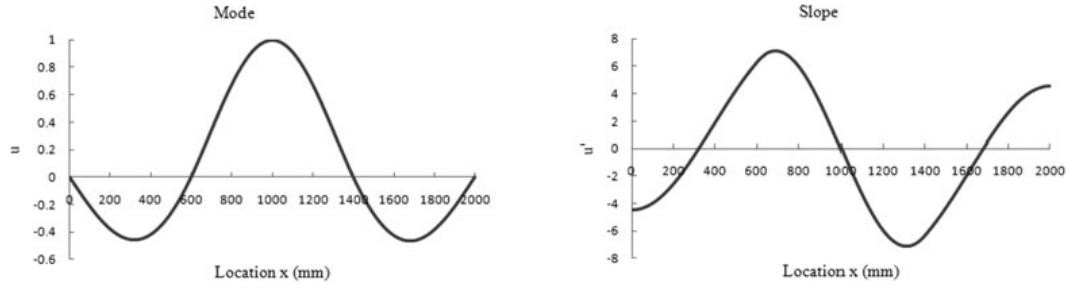

Fig. 10. The mode shape and its corresponding slope of the three-span continuous beam.

indicating that there are cracks in the corresponding beam segments.

9 EFFECT OF NOISE ON WAVELET ANALYSIS

In this section, the second mode shape of the cracked simply supported beam (Slope 2 in Figure 1) is used as the uncontaminated signal to analyze. The number of sampling points is set $N = 1{,}001$ along the beam. In the following simulations the mode shape is added with a Gaussian white noise such that the SNR varies from 50 db to 75 db. The SNR is defined as SNR $= 20\log_{10}(Y_s/Y_n)$db, where Y_s is the standard deviation of the signal and Y_n is the standard deviation of white noise. The slope of the contaminated signal can be

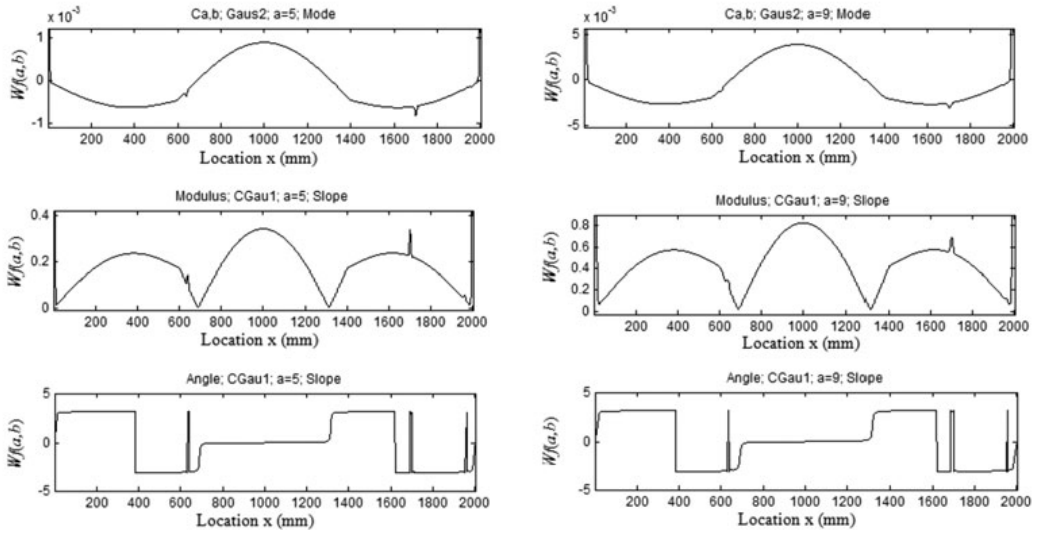

Fig. 11. Wavelet coefficients lines of the continuous beam, for scale $a = 5$ and $a = 9$.

obtained as the first derivative of this signal with the difference method. On the one hand, the derivative of the uncontaminated signal (the slope of the mode shape herein) can reflect the singularity more clearly; on the other hand, derivative operations of the signal with noise normally magnify the adverse effect of noise to some extent so that the singularity may be masked (Gentile and Messina, 2003).

As demonstrated by Mallat and Hwang (1992), the signal is often dominated by the noise on the low scale, but the signal may dominate the noise on higher scales for a given SNR. If the signal localizes singularities of a larger value than the noise, the modulus maxima of the signal on high scales can be discriminated from that of noise, and their amplitude increases slightly when the scale decreases. To demonstrate the advantage and effectiveness of the proposed method applied to signal with noise, a multiscale wavelet analysis of the signal with SNR = 65 db is shown in Figure 12. Although CWT of the mode shape using Gaus2 can detect cracks at $x = 100$ mm and $x = 400$ mm as shown in Figure 2 when the signal is not contaminated by noise, no singularities appear at the locations of cracks as shown in the left four subfigures in Figure 12 when SNR of the signal is 65 db. The right four subfigures in Figure 12 show the results of Complex CWT of the slope of the contaminated mode shape with SNR = 65 db. In the gray map of angle using CGau1, there are two main bold lines along the scales: one is black at $x = 100$ mm and the other is white at $x = 400$ mm. There are also discontinuous fine lines between $x = 200$ mm and $x = 300$ mm. Such fine lines created by noise become narrower and narrower with increasing scales and finally disappear at a high scale $a = 26$. We can also see this phenomenon from the angle lines for multiscale. For scale $a = 20$, there are two typical peaks (almost the same shapes of peaks for the uncontaminated signal in Figure 3) at $x = 100$ mm and $x = 400$ mm whereas there are many narrow peaks between $x = 200$ mm and $x = 300$ mm. For scale $a = 23$, the same two peaks as shown in scale $a = 20$ still exist at the same locations, whereas the width or location of narrow peaks are different from those for scale $a = 20$. For scale $a = 26$, only two typical peaks appear at the locations of cracks and the effect of noise is negligible.

The influence of different SNR is also analyzed in Figure 13. Although the difference of SNR of the mode shape is insignificant (one is 75 db and the other is 50 db), their slopes are substantially different. This is ascribed to the notorious adverse effect of derivative operation, which considerably magnifies noise to mask the signal. In the gray map of angle when SNR = 75 db, the two bold lines in the color map clearly indicate the locations of the cracks. Compared with the gray map of angle in Figure 12 in which SNR = 65 db, these two bold lines are more noticeable, and there are much less fine lines created by noise. It means that the greater SNR is, the clearer the singularity is. In this example, when SNR is less than 50 db, the noise influence is dominant and the singularity of the cracks is masked.

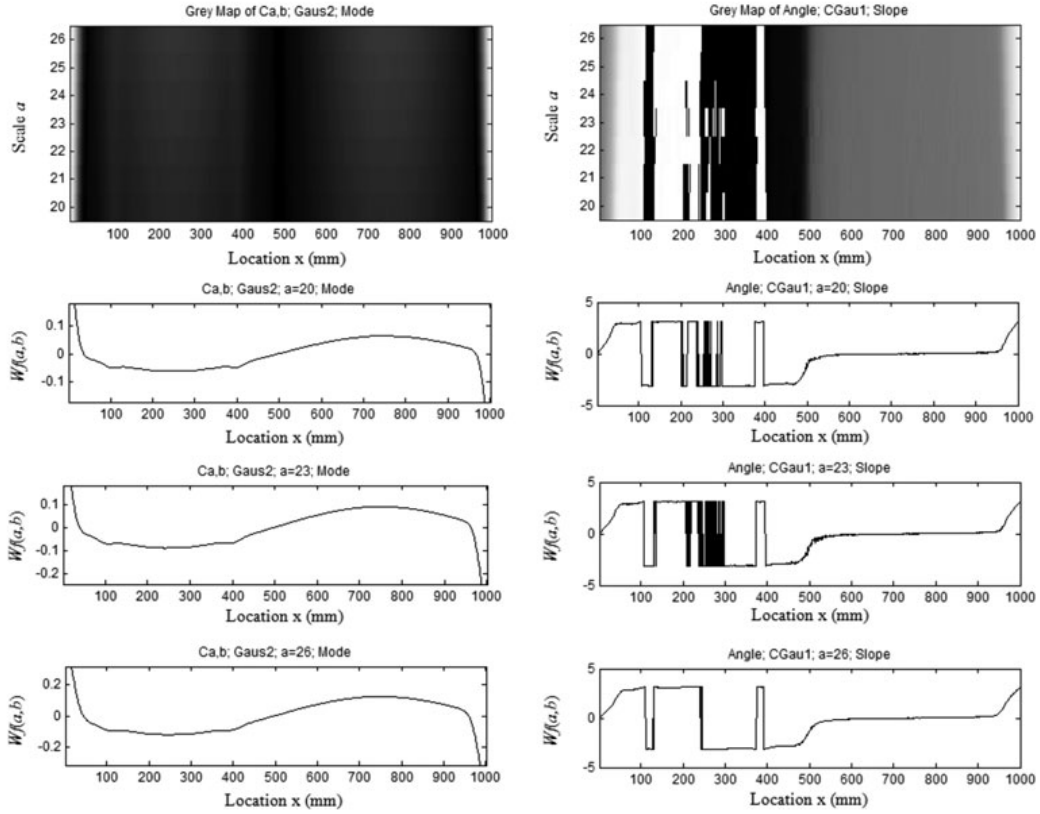

Fig. 12. Comparison of CWT of the second mode shape with SNR = 65 db and Complex CWT of the corresponding slope.

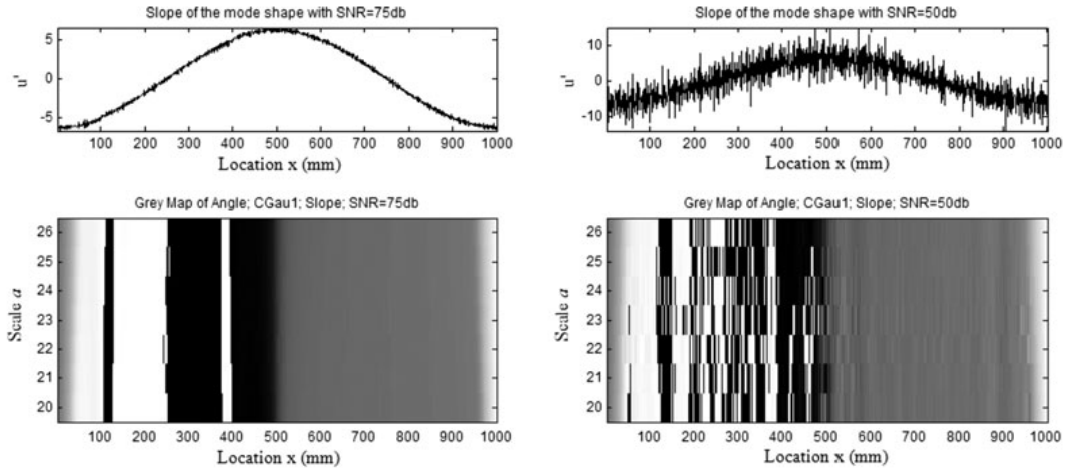

Fig. 13. Complex CWT for the slopes of the second mode shape with SNR = 75 db and SNR = 50 db.

10 CONCLUSIONS

In this article, a method based on Complex CWT has been presented for crack identification in beam members. A series of cracked beams with different boundary conditions are analyzed. Both the mode shape and its slope are calculated. Although it is difficult to detect the local perturbations due to cracks directly, they are visible through wavelet transform. The main conclusions drawn from this study are as follows.

1. The proposed method based on Complex CWT proves effective in detection of cracks in beams. Compared with CWT, the singularity is much more apparent in the angle line of Complex CWT, even when the signal is contaminated by noise.
2. The wavelet analysis of both the mode shape and its slope can be used to detect the location of the crack. By comparison, the singularity of the slope is more obvious. Therefore, it is recommended to use Complex CWT of the slope to identify the crack.
3. The location of the crack can be detected from the characteristic of wavelet coefficients lines through multiscale analysis. At the crack location, there is a peak or a zero-crossing in the modulus line or the angle line of Complex CWT of the slope. Especially, it is much easier to detect crack from apparent singularity in the angle line. This method can be used to detect cracks in a variety of beams.
4. The fundamental mode shape and its corresponding slope may not be the best signal to detect the crack. In this research, the second mode shape and its corresponding slope are preferable when detecting cracks in the simply supported beam.
5. Boundary conditions, crack locations, and crack depth have great influence on the coefficients of CWT using real wavelets, even making it impossible to detect all cracks. However, with the method of Complex CWT of the slope of the mode shape, all cracks can be detected from the angle line easily.
6. When the signal is contaminated by noise, the proposed method of Complex CWT of the slope outperforms the method of CWT of the mode shape. Through the multiscale analysis, cracks can be detected on high scales.

ACKNOWLEDGMENTS

The research is supported by China Scholarship Council (CSC) and the Department of Civil and Environmental Engineering of University of Tennessee, Knoxville, which are gratefully acknowledged. The authors are also grateful to Dr. Deqing Guan of Changsha University of Science and Technology for the presented work.

REFERENCES

Adeli, H. & Jiang, X. (2006), Dynamic fuzzy wavelet neural network model for structural system identification, *Journal of Structural Engineering, ASCE*, **132**(1), 102–11.

Adeli, H. & Karim, A. (2000), A fuzzy-wavelet RBF neural network model for freeway incident detection, *Journal of Transportation Engineering, ASCE*, **126**(6), 464–71.

Adeli, H. & Samant, A. (2000), An adaptive conjugate gradient neural network: wavelet model for traffic incident detection, *Computer-Aided Civil and Infrastructure Engineering*, **13**(4), 251–60.

Al-Khalidy, A., Noori, M., Hou, Z., Yamamoto, S., Masuda, A. & Sone, A. (1997), Health monitoring systems of linear structures using wavelet analysis, in *Proceedings of the International Workshop on Structural Health Monitoring: Current Status and Perspectives*, Stanford, CA, 18–20, September 1997, 164–75.

Cao, M. & Qiao, P. (2008), Integrated wavelet transform and its application to vibration mode shapes for the damage detection of beam-type structures, *Smart Materials and Structures*, **17**, 1–17.

Chang, C. C. & Chen, L. W. (2003), Vibration damage detection of a Timoshenko beam by spatial wavelet based approach, *Applied Acoustics*, **64**, 1217–40.

Chasalevris, A. C. & Papadopoulos, C. A. (2006), Identification of multiple cracks in beams under bending, *Mechanical Systems and Signal Processing*, **20**, 1631–73.

Chondros, T. G. & Dimarogonas, A. D. (1980), Identification of cracks in welded joints of complex structures, *Journal of Sound and Vibration*, **69**(4), 531–38.

Daubechies, I. (1992), *Ten Lectures on Wavelets*, SIAM, Philadelphia.

Dimarogonas, A. D. & Paipetis, S. A. (1983), *Analytical Methods in Rotor Dynamics*, Applied Science Publishers, London.

Douka, E., Loutridis, S. & Trochidis, A. (2003) Crack identification in beams using wavelet analysis, *International Journal of Solids and Structures*, **40**, 3557–69.

Gentile, A. & Messina, A. (2003), On the continuous wavelet transforms applied to discrete vibrational data for detecting open cracks in damaged beams, *International Journal of Solids and Structures*, **40**, 295–315.

Ghosh-Dastidar, S. & Adeli, H. (2003), Wavelet-clustering-neural network model for freeway incident detection, *Computer-Aided Civil and Infrastructure Engineering*, **18**(5), 325–38.

Ghosh-Dastidar, S. & Adeli, H. (2006), Neural network-wavelet micro-simulation model for delay and queue length estimation at freeway work zones, *Journal of Transportation Engineering, ASCE*, **132**(4), 331–41.

Han, J. G., Ren, W. X. & Sun, Z. S. (2005), Wavelet packet based damage identification of beam structures, *International Journal of Solids and Structures*, **42**(26), 6610–17.

Hong, J. C., Kim, Y. Y., Lee, H.C. & Lee, Y.W. (2002), Damage detection using the Lipschitz exponent estimated by the wavelet transform: applications to vibration modes of a beam, *International Journal of Solids and Structures*, **39**, 1803–16.

Jafarkhani, R. & Masri, S. F. (2011), Finite element model updating using evolutionary strategy for damage detection, *Computer-Aided Civil and Infrastructure Engineering*, **26**(3), 207–24.

Jiang, X. & Adeli, H. (2004), Wavelet packet-autocorrelation function method for traffic flow pattern analysis, *Computer-Aided Civil and Infrastructure Engineering*, **19**(5), 324–37.

Jiang, X. & Adeli, H. (2005), Dynamic wavelet neural network for nonlinear identification of highrise buildings, *Computer-Aided Civil and Infrastructure Engineering*, **20**(5), 316–30.

Jiang, X. & Adeli, H. (2007), Psuedospectra, MUSIC, and dynamic wavelet neural network for damage detection of high-rise buildings, *International Journal for Numerical Methods in Engineering*, **71**(5), 606–29.

Jiang, X., Mahadevan, S. & Adeli, H. (2007), Bayesian wavelet packet denoising for structural system identification, *Structural Control and Health Monitoring*, **14**(2), 333–56.

Kim, H. & Adeli, H. (2005a), Hybrid control of smart structures using a novel wavelet-based algorithm, *Computer-Aided Civil and Infrastructure Engineering*, **20**(1), 7–22.

Kim, H. & Adeli, H. (2005b), Wind-induced motion control of 76-story benchmark building using the hybrid damper-tuned liquid column damper system, *Journal of Structural Engineering, ASCE*, **131**(12), 1794–802.

Kim, J. T. & Stubbs, N. (2002), Improved damage identification method based on modal information, *Journal of Sound and Vibration*, **252**(2), 223–38.

Liang, R. Y., Hu, J. & Choy, F. (1992), Theoretical study of crack-induced eigenfrequency changes on beam structures, *Journal of Engineering Mechanics*, **118**(2), 384–96.

Liew, K. M. & Wang, Q. (1998), Application of wavelet theory for crack identification in structures, *Journal of Engineering Mechanics*, **124**(2), 152–57.

Mallat, S. (2001), *A Wavelet Tour on Signal Processing*, Academic Press, New York.

Mallat, S. & Hwang, W. (1992), Singularity detection and processing with wavelets, *IEEE Transactions on Information Theory*, **38**(2), 617–43.

Moaveni, B., Conte, J. P. & Hemez, F. M. (2009), Uncertainty and sensitivity analysis of damage identification results obtained using finite element model updating, *Computer-Aided Civil and Infrastructure Engineering*, **24**(5), 320–34.

Narkis, Y. (1994), Identification of crack location in vibrating simply supported beams, *Journal of Sound and Vibration*, **172**(4), 549–58.

Ostachowicz, W. M. & Krawczuk, M. (1991), Analysis of the effect of cracks on the natural frequencies of a cantilever beam, *Journal of Sound and Vibration*, **150**(2), 191–201.

Ovanesova, A. V. & Suarez, L. E. (2004), Applications of wavelet transforms to damage detection in frame structures, *Engineering Structures*, **26**, 39–49.

Pakrashi, V., O'Connor, A. & Basu, B. (2007), A study on the effects of damage models and wavelet bases for damage identification and calibration in beams, *Computer-Aided Civil and Infrastructure Engineering*, **22**(8), 555–69.

Pandey, A. K., Biswas, M. & Samman, M. M. (1991), Damage detection from changes in curvature mode shapes, *Journal of Sound and Vibration*, **145**(2), 321–32.

Quek, S. T., Wang, Q., Zhang, L. & Ang, K. K. (2001), Sensitivity analysis of crack detection in beams by wavelet technique, *International Journal of Mechanical Sciences*, **43**, 2899–910.

Ren, W. X. & De Roeck, G. (2002a), Structural damage identification using modal data. I: simulation verification, *Journal of Structural Engineering, ASCE*, **128**(1), 87–95.

Ren, W. X. & De Roeck, G. (2002b), Structural damage identification using modal data. II: test verification, *Journal of Structural Engineering, ASCE*, **128**(1), 96–104.

Ren, W. X. & Jaishi, B. (2006), Damage detection by finite element model updating using modal flexibility residual, *Journal of Sound and Vibration*, **290**(1–2), 369–87.

Ren, W. X. & Sun, Z. S. (2008), Structural damage identification by using wavelet entropy, *Engineering Structures*, **30**(10), 2840–49.

Ren, W. X., Sun, Z. S., Xia, Y., Hao, H. & Deeks, A. J. (2008), Damage identification of shear connectors with wavelet packet energy: laboratory test study, *Journal of Structural Engineering, ASCE*, **134**(5), 832–41.

Rizos, P. F. & Aspragathos, N. (1990), Identification of crack location and magnitude in a cantilever beam from the vibration modes, *Journal of Sound and Vibration*, **138**(3), 381–88.

Samant, A. & Adeli, H. (2000), Feature extraction for traffic incident detection using wavelet transform and linear discriminant analysis, *Computer-Aided Civil and Infrastructure Engineering*, **13**(4), 241–50.

Samant, A. & Adeli, H. (2001), Enhancing neural network traffic incident-detection algorithms using wavelets, *Computer-Aided Civil and Infrastructure Engineering*, **16**(4), 239–45.

Spanos, P. D., Failla, G., Santini, A. & Pappatico, M. (2006), Damage detection in Euler-Bernoulli beams via spatial wavelet analysis, *Structural Control and Health Monitoring*, **13**, 472–87.

Surace, C. & Ruotolo, R. (1994), Crack detection of a beam using the wavelet transform, in *Proceedings of the 12th International Modal Analysis Conference*, Honolulu, USA, 1141–47.

Tu, C., Hwang, W. & Ho, J. (2005), Analysis of singularities from modulus maxima of complex wavelets, *IEEE Transactions on Information Theory*, **51**(3), 1049–62.

Umesha, P. K., Ravichandran, R. & Sivasubramanian, K. (2009), Crack detection and quantification in beams using wavelets, *Computer-Aided Civil and Infrastructure Engineering*, **24**(8), 593–607.

Xia, Y., Ni, Y. Q., Zhang, P., Liao, W. Y. & Ko, J. M. (2011), Stress development of a super-tall structure during construction: numerical analysis and field monitoring verification, *Computer-Aided Civil and Infrastructure Engineering*, **26**(7), 1–18.

Xu, B., Chen, G. & Wu, Z. (2007), Parametric identification for a truss structure using axial strain, *Computer-Aided Civil and Infrastructure Engineering*, **22**(3), 210–22.

Yin, T., Lam, H. F. & Chow, H. M. (2010), A Bayesian probabilistic approach for crack characterization in plate structures, *Computer-Aided Civil and Infrastructure Engineering*, **25**(5), 375–86.

Yuen, M. M. F. (1985), A numerical study of the eigenparameters of a damaged cantilever, *Journal of Sound and Vibration*, **103**, 301–10.

Zhou, Z. & Adeli, H. (2003a), Time-frequency signal analysis of earthquake records using Mexican hat wavelets, *Computer-Aided Civil and Infrastructure Engineering*, **18**(5), 379–89.

Zhou, Z. & Adeli, H. (2003b), Wavelet energy spectrum for time-frequency localization of earthquake energy, *International Journal of Imaging Systems and Technology*, **13**(2), 133–40.

Effect of Shear Stud Connections on Dynamic Response of an FRP Deck Bridge under Moving Loads

Xin Jiang[1]; Zhongguo John Ma, F.ASCE[2]; and Jing Song[3]

Abstract: The main objective of this study was to evaluate the effect of shear stud connections on the dynamic response of the fiber-reinforced polymer (FRP) deck system under moving loads. A FRP deck bridge in Pennsylvania was studied based on a field test and finite-element (FE) analysis. In the field test, the strain of each steel girder at the midspan was measured at three positions: top, midheight, and bottom. In the FE analysis, the connection between the steel girders and the FRP deck was simulated as fully and partially composite, separately. Static performance under a simplified truck load was investigated based on these two FE models, and the FE analysis results were compared with the field test results to validate the FE models. The FE results of the fully composite model and the partially composite model provide a lower bound and an upper bound for the real response of the FRP deck system. Next, the dynamic behavior of the FRP deck system under moving loads was studied based on the two verified FE models. The static or dynamic response in the partially composite model of the FRP deck bridge was greater than the corresponding static or dynamic response in the fully composite model. Also, it was shown that the dynamic response in the partially composite model lags behind that in the fully composite model. Additionally, the FE analysis revealed that the number of shear stud connections affected the dynamic deflection, slip, and separation. Finally, the dynamic response of the FRP deck system was compared with that of the commonly used RC system. **DOI: 10.1061/(ASCE)BE.1943-5592.0000401.**

CE Database subject headings: Dynamic response; Fiber reinforced polymer; Bridge decks; Girder bridges; Studs; Finite element method; Connections; Moving loads.

Author keywords: Dynamic response; Fiber-reinforced polymer (FRP) deck; Steel I-girders; Shear studs; Finite-element analysis; Composite action.

Introduction

It has been demonstrated that the use of fiber-reinforced polymer (FRP) sandwich panels for bridge deck construction is time-efficient and structurally effective (Ji et al. 2010). They show great potential for integration into the highway infrastructure by applying the prefabricated and easily installed FRP sandwich panels to the accelerated construction and replacement of deteriorated concrete bridge decks. Currently, connections to an existing superstructure are subdivided into those that provide noncomposite bending action and those that provide composite bending action. Traditionally, connections between RC deck and prestressed concrete and/or steel I-girders have been designed to develop a composite bending action (i.e., to transfer the horizontal shear developed between the deck and the support girders). These connections are specified to have strain compatibility and prevent relative movement between the deck and the support girders.

Schollmayer and Keller (2009) assumed deck-to-girder adhesive joints as being loaded by uplift forces only when the thickness of the adhesive layer was not less than 10 mm. An analytical model was proposed that allowed the calculation of a representative approximation of the complex uplift stress state in the joint, and this model was validated by numerical and experimental results. On the other hand, shear stud connections are commonly used in hybrid beams to accomplish the composite action. Slutter and Fisher (1965) proposed design criteria for shear connectors in composite beams. The number of shear connectors satisfied the fatigue criterion and also ensured the ultimate strength of the composite section. It was noted that the number of connectors required by the former criterion usually greatly exceeded the latter. Furthermore, Ollgaard et al. (1971) studied the behavior of stud connectors in lightweight and normal-weight concrete based on a series of pushout tests. The shear strength of studs was determined by the cross-sectional area of the studs, the compressive strength, and the modulus of elasticity of the concrete. Gattesco (1999) analyzed the steel and concrete composite beams based on a numerical procedure, accounting for nonlinear behavior of materials and using an empirical load-slip relationship for shear connectors. Xue et al. (2008) conducted 30 push-out tests to investigate the influence of factors such as stud size, concrete strength, stud welding technique, transverse reinforcement, and steel beam type. The load-slip relationship also was analyzed. Pallares and Hajjar (2009a, b) studied the behavior of headed shear studs embedded in composite beams systematically.

Over the past decade, investigation was conducted to analyze the behavior of shear studs embedded in FRP decks. Moon et al. (2002) evaluated the performance of three different shear studs used for FRP deck-to-girder connections. An expression was proposed to determine the longitudinal capacity for shear stud connections. The bearing strength of the bottom face sheet represented a lower bound, and the shear stud capacity an upper bound. Park et al. (2006)

[1]Graduate Student, Dept. of Civil and Environmental Engineering, Univ. of Tennessee, Knoxville, TN 37996-2010.

[2]Associate Professor, Dept. of Civil and Environmental Engineering, Univ. of Tennessee, Knoxville, TN 37996-2010 (corresponding author). E-mail: zma2@utk.edu

[3]Graduate Student, Dept. of Civil and Environmental Engineering, Univ. of Tennessee, Knoxville, TN 37996-2010.

Note. This manuscript was submitted on November 6, 2011; approved on April 18, 2012; published online on April 20, 2012. Discussion period open until December 1, 2013; separate discussions must be submitted for individual papers. This paper is part of the ***Journal of Bridge Engineering***, Vol. 18, No. 7, July 1, 2013. ©ASCE, ISSN 1084-0702/2013/7-644–652/$25.00.

conducted a static load test to investigate the degree of composite action for a bolted glass FRP (GFRP) bridge deck-to-girder connection system, based on the analysis of neutral axis changes. Davalos et al. (2011) evaluated a nongrouted sleeve-type connection system for FRP bridge decks to steel girders. The neutral axis position for two spacings of connections was analyzed to investigate the composite action.

Because of the section properties of the FRP composite deck, which has relatively thin face skins and discrete webs with nonstructural filler material (foam), the composite action will not provide the same magnitude of additional bending capacity to the support girders as a conventional concrete deck. This traditional connection concept should not be blindly followed in the FRP composite deck-to-girder connection design. In the area of deck replacement, considering the significant decrease of dead load when replacing concrete deck with FRP deck, it is very attractive to relax the requirement on the degree of composite action between the FRP deck and the lower girders to accelerate bridge construction (Li et al. 2010). Because of significant differences in the basic material systems between FRPs and concrete materials, designing interfaces between these materials to ensure consistent mechanical action is much more important in the overall design process. Currently, no specific guidelines or research on the design of the number of the shear studs in the FRP deck system is available, especially in the area of the impact of shear stud connections on the dynamic response.

In this article, three-dimensional (3D) FE models were established with *ABAQUS 6.11* to analyze the influence of shear studs on a FRP deck bridge. The composite action between the steel girders and the FRP decks were categorized into two types: fully composite and partially composite. By comparison with the results of a field test (Luo and Earls 2003), these FE models were validated. Furthermore, the dynamic response of the FRP deck bridge under moving truck loads was analyzed based on these validated FE models. Based on these models, the influence of the number of shear studs on the dynamic response of the bridge, the range of the ratio of the maximum dynamic deflection to the maximum static deflection, and the difference of dynamic response between the FRP and the RC deck system were studied. In addition, the longitudinal slip and the vertical separation between the FRP deck and the steel girders were studied based on the three partially composite models.

Description of Bridge

In this article, the Boyer Bridge in Pennsylvania was studied. It is a short-span ($L = 12.649$ m), simply supported composite structure using steel stringer-FRP deck systems. It consists of five galvanized stringers (W610 × 155 Gr.345) acting compositely with FRP deck panels (DuraSpan, Martin Marietta Composites). The cellular FRP deck and steel girders are connected by shear studs at 0.61-m intervals along the longitudinal direction of the bridge. As shown in Fig. 1(a), there are two headed shear studs across the steel girder section in each stud pocket, which is subsequently poured with nonshrink grout. The moduli of elasticity of steel, grout, and FRP are 200,000 MPa, 31,841.7 MPa, and 17,241.4 MPa, respectively. The section properties are shown in Table 1, which is based on the information from Martin Marietta Composites.

Existing FE Analysis Used for Composite Beams

A decade ago, most research on shear stud connections was mainly based on extensive push-out tests. Although the test results were helpful for analyzing the strength of shear studs in composite beams, expensive and time-consuming experiments were not good for parametric analysis; very limited data can be obtained from these tests. However, the behavior of shear studs and the composite action of the hybrid beam are complicated; numerous variables are involved and interact mutually, including the deflection of decks and girders, the longitudinal slip and vertical separation between them, the degree of composite action, and so on. Moreover, it is difficult to show the overall effect of the influence of shear studs on the whole composite structure from the small-scale push-out tests, which only concentrate on the local behavior. Thus, FE analysis was introduced to capture the complete behavior of the composite system.

In recent years, FE analysis of steel-concrete composite beams was conducted. Baskar et al. (2002) developed a 3D FE model with *ABAQUS 6.11*, which predicted the ultimate load behavior of steel-concrete composite members accurately. The shear studs were simulated by general beam elements with circular cross sections. The concrete slab was modeled with a 20-node quadratic brick element and reinforcing bars with a rebar option. Three different models were adopted: concrete, cast iron, and elastic-plastic. Lam and El-Lobody (2005) proposed an effective numerical FE model using *ABAQUS 6.11* to simulate the push-off test. Concrete strength and shear stud diameter were considered in parametric studies. This FE model contributed to a better understanding to the failure modes and shear capacity of shear studs. Queiroz et al. (2007) established a FE model of composite beams with full and partial shear connection with *ANSYS 7.0*. Elastic-plastic shell (SHELL 43) and solid (SOLID65) elements were used for the steel section and the concrete slab, respectively. The shear connectors were simulated by nonlinear springs (COMBIN39). Load-deflection behavior, longitudinal slip at the steel-concrete interface, and distribution of stud shear force were studied.

However, to date, extremely limited parametric studies have been carried out through FE analysis on the composite FRP system. Furthermore, these studies were only focused on the behavior under static loads, seldom concerning the dynamic response. Alnahhal et al. (2008) analyzed the fully composite behavior of a FRP bridge deck system using *ABAQUS 6.11*. In the FE model, a perfect bond between the girders and the FRP deck was assumed with no consideration of the slip effect. Only a static monotonic loading was considered in that study.

FE Model of Bridge

A 3D FE model of the Boyer Bridge was established with *ABAQUS 6.11*, as shown in Fig. 1(b). The x-axis was along the width of the bridge, the y-axis along the vertical direction, and the z-axis along the span direction. The facings of the FRP panels were simplified as a solid plate using eight-node linear solid elements with reduced integration (C3D8R), and the contribution of the core of the deck to the load resistance was neglected. The haunch and steel stringers were also modeled by C3D8R. It was designed such that each stringer had 42 shear studs embedded into the top FRP deck. The composite action between the steel girder and the FRP deck was categorized into two types: fully composite and partially composite. In the fully composite model, the deck and the girder were fast tied through the haunch between them. This interaction was simulated by tie in *ABAQUS 6.11*. With the tie constraint, there was no relative motion between the two separate surfaces. The fully composite model was an ideal model in which forces were transmitted to other members most efficiently. In the partially composite model, the interaction between the surfaces of the haunch and the girders were modeled with surface-to-surface contact capable of simulating both the normal behavior and the tangential behavior between the surfaces. The normal behavior was set as hard contact, which meant that

J. Bridge Eng. 2013.18:644-652.

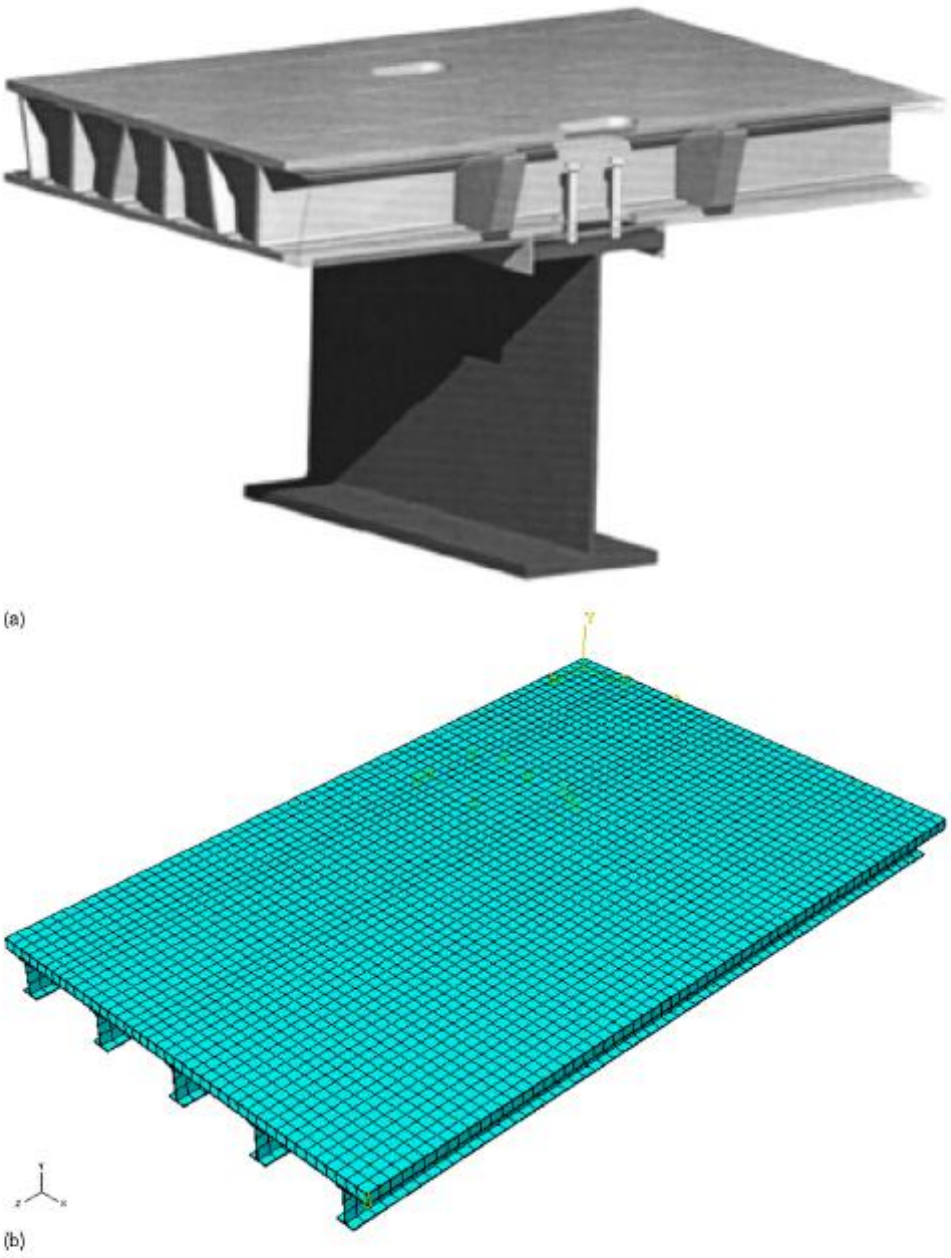

Fig. 1. Depiction of Boyer Bridge: (a) FRP deck system (courtesy of Martin Marietta Composites); (b) FE model of FRP deck bridge

pressure existed between surfaces, and the tangential behavior was set as frictionless, indicating that no friction existed between surfaces. Also, shear studs, which were not only embedded into the FRP deck but also tied to the steel stringers, were simulated by two-node linear truss elements (T3D2). The embedded element technique in *ABAQUS 6.11* is used to specify an element or a group of elements that lie embedded in a group of host elements whose response will be used to constrain the translational degrees of freedom of the embedded nodes. Obviously, it is the shear studs that lead to the composite action between the FRP deck and the steel stringers. Thus, the number of shear studs determines the extent of this composite behavior. In the latter part of the article, this effect was analyzed under moving loads. The partially composite model was further divided into three models with different numbers of shear studs: the designed number of shear studs, double the designed number, and half of the designed number. The FE results of these three partially composite models and the fully composite model were compared to evaluate the contribution of shear stud connections to the composite action.

To capture the typical response of the bridge, points in the steel girders and the FRP deck were selected. As shown in Fig. 2, the five

J. Bridge Eng. 2013.18:644-652.

Table 1. Cross-Section Properties of Steel Stringers and FRP Deck

Property	Dimension (mm)
Steel stringers	
Flange thickness	19.05
Flange width	323.85
Web thickness	12.70
Stringer spacing	1,752.60
FRP deck	
Haunch thickness	12.70
FRP flange thickness	16.76
Deck thickness	194.56

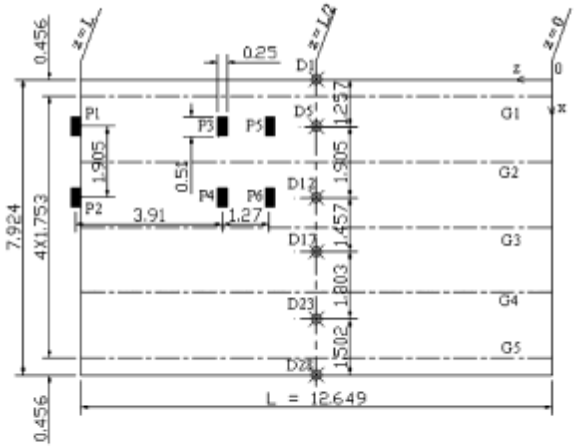

Fig. 2. Load positions in the field test (units = m)

girders were named G1, G2, G3, G4, and G5, with spacing of 1.753 m along the x direction. Also, D1, D5, D12, D17, D23, and D28, all of which were the nodes of the deck at the midspan, were selected to analyze the behavior of the FRP deck. D1 and D28 were on the edge of the deck, whereas D5, D12, D17, and D23 were in the middle of the corresponding neighboring girders. D5 and D12 were in the wheel tracks, where the maximum response of the deck may exist.

Static Performance in the Field Test

The positions of the truck loads in Test 1 of the field test (Luo and Earls 2003) are shown in Fig. 2. The front wheels (P1 and P2) were just off the bridge. The centerline of the truck was located at the centerline of the second girder (G2). Keelor et al. (2004) studied this FRP deck bridge based on the field test, focusing on the effective flange width under static service loading. In this study, several FE models were established to investigate the static and dynamic performance. In the FE model, the loading area at each side of the truck was simplified as rectangular (250 × 510 mm). The weights of the six loads P1, P2, P3, P4, P5, and P6 were approximately 4,273, 3,409, 4,727, 4,273, 4,750, and 4,136 kg, respectively. Three-wire metal foil strain gauges were attached to the steel girders at a longitudinal position located 305 mm from the midspan. As shown in Fig. 3, six strain gauges were attached to each stringer at three height levels: the bottom face of the top flange (Top), the midheight of the stringer (Midheight), and the top face of the bottom flange (Bottom).

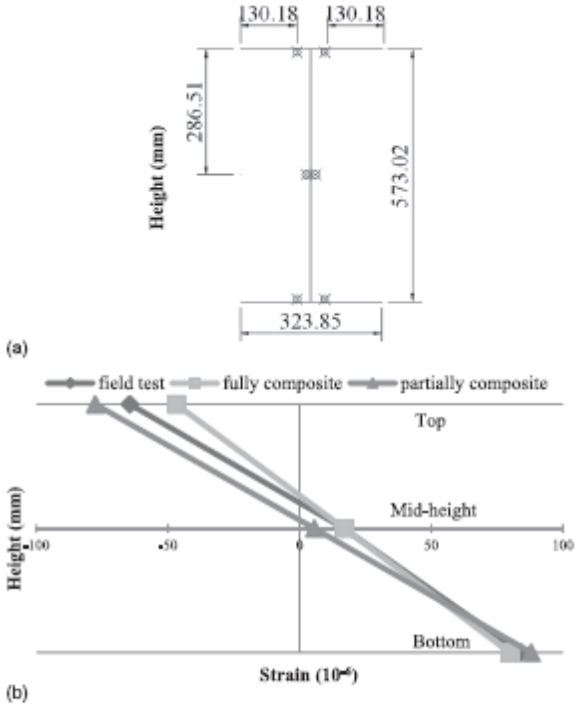

Fig. 3. Longitudinal strain distribution: (a) locations of strain gauges; (b) strain in G2

The longitudinal strain in the two FE models was compared with that in the field test. The FE analysis result and the tested strain were very close, validating the FE models. In the fully composite model, the ratios of the midspan curvature of G1, G3, G4, and G5 to that of G2 are 0.74, 0.64, 0.14, and 0.03, respectively; in the partially composite model, the ratios of the midspan curvature of G1, G3, G4, and G5 to that of G2 are 0.68, 0.65, 0.11, and 0.02, respectively. These ratios revealed that the girders close to the loads took most loads although all girders worked together as a whole through connections to the deck. Also, the strain distribution in Fig. 2 revealed that the position of the neutral axis in the fully composite model was higher than that in the partially composite model, thus indicating that the degree of composite action between the steel girders and the FRP deck in the fully composite model is higher. Furthermore, the strain measured in the field test was between the strain of the fully composite model and the partially composite model. The slope of the longitudinal strains along the height of the girder, indicating the curvature at the midspan, revealed the difference of the degree of composite action between the two FE models and the field test. By comparison with the midspan curvature of G2 in the field test, the curvature in the fully composite model is about 15% lower, and the curvature in the partially composite model is about 10% higher. This comparison suggested that the fully composite model provided a lower bound for the real response of the FRP deck system, and the partially composite model provided an upper bound.

Dynamic Response of FRP Deck Bridge

To date, limited research has been carried out on the dynamic response of FRP deck bridges. Aluri et al. (2005) studied the dynamic

J. Bridge Eng. 2013.18:644-652.

response of three FRP bridge decks supported on steel or FRP stringers through field tests. The investigators claimed that the dynamic load allowance (DLA) factors were mostly within AASHTO 1998 LRFD bridge specification limits. Daly and Cuninghame (2006) examined the performance of a full-scale GFRP bridge deck under static and dynamic wheel loading. They stated that it was important to prevent local damage at web-to-flange connections and the parts close to bearing supports. In the present study, the effect of shear stud connections on the dynamic response of FRP deck bridges under moving vehicle loads was examined based on the FE models validated by the field test; in particular, only the forced vibration without damping was considered.

The maximum dynamic deflection at the midspan of each girder under the moving loads was compared with the corresponding static deflection. Both the fully composite model simulated by tie and the partially composite model simulated with embedded shear studs and surface-to-surface contact were studied. The truck loads passed through the bridge within 0.9 s at 20 m/s, i.e., it was 0.9 s from the start of truck loading onto the bridge to the moment that the rear wheels were just off the bridge. The locations of the loads in the x direction were the same as those in the field test shown in Fig. 2. In *ABAQUS 6.11*, the moving loads were realized by step. The total time was divided into nine steps, and the duration of the each step was 0.1 s. The truck was loaded at a different position at each step, i.e., the six wheels of P1 through P6 were loaded at the different locations of the bridge. When comparing the maximum dynamic response with the maximum static response at the midspan, the latter referred to the response when the truck loads P3 and P4 were located at the midspan, while P1 and P2 were in the left half-span and P5 and P6 were in the right half-span. In this case, the static response at the midspan reached the maximum according to the influence line diagrams. As shown in Fig. 4, for G1, G2, and G3, all of which took most loads, the dynamic or static deflection in the partially composite model was greater than that in the fully composite model, and the static deflection in the partially composite model was even greater than the dynamic deflection in the fully composite model. For G4 and G5, the static or dynamic results in the fully composite model were close to those in the partially composite model. For G1, G2, G3, G4, and G5 under static loads, the ratios of the deflection in the partially composite model to that in the fully composite model were 1.29, 1.37, 1.36, 0.90, and 0.77, respectively; for each girder under moving loads, the ratios of maximum dynamic deflection in the partially composite model to that in the fully composite model were 1.25, 1.30, 1.29, 0.98, and 1.04, respectively. This comparison revealed that the deflection of the main girders (G1, G2, and G3) in the partially composite model was approximately 30% greater than the deflection in the fully composite model. In addition, for G1 through G5 in the fully composite model, the ratios of the maximum dynamic deflection to the corresponding static deflection were 1.18, 1.10, 1.23, 1.73, and 2.48, respectively; whereas, for G1 through G5 in the partially composite model, the ratios were 1.15, 1.05, 1.17, 1.89, and 3.34, respectively. This comparison indicated that the deflection of the main girders may increase between 5 and 20% as a result of the effect of the moving loads.

In the shear-studs design for the RC deck system, the number or the spacing of the shear studs is the most important consideration. Slutter and Fisher (1965) proposed a design procedure with the sufficient number of shear studs to assure the theoretical static ultimate strength of the bridges in which the concrete deck was supported by the lower steel girders. However, no specific guidelines or research on the design of the number of the shear studs in the FRP deck system is available to date. Based on the existing study on the concrete-deck-steel-girder composite system, we only have a vague picture of how many shear studs may affect the degree of the composite action between the FRP deck and the girder. As mentioned previously, from the point of static design of the FRP deck system, the degree of composite action between the FRP deck and the lower girders, which depends on the number of shear studs, is not a main consideration considering the significant decrease of dead load. However, we are not sure how shear stud connections affect the capacity and durability of a FRP deck bridge loaded by moving vehicles.

In this article, to investigate the effect of the number of shear stud connections on the degree of composite behavior under moving loads, the partially composite model was further divided into three models with different numbers of shear studs: the designed number of shear studs, double the designed number, and half of the designed number. It was assumed that the shear studs did not fail, even if the number of shear stud connections was reduced by half. The FE results (the maximum dynamic downward deflection at the midspan) of these three partially composite models and of the fully composite model are shown in Fig. 5. For G1, G2, and G3, the maximum

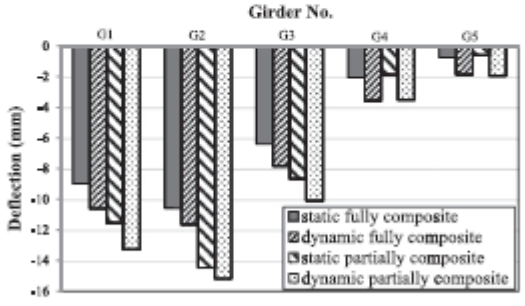

Fig. 4. Maximum static or maximum dynamic deflection at the midspan of the girders

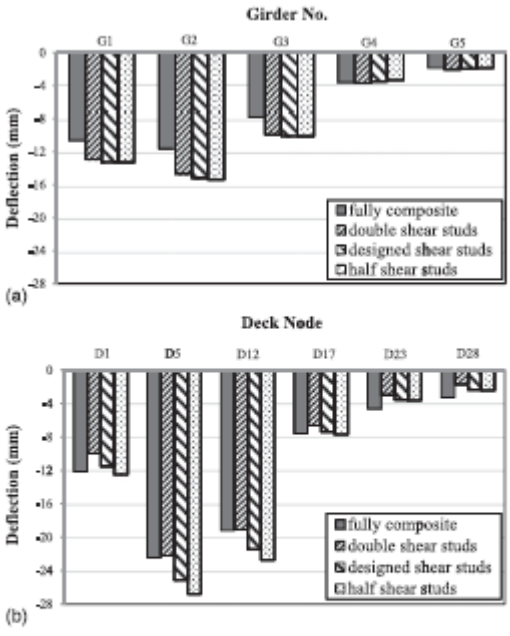

Fig. 5. Maximum dynamic deflection of FRP deck system at midspan: (a) girders; (b) deck

J. Bridge Eng. 2013.18:644-652.

downward deflection increased a small amount with the reduction of the number of shear studs, as shown in Fig. 5(a). The number of shear studs had no significant influence on the dynamic deflection of the steel girders. However, this was not the case for the dynamic deflection of the FRP deck. For deck nodes D5 and D12, both of which were in the wheel tracks of the truck, the maximum dynamic downward deflection increased significantly with the reduction of the number of shear studs, as shown in Fig. 5(b). The maximum downward deflection of the deck occurred at D5. The maximum downward deflection at D5 was approximately 22.20 mm in the model of double shear studs, 25.14 mm in the model of designed shear studs, and 26.79 mm in the model of half shear studs. This change indicated that the maximum downward dynamic deflection in the deck decreased by approximately 12% when the shear stud connections were doubled, and increased by about 7% when half of the connections were used.

The slip and separation at the interface of the FRP deck and the steel girder were also studied. In this article, slip is defined as the longitudinal move of the deck relative to the girder, whereas separation is defined as the difference of the vertical deflection between the deck and the girder. The slip and separation not only indicate the degree of the composite action, but also affect the durability of the structure. As shown in Fig. 6, the slip at the midspan ($z = L/2$) was not evident in all three partially composite models. However, the slip at the two ends ($z = 0$ and $z = L$) was significant, and changed with the decrease of the number of the connections. The slip difference between the maximum slip at $z = 0$ and the maximum slip at $z = L$ was studied. The slip difference in the model of double shear studs was 1.96 mm, the difference in the model of designed shear studs was 2.18 mm, and the difference in the model of half shear studs increased to 2.45 mm. It revealed that the slip at the ends increased with the decrease in the number of shear stud connections. Also, Fig. 6 revealed that the maximum slip occurred during 0.45 s and 0.55 s, when the truck arrived at the vicinity of the midspan. As mentioned previously, the interaction between the steel girders and the FRP deck was simulated by surface-to-surface contact because the adhesive force between them was weak. The separation between them may occur at a specific moment, as shown in Fig. 7. In the model of double shear studs, it seemed that the shear stud connections provided enough bond force to avoid separation. In the model of designed shear studs, the separation was less than 1 mm, which also can be regarded as insignificant because in the real structure there was an adhesive force at the surface between the deck and girders to avoid separation, even if this force was weak. However, in the model of half shear studs, the separation may reach 4.5 mm [see Fig. 7(c)] at some specific moments. It revealed that there was a tendency of separation when the number of shear stud connections decreased to the extent that the connections could not provide enough bond force between the FRP deck and the steel girders.

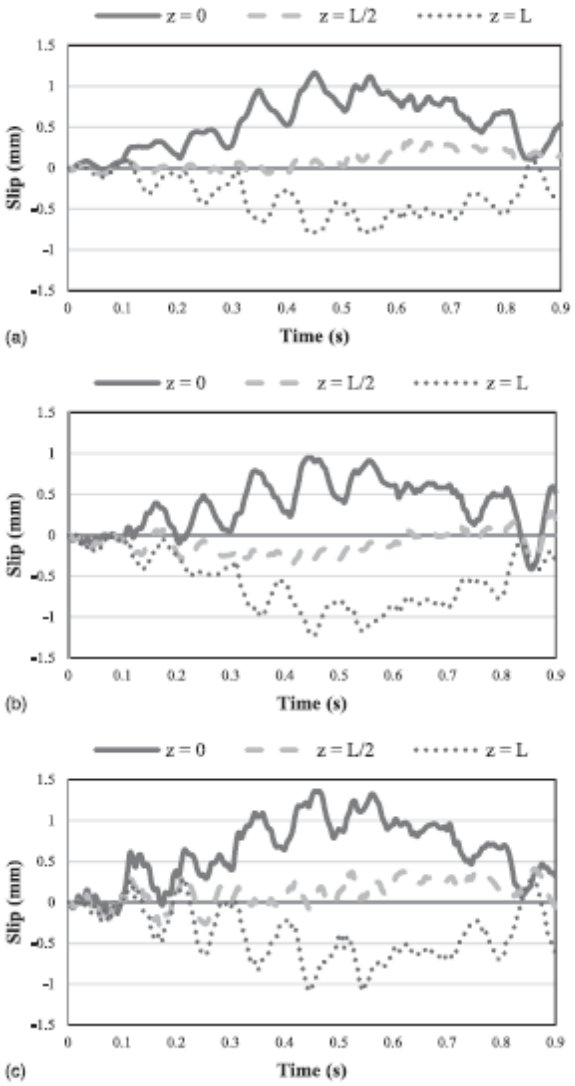

Fig. 6. Slip history of three partially composite models: (a) double shear studs; (b) designed shear studs; (c) half shear studs

Comparison of FRP Deck System and RC Deck System under Moving Loads

Zhang and Cai (2007) claimed that both the load distribution factor values and the dynamic response of FRP deck bridges were greater than those of concrete deck bridges, and that FRP deck bridges with partially composite conditions led to a greater girder load distribution and a larger dynamic displacement by comparison with those of the FRP deck bridges with fully composite conditions. Based on experimentally validated FE models, Chiewanichakorn et al. (2007) studied the dynamic and fatigue response of a truss bridge in which the old deteriorated concrete deck was replaced with a FRP deck. The numerical results suggested that the fatigue life of FRP deck system almost doubled by comparison with the RC deck system. Hag-Elsafi et al. (2011) studied the dynamic characteristics of the Bentley Creek Bridge with a FRP deck. It was shown that the fundamental frequency for the current structure with a FRP deck was approximately 45% higher than that for the original structure with a concrete deck. The maximum dynamic allowance estimated for the FRP deck bridge was lower than that of the concrete deck bridge.

In this article, the dynamic performance of the FRP deck bridges with the corresponding RC deck bridges were compared based on the FE analysis of both the fully composite and the partially composite models. The concrete deck used in the comparison was a 20-cm-deep, cast-in-situ RC deck. The compressive strength of concrete was 41.4 MPa, and the modulus of elasticity was 32,000

J. Bridge Eng. 2013.18:644-652.

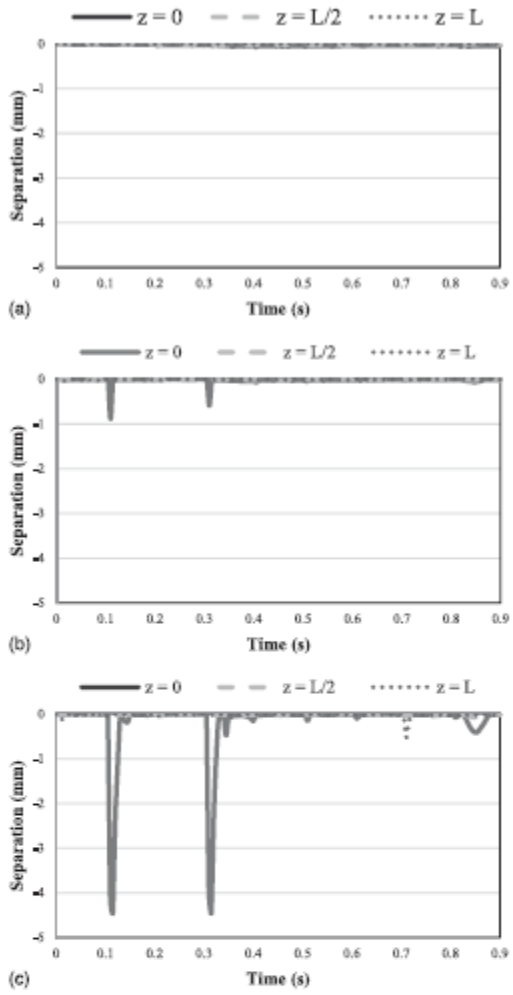

Fig. 7. Separation history of three partially composite models: (a) double shear studs; (b) designed shear studs; (c) half shear studs

MPa. The partially composite models for both FRP and RC deck systems used designed numbers of shear studs.

As shown in Fig. 5, the maximum response of the girders and the decks occurred in G2 and D5, respectively; thus, their response was the concern. As shown in Fig. 8, the dynamic response in the FRP deck system was greater than that in the RC deck system, and the vibration amplitude in the former was greater than that in the latter. For the girders in the FRP deck system, the vibration amplitude in the fully composite model was approximately 80% of that in the partially composite model. As shown in Figs. 8 and 9, in the partially composite model of the FRP deck system, the maximum dynamic deflection of G2 occurred at 0.45 s and another deflection peak existed at 0.55 s, whereas the maximum dynamic deflection of D5 occurred at 0.55 s and another deflection peak existed at 0.45 s. In Fig. 6, the slip peaks (the slip history of $z = 0$ and $z = L$) also existed at 0.45 s and 0.55 s. The truck was located at the vicinity of the midspan between 0.45 and 0.55 s, indicating that when the moving loads arrived at the midspan, the slip at the two ends and the girder deflection at the midspan may reach the maximum, simultaneously.

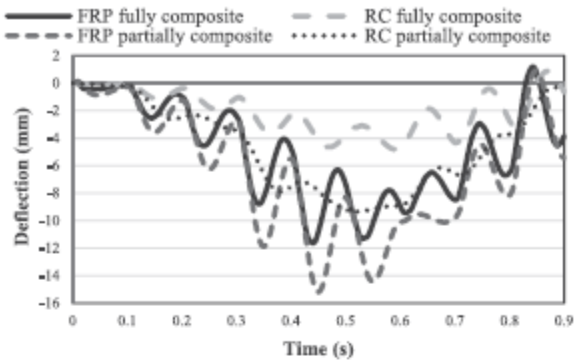

Fig. 8. Dynamic deflection history of G2 in FRP/RC deck systems

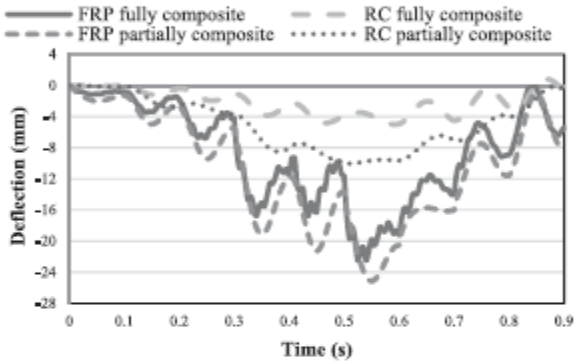

Fig. 9. Dynamic deflection history of D5 in FRP/RC deck systems

In addition, the lag phenomenon was obvious. As shown in Fig. 8, the dynamic response in the partially composite model of the FRP deck system lagged behind that in the fully composite model. This lag phenomenon was attributed to the different degree of composite action between the FRP deck and the steel girder. In the fully composite model with the higher degree of composite action, the FRP deck and the steel girders were tied fast to work as a whole member; in the partially composite model, the load was taken by the FRP deck directly, then was transmitted to the girders through the interaction between the FRP deck and the steel girders.

The maximum downward dynamic deflections in the FRP and RC deck systems are shown in Fig. 10. The maximum downward deflections of G1 and G2 in the FRP deck system were considerably greater than those of the other three girders, whereas the difference of the maximum downward deflections for all girders in the RC deck system was not as significant, as shown in Fig. 10(a). In addition, the maximum downward deflections of D5 and D12 in the FRP deck system were much greater than those of the other deck nodes, whereas the differences in the RC deck system were not as significant, as shown in Fig. 10(b). In the RC deck system, the connections between the deck and the girders were stronger than those in the FRP deck system; thus, the RC deck may transmit more loads to the girders farther from the load positions. Furthermore, Fig. 10 reveals that the difference of maximum downward deflection between the deck and the girder in the FRP deck system was significantly greater than that in the RC deck system. The lower stiffness of the

J. Bridge Eng. 2013.18:644-652.

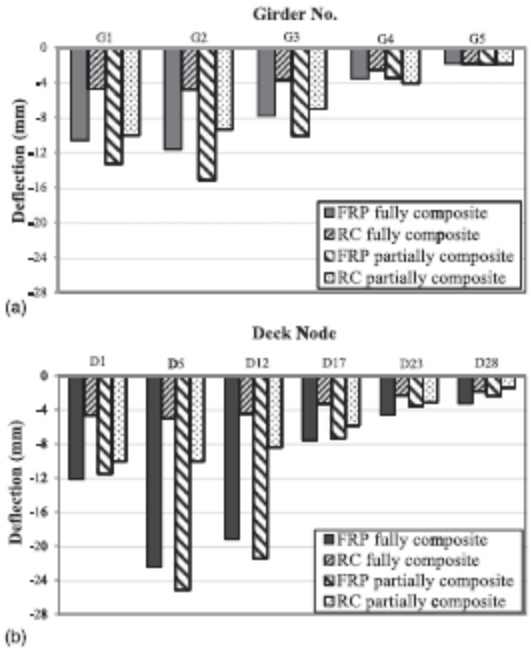

Fig. 10. Maximum dynamic deflection in FRP/RC deck systems: (a) girders; (b) deck

FRP deck compared with the RC deck resulted in significant deflection in the FRP deck. Finally, for the FRP deck system, FE analysis revealed that the maximum downward deflection of the girder existed in G2, the maximum downward deflection of the deck existed in the wheel tracks (D5 and D12), and the maximum upward deflection existed in the exterior girder (G1) and in the deck edge (D1).

Conclusions

The structural behavior of a FRP deck bridge, Boyer Bridge, was studied based on FE analysis. Two different FE models were analyzed: fully composite and partially composite. The static performance of the bridge FE models was compared with the field test results to verify the applicability of these two FE models. Furthermore, these FE models were used to analyze the effect of the shear stud connections on the dynamic response of the bridge under moving loads, focusing on the midspan deflection of the girders and the FRP deck, and the slip and separation at their interface. Also, the dynamic response of the FRP deck bridge was compared with that of the RC deck system. Based on the results of this study, the following conclusions can be drawn:

1. This study used tie to simulate the fully composite action and surface-to-surface contact and embedded shear studs to simulate the partially composite action in the FE analysis. The strain distribution along the height of the girders revealed that the position of the neutral axis in the fully composite model was higher than that in the partially composite model, and the curvature at the midspan in the fully composite model was smaller. The degree of composite behavior in the real structure was between the fully composite action and the partially composite action. The FE results of the fully composite model and the partially composite model provide a lower bound and an upper bound for the real response of the FRP deck system.
2. The static or dynamic response in the fully composite model of the FRP deck bridge is smaller than that in the partially composite model. For Boyer Bridge, the deflections of main girders in the partially composite model were approximately 30% greater than those in the fully composite model. Also, the dynamic deflection of the main girders may increase between 5 and 20% by comparison with the static response, a a result of the dynamic effect of the moving loads.
3. The number of shear stud connections significantly affects the composite action under moving loads. In this research, although its influence on the dynamic deflection of the girder was not significant, the maximum downward deflection in the deck decreased by approximately 12% when the shear stud connections were doubled and increased by about 7% when half of the connections were used. In addition, the reduction of the number of the shear studs may increase the slip at the interface, and even lead to significant separation. Furthermore, the slip at the two ends and the girder deflection at the midspan may reach the maximum simultaneously.
4. The dynamic deflection history showed that the dynamic response in the partially composite model lagged behind that in the fully composite model.
5. In comparison with the RC deck bridge, both the dynamic response and the vibration amplitude are greater in the FRP deck bridge. The RC deck may transmit more loads to the girders farther from the load positions, because of the stronger connections between the deck and the girders. In addition, the difference of maximum downward deflection between the deck and the girder in the FRP deck system was significantly greater than that in the RC deck system, because of the lower stiffness of the FRP deck compared with the RC deck.

This research focused on the effect of the number of shear studs and compared FRP and RC deck systems. For the purpose of better understanding the effect of shear studs on the behavior of FRP deck bridges, other factors, including the size and shape of the shear studs, the type of FRP deck, and the effect of time and temperature should be considered in future research; and experimental tests should be conducted to fully investigate the dynamic response under moving loads. Finally, the extremely limited experimental data for FRP deck bridges makes the FE analysis necessary and valuable.

Acknowledgments

The financial support to the second author provided by the National Science Foundation—NSF CAREER program (CMS-0550899) is gratefully acknowledged. The authors would also like to thank the Center for Transportation Research (CTR) at the Univ. of Tennessee Knoxville for providing the financial support to the first author.

References

AASHTO. (1998). *LRFD bridge design specifications*, Washington, DC.

ABAQUS 6.11 [Computer software]. Providence, RI, Dassault Systèmes Simulia Corp.

Alnahhal, W., Aref, A., and Alampalli, S. (2008). "Composite behavior of hybrid FRP-concrete bridge decks on steel girders." *Compos. Struct.*, 84(1), 29–43.

Aluri, S., Jinka, C., and GangaRao, H. V. S. (2005). "Dynamic response of three fiber reinforced polymer composite bridges." *J. Bridge Eng.*, 10(6), 722–730.

ANSYS 7.0 [Computer software]. Canonsburg, PA, ANSYS.

Baskar, K., Shanmugam, N. E., and Thevendran, V. (2002). "Finite-element analysis of steel-concrete composite plate girder." *J. Struct. Eng.*, 128(9), 1158–1168.

Chiewanichakorn, M., Aref, A. J., and Alampalli, S. (2007). "Dynamic and fatigue response of a truss bridge with fiber reinforced polymer deck." *Int. J. Fatigue*, 29(8), 1475–1489.

Daly, A. F., and Cuninghame, J. R. (2006). "Performance of a fibre-reinforced polymer bridge deck under dynamic wheel loading." *Compos. Part A Appl. Sci. Manuf.*, 37(8), 1180–1188.

Davalos, J. F., Chen, A., and Zou, B. (2011). "Stiffness and strength evaluations of a shear connection system for FRP bridge decks to steel girders." *J. Compos. Constr.*, 15(3), 441–450.

Gattesco, N. (1999). "Analytical modeling of nonlinear behavior of composite beams with deformable connection." *J. Constr. Steel Res.*, 52(2), 195–218.

Hag-Elsafi, O., Albers, W. F., and Alampalli, S. (2011). "Dynamic analysis of the Bentley Creek Bridge with FRP deck." *J. Bridge Eng.*, 17(2), 318–333.

Ji, H. S., Song, W., and Ma, Z. (2010). "Design, test and field application of a GFRP corrugated-core sandwich bridge." *Eng. Struct.*, 32(9), 2814–2824.

Keelor, D. C., Luo, Y., Earls, C. L., and Yulismana, W. (2004). "Service load effective compression flange width in fiber reinforced polymer deck systems acting compositely with steel stringers." *J. Compos. Constr.*, 8(4), 289–297.

Lam, D., and El-Lobody, E. (2005). "Behavior of headed stud shear connectors in composite beam." *J. Struct. Eng.*, 131(1), 96–107.

Li, L., Ma, Z., Griffey, M. E., and Oesterle, R. G. (2010). "improved longitudinal joint details in decked bulb tees for accelerated bridge construction: Concept development." *J. Bridge Eng.*, 15(3), 327–336.

Luo, Y., and Earls, C. L. (2003). "The composite response assessment of the steel stringer-FRP deck system in the Boyer Bridge." *Rep. No. FHWA-PA-2002-043-97-04*, Dept. of Civil and Environmental Engineering, Univ. of Pittsburgh, Pittsburgh.

Moon, F. L., Eckel, D. A., and Gillespie, J. W. (2002). "Shear stud connections for the development of composite action between steel girders and fiber-reinforced polymer bridge decks." *J. Struct. Eng.*, 128(6), 762–770.

Ollgaard, J.G., Slutter, R.G., and Fisher, J.W. (1971). "Shear strength of stud connectors in lightweight and normal weight concrete." *AISC Eng. J.*, 55–64.

Pallares, L., and Hajjar, J. F. (2009a). "Headed steel stud anchors in composite structures: Part I—Shear." *Rep. No. NSEL-013*, Univ. of Illinois at Urbana-Champaign, Urbana-Champaign, IL.

Pallares, L., and Hajjar, J. F. (2009b). "Headed steel stud anchors in composite structures: Part II—Tension and interaction." *Rep. No. NSEL-014*, Univ. of Illinois at Urbana-Champaign, Urbana-Champaign, IL.

Park, K. T., Kim, S. H., Lee, Y. H., and Hwang, Y. K. (2006). "Degree of composite action verification of bolted GFRP bridge deck-to-girder connection system." *Compos. Struct.*, 72(3), 393–400.

Queiroz, F. D., Vellasco, P. C. G. S., and Nethercot, D. A. (2007). "Finite element modeling of composite beams with full and partial shear connection." *J. Constr. Steel Res.*, 63(4), 505–521.

Schollmayer, M., and Keller, T. (2009). "Modeling of through-thickness stress state in adhesive joints connecting pultruded FRP bridge decks and steel girders." *Compos. Struct.*, 90(1), 67–75.

Slutter, R.G., and Fisher, J. W. (1965). "Tentative design procedure for shear connectors in composite beams." *Fritz Engineering Laboratory Report No. 316.1A*, Lehigh Univ., Bethlehem, PA.

Xue, W., Ding, M., Wang, H., and Luo, Z. (2008). "Static behavior and theoretical model of stud shear connectors." *J. Bridge Eng.*, 13(6), 623–634.

Zhang, Y., and Cai, C. S. (2007). "Load distribution and dynamic response of multi-girder bridges with FRP decks." *Eng. Struct.*, 29(8), 1676–1689.

J. Bridge Eng. 2013.18:644-652.

Vita

Xin Jiang was born in Hunan, China in October, 1981. He received a B.S degree and a M.S in Civil Engineering in China.

Xin is currently pursuing his doctorate degree in Civil Engineering at the University of Tennessee, Knoxville.